

UNIVERSITY OF CALIFORNIA
SANTA CRUZ

**SEARCH FOR WW AND WZ RESONANCES IN $\ell\nu qq$ FINAL
STATES IN pp COLLISIONS AT $\sqrt{s} = 13$ TEV WITH THE ATLAS
DETECTOR**

A dissertation submitted in partial satisfaction of the
requirements for the degree of

DOCTOR OF PHILOSOPHY

in

PHYSICS

by

Natasha Woods

December 2019

The Dissertation of Natasha Woods
is approved:

Abraham Seiden, Chair

Mike Hance

Bruce Schumm

Quentin Williams
Vice Provost and Dean of Graduate Studies

Copyright © by

Natasha Woods

2019

Table of Contents

List of Figures	vi
List of Tables	xvi
Abstract	xix
Dedication	xx
Acknowledgments	xxi
I Introduction	1
1 Introduction	2
II Theoretical Motivation	6
2 The Standard Model of Particle Physics	7
2.1 Introduction	7
2.2 Quantum Field Theory	7
2.3 $U(1)_{EM}$ Local Gauge Invariance	8
2.4 Yang-Mills Gauge Theories	11
2.5 Particles in the Standard Model	12
2.6 Higgs Mechanism	17
2.7 Electroweak Theory	18
2.8 Quantum Chromodynamics	18
3 Standard Model Successes and Limitations	24
4 New Physics Models with Diboson Resonances	27
4.1 Randall Sundrum Bulk Model	27
4.2 Simple Standard Model Extensions	29

III Experimental Setup	32
5 LHC	33
5.1 LHC Layout and Design	35
6 The ATLAS Detector	39
6.1 Coordinate System	42
6.2 Inner Detector	42
6.2.1 Pixel Detector	44
6.2.2 Semiconductor Tracker	45
6.2.3 Transition Radiation Tracker	45
6.3 Calorimeters	46
6.4 Muon Spectrometer	51
6.5 Magnet System	55
6.6 Trigger System	56
IV The Search for WW and WZ Resonances in $\ell\nu qq$ final states	58
7 Dataset and Simulated Samples	59
7.1 Dataset	59
7.2 Simulated Samples	62
8 Objects	63
8.1 Electrons	63
8.2 Muons	64
8.3 Jets	65
8.3.1 Small-R jets	68
8.3.2 Large-R jets	69
8.3.3 Variable Radius jets	73
8.3.4 Jet Flavor Tagging	73
8.4 MET/Neutrinos	74
8.5 Overlap Removal	74
8.6 Reconstructed Resonance Mass (m_{WW})	75
9 Event Selection and Categorization	76
9.1 Pre-selection	77
9.2 Trigger	78
9.3 non-VBF/VBF RNN	80
9.4 Signal Region Definitions	87
9.5 Selection Acceptance and Efficiency	90

10 Background Estimate	92
10.1 Control Regions	93
10.2 Fake Lepton Backgrounds	100
11 Systematic Uncertainties	114
11.1 Experimental Systematics	114
11.2 Theoretical Systematics	116
12 Statistical Analysis	124
12.1 Likelihood Function	125
12.2 Fit Configuration	125
12.3 Best Fit μ	128
12.4 Discovery Test	128
12.5 Exclusion Limits	130
13 Results	132
13.1 Expected and Measured Yields	132
13.2 Systematic Profiling and Correlations	142
13.3 Discovery Tests	144
13.4 Limits	145
V Quark and Gluon Tagging	148
14 Quark Gluon Tagging in $\ell\nu qq$ Diboson Resonance Search	149
15 Quark Gluon Tagger Calibration	156
16 Quark Gluon Tagger Impact in Diboson Resonance Search	165
VI Conclusion	167
17 Conclusions	168
Bibliography	169

List of Figures

2.1	The particles of the Standard Model.	14
2.2	Summary of SM particle interactions.	15
2.3	This figure shows the three dominant QCD interactions [41] . . .	20
2.4	Strength of the $U(1)$, $SU(2)$, and $SU(3)$ gauge couplings as a function of the energy scale of the interaction (Q). From Ref. [27] . .	21
2.5	A cartoon of string breaking: the QCD string spanned between quark Q and antiquark \bar{Q} breaks due to $q\bar{q}$ creation [13].	23
3.1	A comparison of cross section measurements at $\sqrt{s} = 7, 8, 13$ TeV from ATLAS compared to theoretical measurements. From Ref. [15]	26
4.1	Cartoon of RS Bulk Model	29
5.1	Scaling of various SM cross sections with \sqrt{s}	34
5.2	The layout of the LHC and the four detectors along the beam line (ATLAS, LHCb, ALICE, CMS).	36
5.3	An overview schematic of the LHC accelerator subsystems.	37
6.1	Overview schematic of the ATLAS detector.	40
6.2	A cartoon of how different particles interact and are detected within ATLAS.	41
6.3	Layout of ATLAS Inner Detector	43
6.4	Layout of ATLAS ID Barrel System.	44
6.5	Overview of ATLAS electromagnetic and hadronic calorimeters. .	48

6.6	Schematic of ECAL	49
6.7	Schematic of HCAL	50
6.8	Schematic of Muon Spectrometer [16]	53
6.9	Schematic of MDT chamber.	54
6.10	Schematic of RPC chamber, which is used for triggering in the central region of the detector.	54
6.11	Schematic of TGC chamber, which is used for triggering in the muon end-cap region.	55
6.12	Layout of ATLAS magnet systems.	56
7.1	Integrated luminosity for data collected from ATLAS from 2011 - 2018	60
7.2	Mean number of interactions per crossing for data collected from ATLAS from 2011 - 2018	61
8.1	This figure shows the breakdown of the muon reconstruction efficiency scale factor measured in $Z \rightarrow \mu\mu$ as a function of the muon p_T [14].	65
8.2	This diagram shows the calibration stages for EM jets [21]	68
8.3	The upper cut on D_2 (a) and jet mass window cut i.e. the upper and lower boundary of the mass (b) of the W -tagger as a function of jet p_T . Corresponding values for Z -tagger are shown in (c) and (d). The optimal cut values for maximum significance are shown as solid markers and the fitted function as solid lines. Working points from $VV \rightarrow JJ$ [20] is also shown as dashed lines as a reference.	71
8.4	The left (right) plot shows the efficiency for the $W(Z)$ tagger mass and D_2 cuts as a function of large-R jet p_T	72

9.1	This figure shows the architecture of the RNN used to classify events as non-VBF/VBF. The two VBF candidate jet's variable are passed to a through two layers of LSTMs. The vector output of the final LSTM is combined to give the scalar output of the RNN used to classify the event as non-VBF/VBF.	82
9.2	This figure shows the embedded logic in LSTM cells. This image was taken from [48], where a more in depth discussion about LSTMs may be found.	83
9.3	RNN Score distribution for ggF and VBF signals and backgrounds.	84
9.4	ROC curve using k-fold validation for RNN.	85
9.5	Comparison of ggF Z' limits for different RNN score selections. The bottom panel shows the ratio of the upper limits set for different RNN cuts to the cut-based analysis. In this panel smaller numbers, indicate that the expected upper limit is smaller than the cut-based analysis, which is desired.	86
9.6	This diagram shows the prioritization scheme used to classify events into the various SRs and CRs. The VBF regions are prioritized over the non-VBF regions and the merged analysis is prioritized over the resolved analysis.	89
9.7	Selection acceptance times efficiency for the $W' \rightarrow WZ \rightarrow \ell\nu qq$ events from MC simulations as a function of the W' mass for Drell-Yan (left) and VBF production (right), combining the merged HP and LP signal regions of the $WV \rightarrow \ell\nu J$ selection and the resolved regions of the $WV \rightarrow \ell\nu jj$ selection. Note: the VBF selection acceptance for the DY W' is approximately zero in the left plot. .	90
9.8	Selection acceptance times efficiency for the $G \rightarrow WW \rightarrow \ell\nu qq$ events from MC simulations as a function of the G mass for (a) Drell-Yan and (b) VBF production, combining the merged HP and LP signal regions of the $WV \rightarrow \ell\nu J$ selection and the resolved regions of the $WV \rightarrow \ell\nu jj$ selection. Note: the VBF selection acceptance for the ggF G'_{KK} is approximately zero in the left plot.	91

10.1 Data MC comparison for the merged WW HP TCR. The bottom panel shows the ratio of the difference between data and simulation to simulation. The red bands include the all systematic and statistical uncertainties on the background.	94
10.2 Data MC comparison for the merged WW LP TCR. The bottom panel shows the ratio of the difference between data and simulation to simulation. The red bands include the all systematic and statistical uncertainties on the background.	95
10.3 Data MC comparison for the merged WZ HP TCR. The bottom panel shows the ratio of the difference between data and simulation to simulation. The red bands include the all systematic and statistical uncertainties on the background.	96
10.4 Data MC comparison for the merged WZ LP TCR. The bottom panel shows the ratio of the difference between data and simulation to simulation. The red bands include the all systematic and statistical uncertainties on the background.	97
10.5 Data MC comparison for the resolved WW TCR. The bottom panel shows the ratio of the difference between data and simulation to simulation. The red bands include the all systematic and statistical uncertainties on the background.	98
10.6 Data MC comparison for the resolved WZ TCR. The bottom panel shows the ratio of the difference between data and simulation to simulation. The red bands include the all systematic and statistical uncertainties on the background.	99
10.7 The E_T^{miss} distribution in MJCR for 2017 data in the electron channel(left), muon channel with W-boson pT < 150 GeV (center) and > 150 GeV (right). Multi-jet templates are given by the difference between the data and simulated distributions.	102
10.8 Postfit Data/MC comparison of distributions of E_T^{miss} , m_T^W , lepton and neutrino p_T , $m_{\ell\nu jj}$, lepton- ν angular distance in the WW electron channel. The MJ template is obtained from the pre-MJ-fit. 103	103

10.9 Postfit Data/MC comparison of distributions of E_T^{miss} , m_T^W , lepton and neutrino p_T , $m_{\ell\nu jj}$, lepton- ν angular distance in the WW muon channel. The MJ template is obtained from the pre-MJ-fit.	104
10.10 Postfit Data/MC comparison of distributions of E_T^{miss} , m_T^W , lepton and neutrino p_T , $m_{\ell\nu jj}$, lepton- ν angular distance in the WZ untag electron channel. The MJ template is obtained from the pre-MJ-fit.	105
10.11 Postfit Data/MC comparison of distributions of E_T^{miss} , m_T^W , lepton and neutrino p_T , $m_{\ell\nu jj}$, lepton- ν angular distance in the WZ untag muon channel. The MJ template is obtained from the pre-MJ-fit.	106
10.12 Postfit Data/MC comparison of distributions of E_T^{miss} , m_T^W , lepton and neutrino p_T , $m_{\ell\nu jj}$, lepton- ν angular distance in the WZ untag electron channel. The MJ template is obtained from the pre-MJ-fit.	107
10.13 Postfit Data/MC comparison of distributions of E_T^{miss} , m_T^W , lepton and neutrino p_T , $m_{\ell\nu jj}$, lepton- ν angular distance in the WZ untag muon channel. The MJ template is obtained from the pre-MJ-fit.	108
10.14 Postfit Data/MC comparison of distributions of E_T^{miss} , m_T^W , lepton and neutrino p_T , $m_{\ell\nu jj}$, lepton- ν angular distance in the VBF WW electron channel. The MJ template is obtained from the pre-MJ-fit.	109
10.15 Postfit Data/MC comparison of distributions of E_T^{miss} , m_T^W , lepton and neutrino p_T , $m_{\ell\nu jj}$, lepton- ν angular distance in the VBF WW muon channel. The MJ template is obtained from the pre-MJ-fit.	110
10.16 Postfit Data/MC comparison of distributions of E_T^{miss} , m_T^W , lepton and neutrino p_T , $m_{\ell\nu jj}$, lepton- ν angular distance in the VBF WZ electron channel. The MJ template is obtained from the pre-MJ-fit.	111
10.17 Postfit Data/MC comparison of distributions of E_T^{miss} , m_T^W , lepton and neutrino p_T , $m_{\ell\nu jj}$, lepton- ν angular distance in the VBF WZ muon channel. The MJ template is obtained from the pre-MJ-fit.	112

11.1 The W/Z+jet systematics for the a) Merged ggF, b) Resolved ggF, c) Merged VBF, and d) Resolved VBF regions. The top subplot shows the nominal and variation distributions/bands, the middle shows the ratio of the two, and the final shows just the shape of the envelope (the final uncertainty).	118
11.2 The two-point generator comparison between Sherpa and MadGraph for the W/Z+jet samples in the a) Merged ggF, b) Resolved ggF, c) Merged VBF, and d) Resolved VBF regions. The normalization of the Madgraph sample is set to the Sherpa value to consider only shape effects. The bottom inlet shows the ratio of the two.	119
11.3 Ratio between the variations of generator (red) and hadronization (blue) variations for the Merged regime for $t\bar{t}$ sample.	120
11.4 Ratio between the variations of generator (red) and hadronization (blue) variations for the Resolved regime for $t\bar{t}$ sample.	120
11.5 Ratio between the variations of ISR up (red) and down (blue) variations for the Merged regime for $t\bar{t}$ sample.	121
11.6 Ratio between the variations of ISR up (red) and down (blue) variations for the Resolved regime for $t\bar{t}$ sample.	122
11.7 Ratio between the variations of FSR up (red) and down (blue) variations for the Merged regime for $t\bar{t}$ sample.	123
11.8 Ratio between the variations of FSR up (red) and down (blue) variations for the Resolved regime for $t\bar{t}$ sample.	123
12.1 The HVT signal mass resolution as a function of mass fit with a straight line in the Resolved ggF region (left) and VBF (right) region.	126
12.2 The HVT signal mass resolution as a function of mass fit with a straight line in the Merged ggF region (left) and VBF (right) region.	126
13.1 The distribution of $m_{\ell\nu qq}$ in the DY $WW(WZ)$ control regions on the left(right).	139

13.2	The distribution of $m_{\ell\nu qq}$ in the VBF $WW(WZ)$ control regions.	140
13.3	The distribution of $m_{\ell\nu qq}$ in the GGF WW signal regions.	141
13.4	The distribution of $m_{\ell\nu qq}$ in the GGF WZ Untag signal regions.	141
13.5	The distribution of $m_{\ell\nu qq}$ in the GGF WZ Tag signal regions.	141
13.6	The distribution of $m_{\ell\nu qq}$ in the VBF WW Tag signal regions.	142
13.7	The distribution of $m_{\ell\nu qq}$ in the VBF WZ Tag signal regions.	142
13.8	Ranked systematics and their fitted values for WW DY (right) and VBF (left) selections.	143
13.9	Ranked systematics and their fitted values for WZ DY (right) and VBF (left) selections.	143
13.10	Correlations between systematics for WW DY (right) and VBF (left) selections.	144
13.11	These plots show the measured p_0 value as a function of resonance mass for HVT Z' DY(VBF) production, left(right).	144
13.12	These plots show the measured p_0 value as a function of resonance mass for HVT W' DY(VBF) production, left(right).	145
13.13	These plots show the measured p_0 value as a function of resonance mass for the RS Graviton DY production.	145
13.14	Theory, expected and observed limits for HVT W' DY (left) and VBF (right) production.	146
13.15	Theory, expected and observed limits for HVT Z' DY (left) and VBF (right) production.	146
13.16	Theory, expected and observed limits for RS Gravitons via gluon- gluon fusion production.	147

14.1 PDGID of the truth-level parton matched to the small-R jets passing the Resolved GGF WW Signal Region selections for the (a) Leading (b) Sub-Leading jets . These distributions are shown for 300, 500, and 700GeV Z' signals and the background (all simulated backgrounds that pass SR selections). PDGID = -1 corresponds to pileup jets, $0 < \text{PDGID} < 6$ correspond to quarks and PDGID = 21 corresponds to gluons.	151
14.2 The number of tracks in small-R jets in events passing the Resolved GGF WW Signal Region selections for the (a) Leading (b) Sub-Leading jets. These distributions are shown for 300, 500, and 700GeV Z' signals and the background.	151
14.3 The number of tracks in background small-R jets in events passing the Resolved GGF WW Signal region selection vs. $\ln(p_T)$ for (a)Leading (b) Sub-Leading jets. The best fit line for the distribution is also shown, as well as the percentage of jets that pass a cut of number of tracks $< 4 \times \ln(p_T) - 5$. Note the number of total entries in these plots has been normalized to one.	152
14.4 The number of tracks in small-R jets in 300GeV Z' events passing the Resolved GGF WW Signal region selection vs. $\ln(p_T)$ for (a)Leading (b) Sub-Leading jets. The best fit line for the distribution is also shown, as well as the percentage of jets that pass a cut of number of tracks $< 4 \times \ln(p_T) - 5$.Note the number of total entries in these plots has been normalized to one.	152
14.5 The number of tracks in small-R jets in 500GeV Z' events passing the Resolved GGF WW Signal region selection vs. $\ln(p_T)$ for (a)Leading (b) Sub-Leading jets. The best fit line for the distribution is also shown, as well as the percentage of jets that pass a cut of number of tracks $< 4 \times \ln(p_T) - 5$.Note the number of total entries in these plots has been normalized to one.	153

14.6 The number of tracks in small-R jets in 700GeV Z' events passing the Resolved GGF WW Signal region selection vs. $\ln(p_T)$ for (a)Leading (b) Sub-Leading jets. The best fit line for the distribution is also shown, as well as the percentage of jets that pass a cut of number of tracks $< 4 \times \ln(p_T) - 5$. Note the number of total entries in these plots has been normalized to one.	153
14.7 ROC Curve for Quark and Gluon Tagging with a cut on the number of tracks that depends on the $\ln(p_T)$	154
14.8 The top panel shows the distribution of m_{lvqq} with and without quark gluon tagging. The middle panel shows the ratio of the signals and backgrounds with and without quark gluon tagging. The bottom panel shows the change in S/\sqrt{B} with quark gluon tagging.	155
15.1 Unfolded and extracted n_c quark and gluon distributions.	161
15.2 The distribution of n_{trk} and m_{WV} for the resolved WCR and TCR including systematics from the quark gluon tagger calibration.	162
15.3 These figures show the impact of the uncertainties on the number of tracks in the leading jet in the sum of the background sample in the Resolved ggF WW SR (a) tracking efficiency (b) fake (c) PDF (d) ME (e) unfolding uncertainties.	163

15.4 An illustration of the closure test from the central-forward method. Filled squares and circles in the upper panel are the value of $\langle n_{charged}^{c,f} \rangle$. The open blue points show $\langle n_{charged}^{q,g} \rangle$ extracted. Open red and black points show $\langle n_{charged}^{q,g} \rangle$ for the more forward and more central jets extracted from labels directly in simulation. The middle panel shows the ratio of $\langle n_{charged}^{q,g} \rangle$ for the forward versus central jets and the lower panel shows the ratio for the values extracted and the ones taken directly from simulation for the more forward jets. The extraction method used is possible because the filled red squares and circles are slightly displaced from each other. Closure is given by the fact that the open stars, circles, and up triangles overlap and the open crosses, squares, and down triangles also overlap [22].	164
16.1 The top panel shows the distribution of m_{lvqq} with and without requiring jets to be true quarks. The middle panel shows the ratio of the signals and backgrounds with and without requiring jets to be true quarks. The bottom panel shows the change in S/\sqrt{B} when requiring jets to be true quarks.	166
16.2 ROC curves for quark gluon tagging BDT (trained using jet substructure variables) and convolutional neural networks (trained using jet images) on (left) 200 GeV and (right) 1000 GeV Pythia jets using jet substructure variables [33].	166

List of Tables

2.1	Representations of the SM fermions under $SU(3)_C \times SU(2)_L \times U(1)_Y$ gauge symmetry group. Rows are correspond to different weak isospin states and columns to different QCD color states.	13
9.1	The list of triggers used in the analysis.	79
9.2	Summary of selection criteria used to define the signal region (SR), W +jets control region (W CR) and $t\bar{t}$ control region ($t\bar{t}$ CR) for merged 1-lepton channel.	88
9.3	The list of selection cuts in the resolved analysis for the WW and WZ signal regions (SR), W +jets control region (WR) and $t\bar{t}$ control region (TR).	89
10.1	Definitions of “inverted” leptons used in multijet control region. For the inverted muon selection, $ptvarcone30$ is given by sum of the p_T of tracks in a cone around the muon candidate divided by the muon p_T . The size of the cone, δR used is $10\text{GeV}/p_T^\mu$ or 0.3, whichever is smaller. So, as the p_T of the muon increases, the cone size used decreases. This is useful as more boosted muons are more likely to be produced in dense environments and using a smaller cone size more accurately determines the quality of the muon.	101

10.2 Fit validation result in WCRs for 2015+16 data. The fit is done in various WCRs, in order to obtain the corresponding scale factors for MJ templates: non-VBF resolved WCR for the $WW \rightarrow lvqq$ selection, non-VBF resolved untagged WCR for the $WZ \rightarrow lvqq$ selection, non-VBF resolved tagged WCR for the $WZ \rightarrow lvqq$ selection, VBF resolved WCR for the $WW \rightarrow lvqq$ selection, and VBF resolved WCR for the $WZ \rightarrow lvqq$ selection. Post-fit event yields for electroweak processes and MJ contributions are shown. The SF column shows the corresponding normalization scale factors for electroweak processes from the fit. R.U. stands for relative uncertainty.	113
13.1 Expected and Measured for DY WW $W+jets$, $t\bar{t}$ control regions and signal regions.	133
13.2 Expected and Measured for DY WZ $W+jets$, $t\bar{t}$ tag and untag control regions.	134
13.3 Expected and Measured for DY WZ $W+jets$, $t\bar{t}$ tag and untag signal regions.	135
13.4 Expected and Measured for VBF WW $W+jets$, $t\bar{t}$ control regions and signal regions.	136
13.5 Expected and Measured for VBF WZ $W+jets$, $t\bar{t}$ control regions and signal regions.	137
13.6 Fitted background normalizations for $t\bar{t}$ and $W+jets$ backgrounds for the DY WW analysis region.	138
13.7 Fitted background normalizations for $t\bar{t}$ and $W+jets$ backgrounds for the DY WZ analysis region.	138
13.8 Fitted background normalizations for $t\bar{t}$ and $W+jets$ backgrounds for the VBF WW analysis region.	138
13.9 Fitted background normalizations for $t\bar{t}$ and $W+jets$ backgrounds for the VBF WZ analysis region.	139

Abstract

Search for WW and WZ Resonances in $\ell\nu qq$ final states in pp collisions at

$\sqrt{s} = 13$ TeV with the ATLAS detector

by

Natasha Woods

This thesis presents a search for WW and WZ resonances using data from pp collisions at $\sqrt{s} = 13$ TeV using the ATLAS detector, corresponding to an integrated luminosity of 139 fb^{-1} . Diboson resonances are predicted in a number of Standard Model (SM) extensions, such as Extended Gauge Models, and extra dimensional models. This search looks for resonances where one W boson decays leptonically and the other W or Z boson decays hadronically. This search is sensitive to diboson resonance production via vector-boson fusion (VBF), quark-antiquark annihilation (DY), and gluon-gluon fusion (ggF) mechanisms. No significant excess of events is observed with respect to the SM backgrounds, and constraints on the masses of new W' , Z' , and bulk-RS Gravitons are extended up to 3.7 TeV, depending on the model. As the dominant backgrounds in this search contain gluon-initiated jets, classifying jets as quark-initiated or gluon-initiated increases the sensitivity of this analysis to new physics. Towards this end, this thesis provides a calibrated quark-gluon tagger based on the multiplicity of charged particles within a jet.

For My Parents

Acknowledgments

Organizing this tomorrow From the beginning my parents created a household that fostered curiosity, integrity, and compassion that significantly shaped my life. My sister Alex has been a integral support in my life and has without fail agreed to too many of my hiking trips. My brother Bryce has also agreed to ridiculous trips and helped me see the long-view numerous times I have been caught in short term views. -advisors(Mike, Jason, Vitaliy, Abe, Hartmut)

-physics knowledge(above + Bruce, howie, onnatom, shastry, sher, profumo, platz, jesse, john thompson, allum)

-CERN (toyoko, lenny, dayton, rob, masahiro, lailin, takuya,

-quantitative guidance teachers(croteau, dad, ryan, mom, ben)

-postdocs(ryan, matthew, giordon, simone, hass, akshay)

-grad students(adam, jeff, nico, christian, sheena, peyton, devon, caitlin, alex, alice, steve, devon, katie, coogan, mike, christoph)

-staff(ben, amy, vicki, mykell, cathy, davina)

-personal (mom, dad, alex, bryce, marco, gerard, renae, john, grandma kay, renae, mel, sandra, mike, mckenna, michelle, nedda, christina, verena, bless, ashley, eno, tim, alyssa, ole, sara, kelsey)

Part I

Introduction

Chapter 1

Introduction

In general, humanity has continually strived to understand the structure and dynamics of reality for widely varying reasons. Each academic field uses a specific set of concepts and models to describe nature. Physics, one such field, uses mathematical objects to systematically develop testable models about the universe. The Standard Model (SM) of particle physics describes the quantum behavior of three of the four fundamental forces: electromagnetic, strong, and weak forces. In this theory the most fundamental types particles are fermions and bosons. The ordinary matter of the universe is composed of fermions and bosons are the mediators of the fundamental forces.

The SM has consistently described much of reality with phenomenal accuracy, predicting cross sections for strong and electroweak processes spanning over ten orders of magnitude (see Fig. 3.1). The SM also contains no known logical inconsistencies. Despite the reality of the SM, it still fails to describe certain aspects of reality and suffers from aesthetic issues. The SM fails to explain dark matter, dark energy, neutrino masses, the hierarchy of the fundamental force strengths, and other issues that may have not been noticed yet! This incompleteness may indicate that a more fundamental theory exists. Such a theory would address

the aforementioned phenomena, and the SM’s ad-hoc structures and parameter values. In particular, the relative scales of the fundamental forces impose oddly fine-tuned SM parameters, unless there is additional structure at higher energies (e.g. between the electroweak and Planck scales). This and other theoretical arguments motivate the search for new physics at the TeV scale. The set of theories that hope to explain more of reality are known as Beyond the Standard Model theories (BSM). Many of these theories, if true, would revolutionize concepts of symmetry and space-time, which would be intrinsically meaningful.

To probe the physics at this high energy frontier, physicists often collide energetic particles that combine to produce massive particles, such as the Higgs boson and top quark. The more energetic the colliding particles are the more massive produced particles can be. Presently, the world’s highest energy particle collider is the Large Hadron Collider (LHC) at the European Organization for Nuclear Research (CERN).

This thesis presents a search for WW and WZ BSM resonances using data from pp collisions at $\sqrt{s} = 13$ TeV using the ATLAS detector at CERN, corresponding to an integrated luminosity of 139 fb^{-1} . These diboson resonances are predicted in a number of BSM theories, such as Extended Gauge Models and Extra dimensional models. This search looks for resonances where one W boson decays leptonically and the other W or Z boson decays hadronically. This search is sensitive to diboson resonance production via vector-boson fusion (VBF) as well as quark-antiquark annihilation (DY) and gluon-gluon fusion (ggF) mechanisms (collectively called non-VBF).

To search for these new resonances, Monte-Carlo simulations are used to model SM backgrounds and BSM resonances. In these simulations, a series of optimized cuts are used to create signal regions (SR) to identify the leptonic and hadronic

decay products of the resonance, maximize signal acceptance, and minimize background contamination. In these regions, the resonance mass is calculated as the combined system mass of the leptonic and hadronic system. Thus, the expected resonance mass distribution from the simulated backgrounds and anticipated signal are compared to data to search for the existence of these BSM signals (also known as a bump hunt). Control regions enriched in the dominant backgrounds, $t\bar{t}$ and W +jets (TCR and WCR, respectively) are constructed to be orthogonal to SRs and used to determine the normalization of the $t\bar{t}$ and W +jets backgrounds in SRs.

The VBF W' and Z' and ggF W' and Z' resonances studied have unique SR and CR selections to maximize analysis sensitivity. RS Graviton signals are probed using the same selections as the ggF Z' signal.

More massive resonances are more likely to have boosted W/Z bosons. As the boost of the hadronically decaying boson increases the separation of the decay products decreases. When the hadronically decaying boson has sufficient boost, the two quarks overlap and are not identified separately. For this reason, a set of resolved selections are used when the hadronic decay products are reconstructed separately, and merged selections when the decay products overlap and are identified as a single object in the event. A W/Z tagger identifies merged jets as originating from a W/Z bosons based on jet substructure and mass cuts. However, the more boosted the jet is the less likely it is to pass the jet substructure cut, due to track merging. Consequently, the merged selection uses a high purity region (HP), which requires that the jet pass both cuts, and low purity (LP) region where the jet fails the jet substructure cut.

The aforementioned SR definitions veto events with b -jets to minimize $t\bar{t}$ contamination. However, b -jets are anticipated from W' resonances from the hadron-

ically decaying Z boson. To increase the signal acceptance of these resonances, a $Z \rightarrow bb$ tagger is used to construct additional SR and CRs called the "tagged" regions (and "untagged" if the event fails the $Z \rightarrow bb$ tagger).

For each signal model, the simulated and measured resonance mass distributions in the relevant SR and CRs are combined to construct a likelihood. This likelihood is parameterized by the signal strength parameter, μ , and systematic uncertainties of the resonance mass distribution. This likelihood is used to quantify the likelihood of a certain signal model given the anticipated backgrounds and measured data.

No significant excess of events is observed with respect to SM backgrounds, and constraints on the masses of new W' , Z' , and bulk-RS Gravitons are extended to up to 3.3 TeV, depending on the model. As the dominant backgrounds in this search contain gluon-initiated jets, classifying jets as quark-initiated or gluon-initiated would improve the analysis sensitivity to new physics. Towards this end, this thesis provides a calibrated quark-gluon tagger based on the multiplicity of charged particles within a jet.

Part II reviews the SM, its successes and shortcomings, and the aforementioned BSM theories that address the incompleteness of the SM. The structure and performance of the ATLAS detector used in this search is given in Part III. Part IV summarizes the search for the diboson resonances using ATLAS data from pp collisions at $\sqrt{s} = 13$ TeV. Finally, Part V examines the prospects for a quark gluon tagger based on the track multiplicity of jets and details the calibration of this tagger.

Part II

Theoretical Motivation

Chapter 2

The Standard Model of Particle Physics

2.1 Introduction

By determining the dynamics of the most elementary degrees of freedom, particle physics hopes to uncover the fundamental laws of the universe. The definition of elementary has evolved with time and currently refers to quantum fields, which are operators on spacetime used to compute probability distributions. The quantized excitations of these fields give rise to particles such as the electron. The Standard Model of Particle Physics (SM) describes the interactions between particles due to three of the four fundamental forces: weak, strong, and electromagnetic. Gravity is not included in the SM and still under investigation.

2.2 Quantum Field Theory

In the SM, forces (and particles) are represented as fields. In this context, fields are mathematical objects that define a tensor (e.g. scalar, vector, etc) at

every point on a manifold, here the manifold is space-time. These fields obey laws dictated by Quantum Field Theory (QFT). Particles arise naturally in QFT as quantized field excitations localized in spacetime.

According to Noether's theorem, symmetries of a field give rise to conserved quantities (e.g. time-translation invariance leads to energy conservation). Often in the history of physics, a conserved quantity of a field is found and then the underlying symmetry of the field is inferred. Gauge symmetries are symmetries among the internal degrees of freedom of the field (components of the tensor), which give rise to conserved quantities associated with fields. By specifying the symmetries of a system the dynamics and conserved quantities of the system may be succinctly defined.

2.3 $U(1)_{EM}$ Local Gauge Invariance

The Lagrangian of Quantum Electrodynamics (QED) describes the electromagnetic force. QED may be derived by requiring local $U(1)_{EM}$ gauge invariance of the free Dirac fermion Lagrangian, ψ :

$$\mathcal{L} = i\bar{\psi}\gamma^\mu\partial_\mu\psi - m\bar{\psi}\psi \quad (2.1)$$

This symmetry may be represented as a complex number with unit modulus, $e^{i\theta}$. $U(1)$ gauge invariance requires this gauge transformation of ψ will leave the Lagrangian unchanged:

$$\psi(x) \rightarrow \psi'(x) = e^{i\theta(x)}\psi(x) \quad (2.2)$$

NB: This transformation is a local gauge transformation as θ depends on the spacetime coordinate.

This transformation does not impact the mass term, but the kinetic term is modified due to $\theta(x)$.

$$\mathcal{L} \rightarrow \mathcal{L}' = i\bar{\psi}e^{-i\theta(x)}\gamma^\mu\partial_\mu\psi e^{i\theta(x)} - m\bar{\psi}e^{-i\theta(x)}\psi e^{i\theta(x)} \quad (2.3)$$

$$= i\psi\gamma^\mu(\partial_\mu\psi + i\psi\partial_\mu\theta) - m\bar{\psi}\psi \quad (2.4)$$

The $\partial_\mu\theta$ terms breaks the gauge invariance of the Lagrangian. By introducing a new field, A_μ , the gauge invariance of the derivative can be recovered. Now redefining the derivative as the covariant derivative:

$$D_\mu\psi \equiv (\partial_\mu - iqA_\mu)\psi \quad (2.5)$$

And letting A_μ transform under $U(1)$ as:

$$A_\mu \rightarrow A_\mu + \delta A_\mu \quad (2.6)$$

The transformed covariant derivative becomes:

$$D_\mu\psi \rightarrow D_\mu\psi' = (\partial_\mu - iqA_\mu)\psi' \quad (2.7)$$

$$= (\partial_\mu - iq(A_\mu + \delta A_\mu))\psi e^{i\theta} \quad (2.8)$$

$$= e^{i\theta}D_\mu + ie^{i\theta}\psi(\partial_\mu\theta - q\delta A_\mu)) \quad (2.9)$$

The covariant derivative can be made gauge invariant by setting the last term to zero.

$$\delta A_\mu = \frac{1}{q}\partial_\mu\theta \quad (2.10)$$

So now A_μ transforms as:

$$A_\mu \rightarrow A_\mu + \frac{1}{q} \partial_\mu \theta \quad (2.11)$$

Finally, replacing the derivative with the covariant derivative the Dirac Lagrangian we have:

$$\mathcal{L} = i\bar{\psi}\gamma^\mu D_\mu \psi - m\bar{\psi}\psi - \frac{1}{4}F_{\mu\nu}F^{\mu\nu} \quad (2.12)$$

$$= \mathcal{L}_{QED} \quad (2.13)$$

Here $F_{\mu\nu} \equiv \partial_\mu A_\nu - \partial_\nu A_\mu$. This last term in the Lagrangian is the kinetic energy of the gauge boson field.

So we have derived the QED Lagrangian! By requiring the free Dirac Lagrangian to be invariant under local U(1) transformations we have generated a new gauge boson field, A_μ , which describes the photon. As expected, the photon interacts with fermions.

Stepping back, a global U(1) gauge symmetry of the free Dirac Lagrangian implies we cannot measure the absolute phase of a charged particle. A local U(1) gauge symmetry changes the phase of fields differently across space time. For this type of transformation to leave the Lagrangian invariant, we had to introduce an additional field, A_μ , which "communicates" these phase changes across space-time. In less formal language this effectively means: if the field at one location changes, this change is conferred to other particles via A_μ .

2.4 Yang-Mills Gauge Theories

Requiring $U(1)_{EM}$ gauge invariance of the free Dirac Lagrangian gave us QED. Requiring different gauge symmetries we can derive the structure of other interactions. Any gauge symmetry may be written as:

$$\psi_i \rightarrow \exp(i\theta^a T_{ij}^a) \psi_j \quad (2.14)$$

Here θ is a dimensionless real parameter and T is the generator of the gauge symmetry group. With this, the covariant derivative can be written as:

$$D_\mu \psi_i \equiv \partial_\mu \psi_i + ig A_\mu^a T_{ij}^a \psi_j \quad (2.15)$$

Then the gauge field must transform as:

$$A_\mu^a \rightarrow A_\mu^a - \frac{1}{g} \partial_\mu \theta^a - f^{abc} \theta^b A_\mu^c \quad (2.16)$$

Here f is the structure constant of the gauge group. The field strength tensor is given by:

$$F_{\mu\nu}^a \equiv \partial_\mu A_\nu^a - \partial_\nu A_\mu^a - g f^{abc} A_\mu^b A_\nu^c \quad (2.17)$$

$$F_{\mu\nu}^a \rightarrow F_{\mu\nu}^a - f^{abc} \theta^b F_{\mu\nu}^c \quad (2.18)$$

This gives the Yang-Mills Lagrangian:

$$\mathcal{L}_{YM} = -\frac{1}{4} F_{\mu\nu}^a F_{\mu\nu}^a + i \bar{\psi}_i \gamma^\mu D_\mu \psi_i + m \bar{\psi}_i \psi_i \quad (2.19)$$

2.5 Particles in the Standard Model

The SM is a $SU(3)_C \times SU(2)_L \times U(1)_Y$ Yang-Mills theory, that explains the quantum behavior of electromagnetic, weak, and strong force. It consists of fermions (half-integer spin matter constituents) and bosons (integer spin force mediators). Fermions are spinor representations of the Poincare group and can be further separated into leptons and quarks. Bosons are the result of requiring a particular symmetry among the spinor fields:

$$SU(3)_C \times SU(2)_L \times U(1)_Y \quad (2.20)$$

$SU(3)_C$ is the symmetry group of the strong force and generates eight gluon fields, G_μ . $SU(2)_L$ is the symmetry group of the electroweak force and generates three electroweak boson fields. The mixing of this $SU(2)_L$ and $U(1)_Y$ gives rise to the photon field, where Y is the weak-hypercharge:

$$Y = 2(Q - T_3) \quad (2.21)$$

Q is the electromagnetic charge, and T_3 is the z-component of the weak isospin. Weak isospin is the charge associated with the $SU(2)_L$ symmetry. The corresponding covariant derivative is then:

$$D_\mu \phi \equiv (\partial_\mu + ig_1 B_\mu Y_{L/R} + [ig_2 W_\mu^\alpha T^\alpha]_L + [ig_3 G_\mu^\alpha \tau^\alpha]_C) \psi \quad (2.22)$$

For a given fermion to interact with a given gauge field it must have a non-zero corresponding Noether charge for that gauge symmetry. If the corresponding Noether charge is zero, that fermion transforms as a singlet and does not participate in that gauge interaction.

Fermions are divided into quarks and leptons based on their transformations

under $SU(3)_C$. Quarks transform as color triplets. Leptons transform as color singlets and consequently do not interact with gluons. Fermions may be further classified by their $SU(2)_L$ interactions. Only the left-chiral part of fermions (denoted by L here) transform as $SU(2)_L$ doublets, the right-chiral part forms singlets under this gauge. Lastly, all these groups of particles come in three generations, each a heavier copy of the previous, but with differing flavor quantum numbers.

This is summarized in Table 2.1 and shown in Figures 2.1 and 2.2.

SM Fermion Gauge Group	First Generation	Second Generation	Third Generation	$(SU(3)_C, SU(2)_L, U(1)_Y)$ Representations
Left-handed quarks	$\begin{pmatrix} u_L^r & u_L^g & u_L^b \\ d_L^r & d_L^g & d_L^b \end{pmatrix}$	$\begin{pmatrix} c_L^r & c_L^g & c_L^b \\ s_L^r & s_L^g & s_L^b \end{pmatrix}$	$\begin{pmatrix} t_L^r & t_L^g & t_L^b \\ b_L^r & b_L^g & b_L^b \end{pmatrix}$	$(3, 2, \frac{1}{6})$
Right-handed quarks	(u_R^r, u_R^g, u_R^b) (d_R^r, d_R^g, d_R^b)	(c_R^r, c_R^g, c_R^b) (s_R^r, s_R^g, s_R^b)	(t_R^r, t_R^g, t_R^b) (b_R^r, b_R^g, b_R^b)	$(3, 1, \frac{2}{3})$ $(3, 1, -\frac{1}{3})$
Left-handed leptons	$\begin{pmatrix} \nu_e^L \\ e_L \end{pmatrix}$	$\begin{pmatrix} \mu_e^L \\ \mu_L \end{pmatrix}$	$\begin{pmatrix} \tau_e^L \\ \tau_L \end{pmatrix}$	$(1, 2, -\frac{1}{2})$
Right-handed leptons	e_R	μ_R	τ_R	$(1, 1, -1)$

Table 2.1: Representations of the SM fermions under $SU(3)_C \times SU(2)_L \times U(1)_Y$ gauge symmetry group. Rows are correspond to different weak isospin states and columns to different QCD color states.

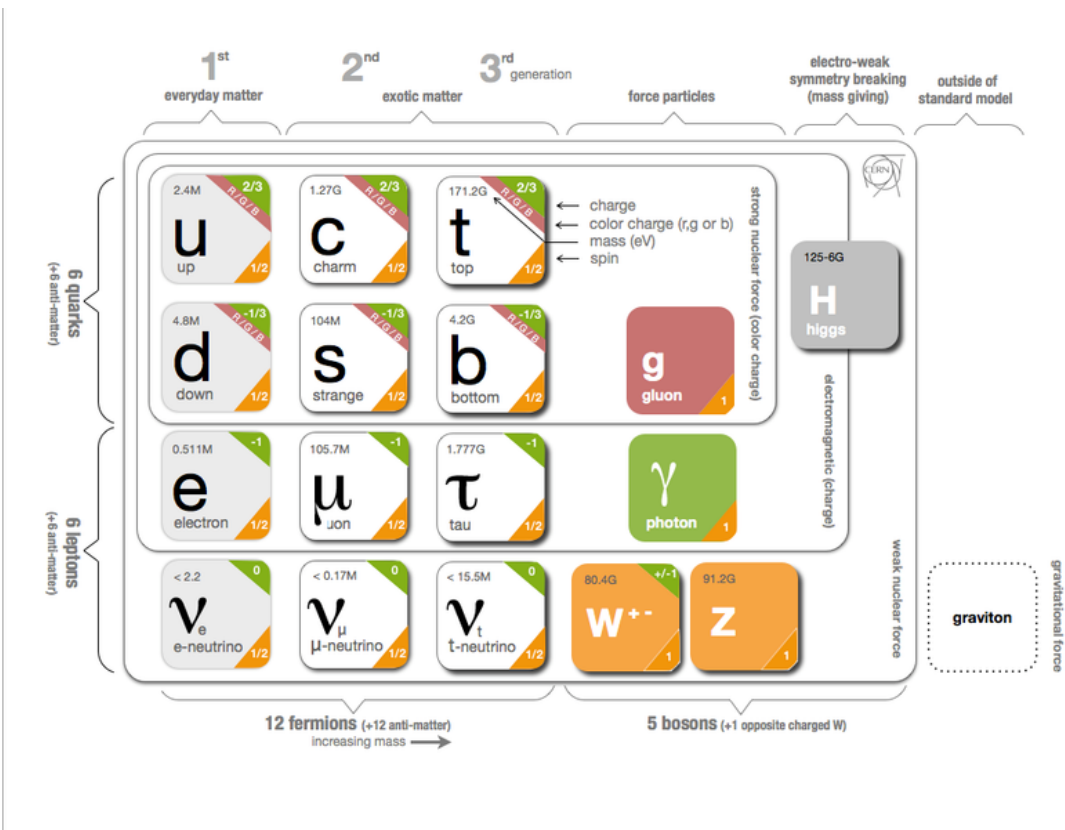


Figure 2.1: The particles of the Standard Model.

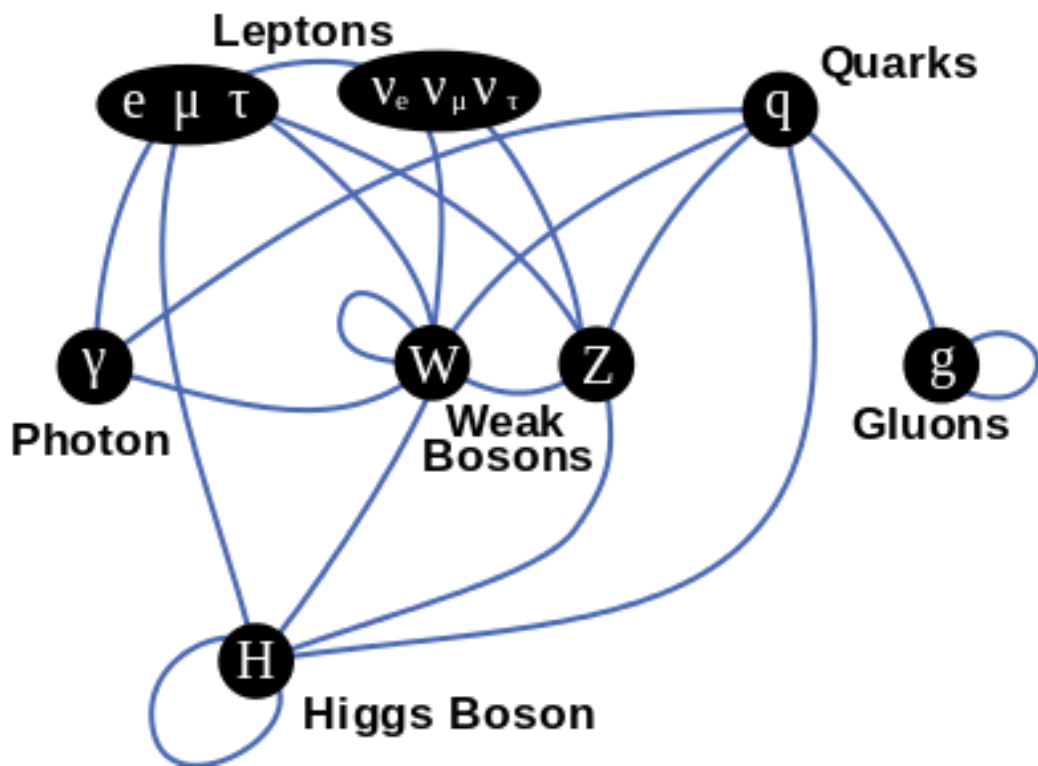


Figure 2.2: Summary of SM particle interactions.

Now we can understand the SM Lagrangian density below as a $SU(3)_C \times SU(2)_L \times U(1)_Y$ Yang-Mills theory with an additional $SU(2)$ complex scalar Higgs field doublet that will be discussed later.

$$\begin{aligned}
\mathcal{L}_{SM} = & \underbrace{-\frac{1}{4}B_{\mu\nu}B^{\mu\nu} - \frac{1}{4}W_{\mu\nu}^a W^{a\mu\nu} - \frac{1}{4}G_{\mu\nu}^\alpha G^{\alpha\mu\nu}}_{\text{Kinetic Energies and Self-Interactions of Gauge Bosons}} \\
& + \underbrace{\bar{L}_i \gamma^\mu (i\partial_\mu - \frac{1}{2}g_1 Y_{iL} B_\mu - \frac{1}{2}g_2 \sigma^a W_\mu^a) L_i}_{\text{Kinetic Energies and EW Interactions of Left-handed Fermions}} \\
& + \underbrace{\bar{R}_i \gamma^\mu (i\partial_\mu - \frac{1}{2}g_1 Y_{iR} B_\mu) R_i}_{\text{Kinetic Energies and EW Interactions of Right-Handed Fermions}} \\
& + \underbrace{\frac{ig_3}{2} \bar{Q}_j \gamma^\mu \lambda^\alpha G_\mu^\alpha Q_j}_{\text{Strong Interactions between Quarks and Gluons}} \\
& + \underbrace{\frac{1}{2} |(i\partial_\mu - \frac{1}{2}g_1 B_\mu - \frac{1}{2}g_2 \sigma^a W_\mu^a)\Phi|^2 - V(\Phi)}_{\text{Electroweak Boson Masses and Higgs Couplings}} \\
& - (\underbrace{y_{kl}^d \bar{L}_k \Phi R_l + y_{kl}^u \bar{R}_k \tilde{\Phi} L_l + h.c.}_{\text{Fermion Mass terms and Higgs Couplings}})
\end{aligned}$$

Here several abstract spaces are being spanned:

- a spans the three $SU(2)_L$ gauge fields with generators expanded in Pauli matrices: $T^\alpha = \frac{1}{2}\sigma^a$
- α spans the eight $SU(3)_C$ gauge fields, with generators expanded in Gell-Mann matrices: $\tau^\alpha = \frac{1}{2}\lambda^\alpha$
- L/R represent left and right projections of Dirac fermion fields. The Strong interaction is not chiral, so $Q = L+R$

- μ and ν are four-vector indices
- i,j,k are summed over the three generations of SM particles

2.6 Higgs Mechanism

The SM Lagrangian without the addition of a Higgs field does not allow for gauge boson and fermion mass terms, $\frac{1}{2}m_A^2 A_\mu A_\mu$ and $m(\bar{\psi}\psi)$, as these terms are not gauge invariant. By introducing the Higgs field, mass terms for these particles may be included in a gauge invariant way. This field is a complex doublet with a potential $V(\Phi)$:

$$\Psi = \begin{pmatrix} \Phi^\dagger \\ \Phi^0 \end{pmatrix} \quad (2.23)$$

$$V(\Phi) = \mu^2 \Phi^\dagger \Phi + \lambda |\Phi^\dagger \Phi|^2 \quad (2.24)$$

The minima of this field occurs for $|\Phi| = \sqrt{\frac{\mu^2}{2\lambda}} \equiv \frac{v}{2}$. This yields degenerate minima, this symmetry is broken by choosing a specific minima (known as spontaneous symmetry breaking). By convention $\Phi_{min} = \frac{1}{\sqrt{2}} \begin{pmatrix} 0 \\ v \end{pmatrix}$ is chosen. This means the ground state of the Higgs field (Higgs vacuum) is non-zero, $\sqrt{\frac{-\mu^2}{\lambda}}$. The Higgs Field may now be expanded around this new ground state as:

$$\Phi(x) = \frac{1}{\sqrt{2}} \begin{pmatrix} 0 \\ v + h(x) \end{pmatrix} \quad (2.25)$$

This non-zero Higgs vacuum generates mass terms for the gauge bosons:

$$|(-\frac{1}{2}g_1 B_\mu - \frac{1}{2}g_2 \sigma^a W_\mu^a)\Phi|^2 = \frac{1}{2}m_W^2 W_\mu^+ W^{-\mu} + \frac{1}{2}m_Z^2 Z_\mu Z^\mu \quad (2.26)$$

where:

$$W_\mu^\pm \equiv \frac{1}{\sqrt{2}}(W_\mu^1 \mp iW_\mu^2) \quad (2.27)$$

$$Z_\mu \equiv \frac{1}{\sqrt{g_1^2 + g_2^2}}(g_2 W_\mu^2 - g_1 B_\mu) \quad (2.28)$$

$$m_W = \frac{v g_2}{\sqrt{2}} \quad (2.29)$$

$$m_Z = \frac{v}{\sqrt{2}} \sqrt{g_1^2 + g_2^2} \quad (2.30)$$

The Higgs field also generates mass terms for fermions and the Higgs boson.

2.7 Electroweak Theory

$SU(2)_L$ generates W^\pm, W^0 gauge bosons, which would be massless if $SU(2)_L$ was a perfect symmetry. These bosons are massive as this symmetry is broken.

Above the electroweak scale (246 GeV) the electromagnetic and weak forces are unified. This can be seen from the mass eigenstates, Z and A_μ given by:

$$\begin{pmatrix} Z_\mu \\ A_\mu \end{pmatrix} = \begin{pmatrix} \cos \theta_W & -\sin \theta_W \\ \sin \theta_W & \cos \theta_W \end{pmatrix} \begin{pmatrix} W_\mu^3 \\ B_\mu \end{pmatrix} \quad (2.31)$$

Here θ_W is the Weinberg angle given by:

$$\cos \theta_W = \frac{g_2}{\sqrt{g_1^2 + g_2^2}} = \frac{m_W}{m_Z} \quad (2.32)$$

2.8 Quantum Chromodynamics

As mentioned earlier the strong force, which binds the proton together, is mediated by gluons. Quantum Chromodynamics is the QFT which describes the

interactions of quarks and gluons via $SU(3)_C$ gauge interactions. QCD contains features not present in electroweak Interactions due to $SU(3)_C$ generators not commuting (i.e. $SU(3)_C$ is a non-abelian group) and the number of quark flavors (n_f). For example, in QCD there is color confinement and asymptotic freedom due to the structure constants being non-zero (to be discussed more later). Requiring $SU(3)_C$ local gauge invariance implies:

$$\psi(x) \rightarrow \psi(x)' = \exp[i g_S \alpha(x) \cdot \hat{T}] \psi(x) \quad (2.33)$$

where $\alpha(x)$ is the local phase function, g_S is the strong coupling constant, and \hat{T} are the eight generators of $SU(3)$ (note $\hat{T}^a = \frac{1}{2}\lambda^a a$, where λ^a are the Gell-Mann matrices). As the Gell-Mann matrices are 3x3, this means ψ has three degrees of freedom under these $SU(3)$ rotations. So, we represent ψ as:

$$\psi = \begin{pmatrix} \psi_{red} \\ \psi_{green} \\ \psi_{blue} \end{pmatrix} \quad (2.34)$$

Physicists describe these components of ψ , as color components (red, green, and blue). A particle's corresponding antiparticle has the corresponding anticolor. This color is the QCD charge which conserved under $SU(3)$ rotations. Combining colors, color neutral states (e.g. red and antired, or red, green and blue) may be created. For the free Dirac Lagrangian to remain invariant under $SU(3)$ transformations, we must again postulate a boson field that modifies the derivative. The gluon field tensor is given by ($\alpha = 1, \dots, 8$):

$$G_{\mu\nu}^k = \partial^\mu G_\alpha^\nu - \partial^\nu G_\alpha^\mu - g_S f^{\alpha\beta\gamma} G_\beta^\mu G_\gamma^\nu \quad (2.35)$$

Here $f^{\alpha\beta\gamma}$ are the structure constants of $SU(3)$. Combining all this gives the

QCD Lagrangian:

$$\mathcal{L}_{QCD} = \bar{\psi}_q i\gamma^\mu (D_\mu)_{ij} \psi^{qj} - m\bar{\psi}^q \psi_q - \frac{1}{4} G_{\mu\nu}^\alpha G^{\alpha\mu\nu} \quad (2.36)$$

Here i are the color indices, and q are the quark flavors. It is important to note that quarks transform under the fundamental representation of $SU(3)$, while gluons transform under the adjoint representation. This means quarks carry a single color charge (red, green, blue, antired, antigreen, antiblue) and gluons carry a color and anticolor charge.

Figure 2.3 shows the three dominant QCD interactions. This figure shows that gluons interact with each other since they have color charge. This does not occur in QED, as photons do not have electric charge and therefore do not interact with each other. In QED, a bare electron's effective charge is largest closest to the electron and decreases as a function of distance. This is because the QED vacuum fills with particle antiparticle pairs spontaneously, which screen the charge of the bare electron. The larger the distance from the electron, the smaller the effective charge and therefore the weaker the force.

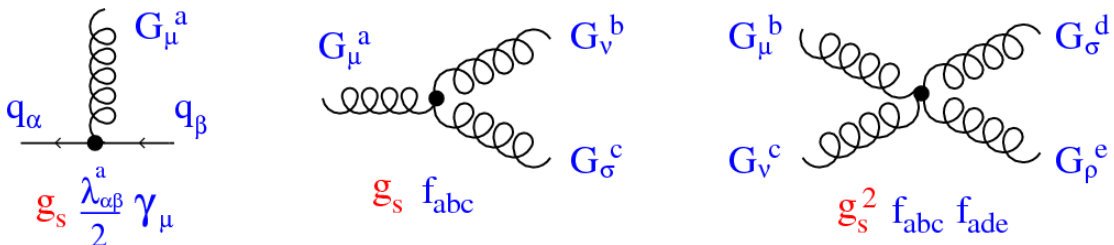


Figure 2.3: This figure shows the three dominant QCD interactions [41] f.

As the distance from a quark increases it's effective color charge increases due to the vacuum polarization in QCD. Color charge grows as the distance from the source increases (i.e. color is anti-screened in QCD). In this way, strong interactions become stronger at large distances (low momenta interactions). At

small distances (large momenta interactions) strong interactions are significantly weaker and considered nearly free. This effect of referred to as asymptotic freedom. At large distances, a quark's effective charge is large and the strong force is more significant. This force becomes so strong that quarks form colorless bound states instead of remaining free particles. This effect is known as color confinement. This scaling of QCD field strength (and the other SM fields) is shown in Figure 2.4.

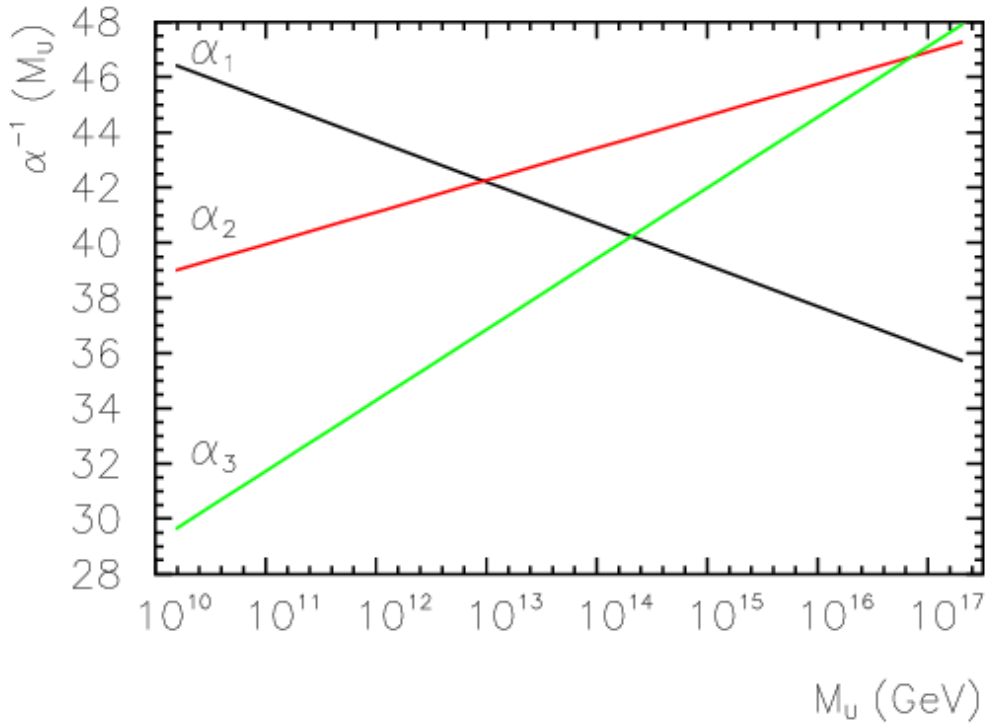


Figure 2.4: Strength of the $U(1)$, $SU(2)$, and $SU(3)$ gauge couplings as a function of the energy scale of the interaction (Q). From Ref. [27]

Commonly the change in a particle's effective charge under a given force is quantified with $\beta(r) \equiv \frac{-de(r)}{d\ln r}$, where $e(r)$ is the effective charge of a given particle under a force. In QED this function is positive but in QCD this function is negative

leading to confinement and asymptotic freedom. Moreover, one can calculate how the coupling (α) of a force varies with energies. More deeply this amounts to incorporating renormalization and vacuum polarization in the boson propagators. For QCD this is:

$$\alpha_s(Q^2) = \frac{\alpha_s(\mu^2)}{1 + \frac{\alpha_s(\mu^2)}{12\pi}(33 - 2n_f)\ln(Q^2/\mu^2)} \quad (2.37)$$

where Q is the momentum of the the force is probed at, μ^2 is the renormalization scale, n_f is the number of quark flavors. There are six quark flavors in SM QCD, making $33 - 2n_f > 0$. Since this factor is positive and the $\ln(Q^2/\mu^2)$ is in the denominator, as Q^2 increases α_s decreases. Meaning, for large Q^2 , α_s is small and SM QCD is asymptotically free, while for small Q^2 , α_s is large and SM QCD is confined, as mentioned earlier.

Particle experiments to date have not observed isolated quarks or gluons due to color confinement. Instead the bound colorless states have been observed. Hadronization is the process by which quarks and gluons form these colorless bound states, called hadrons. The process of hadronization is still an active area of research. One qualitative description is shown in Figure 2.5. In this figure, as two quarks separate the color field between them is restricted to a tube with energy density of 1 GeV/fm. As they separate further, the energy in the color field increases, until there is enough energy to produce $q\bar{q}$ pairs, which breaks the color field. This process repeats until quarks and antiquarks have low enough energy to form colorless hadrons. The resulting spray of hadrons is called a jet.

Since quarks and gluons carry different color charges, their respective jets have different properties. As quarks carry only a single color charge (vs. gluons which have color and anticolor charge), their jets have less constituent particles. More precisely, the Altarelli-Parisi splitting functions [8] contain a factor C_A for gluon

radiation off a gluon, and C_F for gluon radiation off a quark ($C_A/C_F = 9/4$). These color factors are the prefactors in the Feynman diagrams for these processes [?], which leads to gluon jets having more constituents (and more charged particle tracks in detectors) than quark jets. Gluon jets also tend to have a larger radius with lower momentum constituents than quarks. There are many novel techniques to distinguish quarks from gluons. For this study the number of charged particles will be the focus.

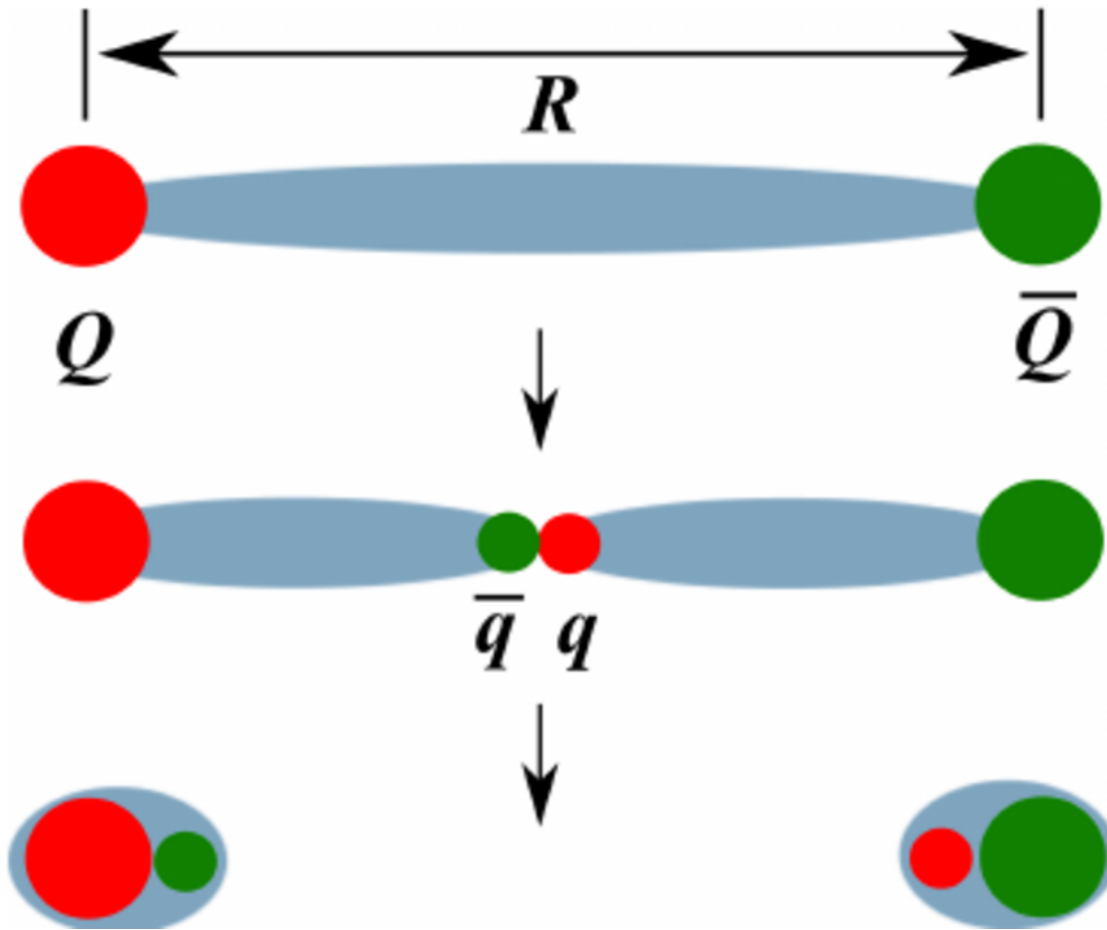


Figure 2.5: A cartoon of string breaking: the QCD string spanned between quark Q and antiquark \bar{Q} breaks due to $q\bar{q}$ creation [13].

Chapter 3

Standard Model Successes and Limitations

The Standard Model has accurately described numerous underlying principles of nature. It has correctly predicted cross sections for strong and electroweak processes spanning over ten orders of magnitude, as shown in Figure 3.1, and contains no known logical inconsistencies. Despite the strength and reality of the Standard Model, it fails to describe some important aspects of reality and suffers from aesthetic issues. To date, dark matter and dark energy comprise $\sim 95\%$ of the universe, but the SM offers no explanation of their nature. Additionally, neutrinos are known to have mass, but the SM contains no mass generation mechanism for left-handed neutrinos without right-handed neutrinos (which do not exist). There are other mechanisms for introducing massive neutrinos in the SM, but these mechanisms create hierarchy problems.

Possibly the most significant aesthetic issue is the hierarchy between the electroweak and Planck scales. The electroweak scale is the scale of electroweak symmetry breaking. The Planck scale is the scale where the gravitational force is comparable in strength to the other forces. The SM breaks down at the Planck

scale, as there is not an experimentally verified theory of quantum gravity, and at this scale gravity cannot be ignored (like it can at the electroweak scale). These scales differ by ~ 30 orders of magnitude. Understanding the difference in these energy scales may help explain the weakness of gravity at electroweak scales, and possibly a QFT for gravity. (NB: This hierarchy can also be framed in terms of the corrections to the Higgs mass, which depend on the UV cutoff scale - where the SM breaks (i.e. the Planck scale). This leads the quantum corrections to the Higgs mass that would force the Higgs mass to $\sim 10^{18}\text{TeV}$.)

These stark contrasts in scales may indicate that a more fundamental theory exists. It is hoped that such a theory would explain and motivate some of the ad-hoc features of the SM. In particular, the SM does not offer an explanation for the values of the 19 SM parameters (6 quark masses, 3 charged lepton masses, 3 gauge couplings, Higgs parameters (μ^2 , λ)) and the structure of the fermion representations.

Standard Model Production Cross Section Measurements

Status: July 2018

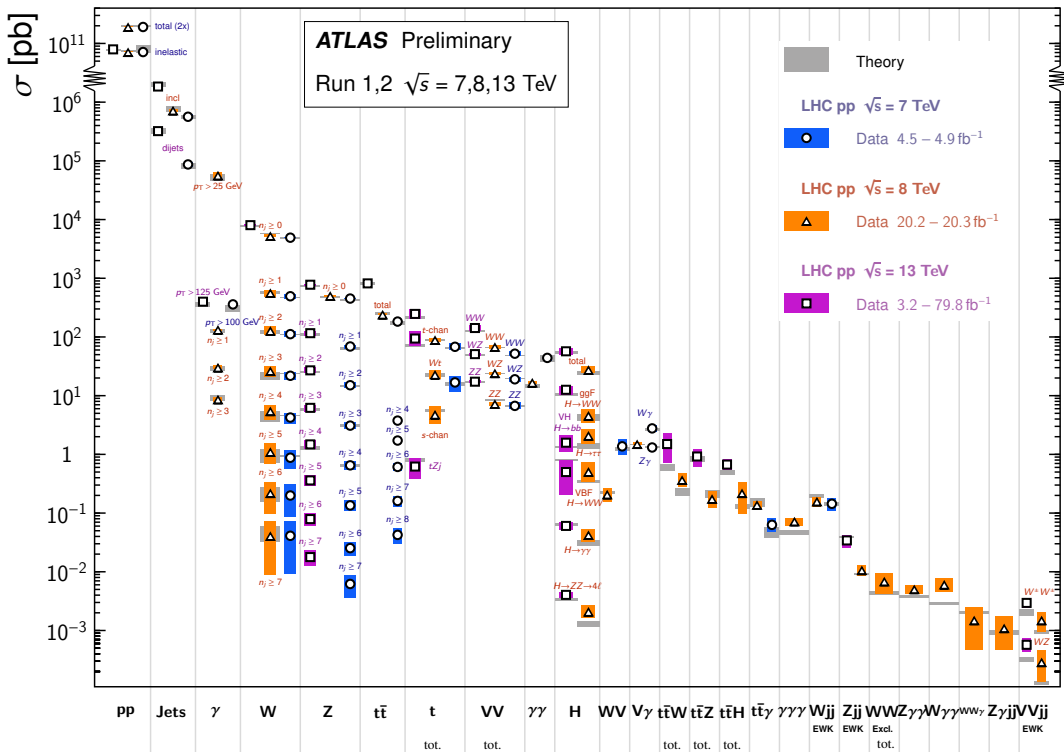


Figure 3.1: A comparison of cross section measurements at $\sqrt{s} = 7, 8, 13$ TeV from ATLAS compared to theoretical measurements. From Ref. [15]

Chapter 4

New Physics Models with Diboson Resonances

4.1 Randall Sundrum Bulk Model

The Planck electroweak hierarchy can be explained in extra dimensional models, such as the 5D Randall Sundrum (RS) Bulk Model ([7],[42]). The RS bulk model posits one extra warped spatial dimension, y , extending a distance L . The metric in this model is:

$$ds^2 = e^{-2k|y|} \eta_{\mu\nu} dx^\mu dx^\nu + dy^2 \quad (4.1)$$

where $e^{-k|y|}$ is the warp factor of the extra dimension, which is compactified on a S^1/Z_2 orbifold (i.e. a circle where $y \rightarrow -y$). This can be visualized as every point in space time having a line extending from it a distance L , representing this fifth dimension. At the end of this line is the Planck brane. This fourth spatial dimension separates two 4-D branes: Planck brane and TeV brane. We live on the TeV brane, as shown in Figure 4.1. The Higgs field (and to a lesser degree

the top quark and graviton fields) is localized near the TeV Brane, while the light fermion fields are localized closer to the Planck brane.

Fundamental parameters are set on the Planck brane. The warp factor may be scaled away from all dimensionless SM terms by field redefinitions. However, the only dimensionful parameter, $m_H^2 = v^2$ is rescaled by $\tilde{v} \sim e^{-kL} M_{Pl} \sim 1\text{TeV}$ for $kL \sim 35$. So, the electroweak and Planck scales are consistent on the Planck brane, and only the electroweak scale is significantly warped down on the TeV brane, explaining the large difference between the two scales. Also, by the localization of the light fermion fields near the Planck brane and top and graviton fields near the TeV brane provides an explanation for the fermion mass hierarchy.

The two free parameters of this theory are M_{Pl} and k . Based on this RS Bulk model, all SM particles should have Kaluza-Klein (KK) excitations. In particular, the graviton would have KK excitations (G_{KK}) that prefer to decay to WW or ZZ . This search is sensitive to the WW decay mode.

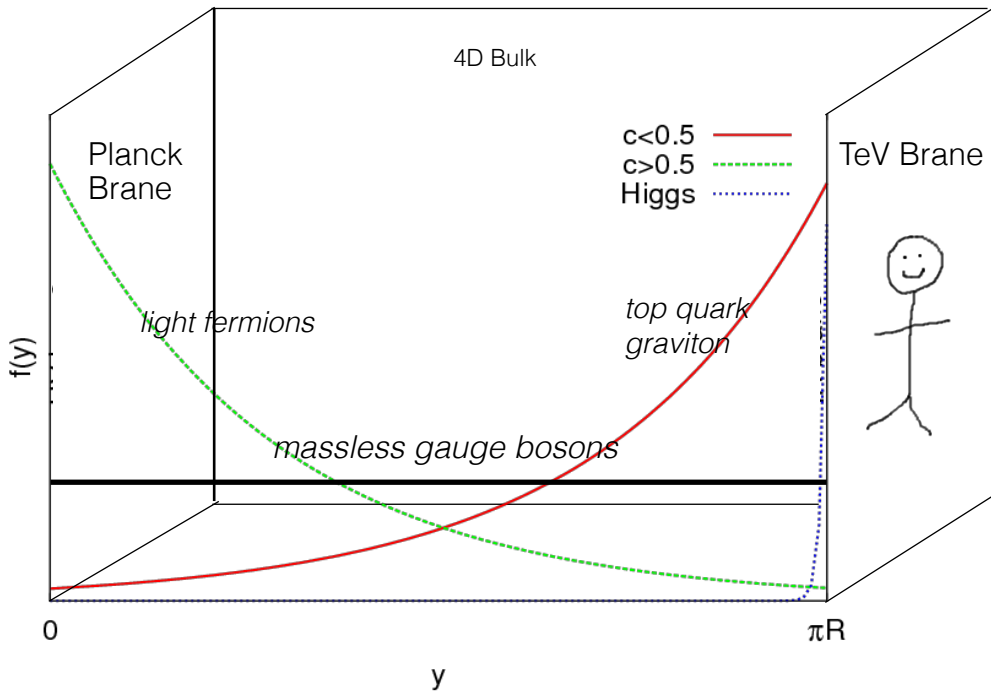


Figure 4.1: Cartoon of RS Bulk Model

4.2 Simple Standard Model Extensions

The RS Bulk model is motivated by resolving SM hierarchies, but it does not address other SM issues. There are many other interesting and well motivated new physics frameworks that address these issues, but there is a lack of completely predictive models, due to model flexibility (free parameters). It is difficult for experimentalists to know which theories to search for in data. Therefore, developing a model-independent resonance search that can be reinterpreted in the context of a given BSM theory is ideal.

This search is sensitive to the resonance mass and its couplings, but not all of a given BSM model's parameters. Therefore, the BSM Lagrangian may be reduced to only retain this information (mass parameters and couplings) following the procedure in [40]. In this simplified approach, the new resonance searched for is

represented as an additional heavy vector triplet (HVT), which is a real vector field in the adjoint representation of $SU(2)_L$ with vanishing hypercharge. This results in one neutral and two charged bosons, defined as:

$$V^\pm = \frac{V_\mu^1 \mp i V_\mu^2}{\sqrt{2}} \quad (4.2)$$

$$V_\mu^0 = V_\mu^3 \quad (4.3)$$

The SM Lagrangian is then augmented with the additional terms:

$$\mathcal{L} \supset -\frac{1}{4} D_{[\mu} V_{\nu]}^a D^{[\mu} V^{\nu]a} + \frac{m_V^2}{2} V_\mu^a V^{a\mu} + ig_V c_H V_\mu^a H^\dagger \tau^a \overset{\leftrightarrow}{D}^\mu H + \frac{g^2}{g_V} c_F V_\mu^a J_F^{\mu a} \quad (4.4)$$

In order the terms represent: the kinetic, V mass, Higgs- V interaction, and V -left-handed fermion interaction terms. The g_V coupling factor determines the coupling of the new resonance to left-handed fermions and the Higgs boson.

As benchmark models, this search considers resonances from Extended Gauge Models (EGM) and composite Higgs models as discussed in [40]. The EGM model predicts weakly coupled resonances, where $g_V = 1$, referred to later as Model A. The composite Higgs Model is a strongly coupled model, where $g_V = 3$, and later referred to as Model B. As shown in Eq. 4.4, the coupling of these resonances to fermions scales as $g_f = g^2 c_F / g_V$, where g is the SM $SU(2)_L$ gauge coupling and c_F is a free model parameter. Therefore in Model B, the coupling to fermions is suppressed relative to Model A, leading to a smaller DY production rate and branching ratio (BR) to fermionic final states. The coupling of V to SM bosons scales as $g_H = g_V c_H$, where c_H is a free model parameter on the order of one for Model A and B. Consequently Model A resonances have a smaller the BR to gauge bosons than Model B. For the pp collision data used, Model A predicts larger production cross sections decaying to leptons and fermions than Model B

which decays primarily to gauge bosons.

Model A and B vectors are produced via quark-anti-quark annihilation and vector-boson-fusion. Both production modes are probed in this search.

Part III

Experimental Setup

Chapter 5

LHC

The Large Hadron Collider (LHC) is currently the highest-energy particle collider in the world. It was designed to expand the frontier of high energy particle collisions in energy and luminosity. This enables LHC experiments to test the Standard Model and search for new physics at higher energies than tested with previous colliders. Collisions at higher energies not only produce more massive particles but also more weakly interacting particles. Fig 5.1 shows production cross sections for various processes at hadron colliders. The rate for electroweak physics processes including W and Z scale with the center-of-momentum energy, \sqrt{s} .

The LHC consists of a 26.7 km (17 miles) ring, approximately 100 m underground, outside Geneva, Switzerland. Counter-circulating proton (and occasionally heavy ions) beams collide inside four experiments along the beam line: ATLAS, CMS, LHCb, ALICE. ATLAS and CMS are general purpose detectors designed to explore the high energy frontier. LHCb is designed to study the physics of b -quarks. ALICE specializes in studying heavy ion collisions.

proton - (anti)proton cross sections

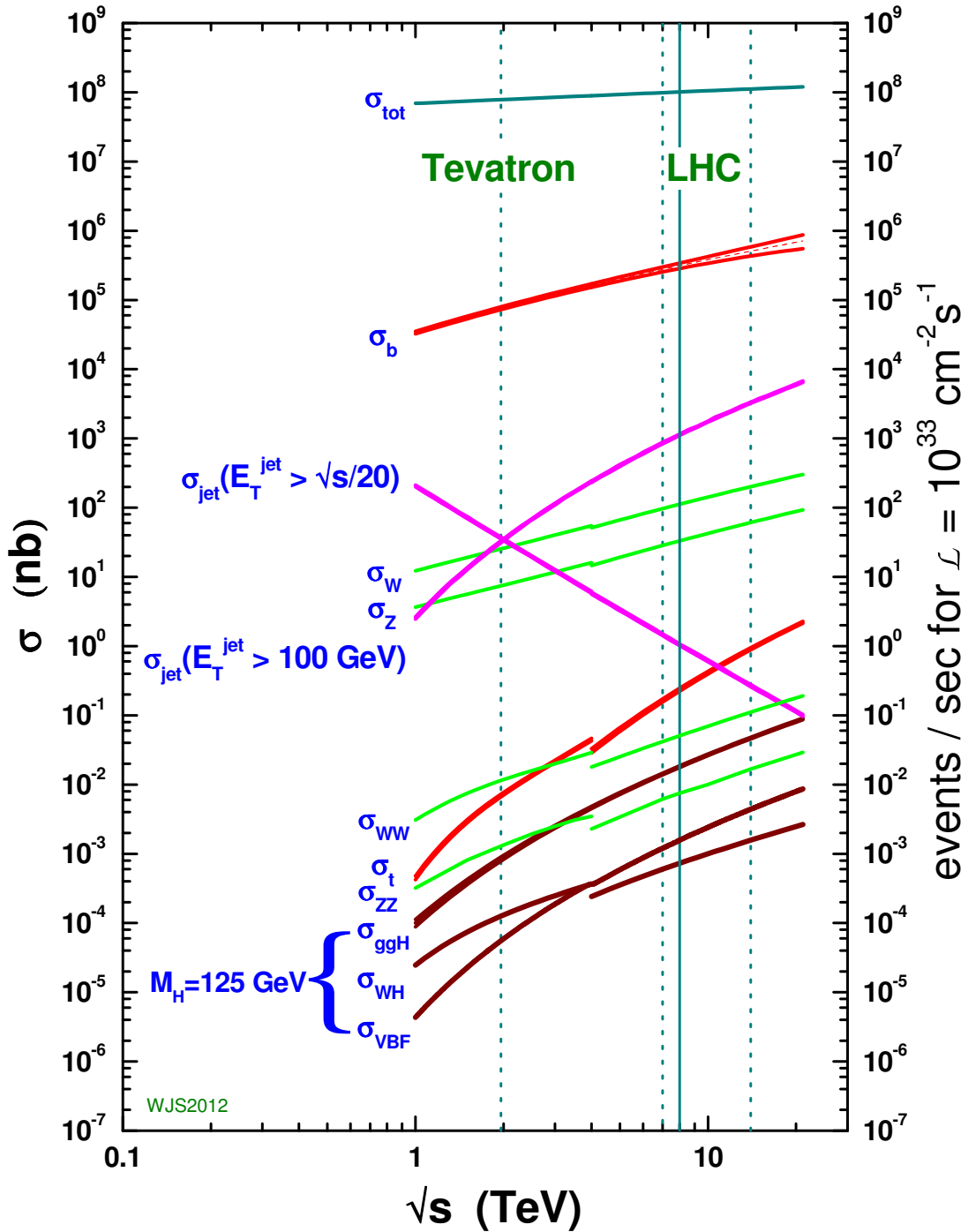


Figure 5.1: Scaling of various SM cross sections with \sqrt{s} .

The first proton beams circulated in September, 2008. Nine days later an electrical fault lead to mechanical damage and liquid helium leaks in the collider. This incident delayed further operation until November 2009, when the LHC became the world’s highest energy particle collider, at 1.18 TeV per beam. This first operational run continued until 2013, reaching 7 and 8 TeV collision energies. During this run a particle with properties consistent with the SM Higgs boson was discovered. The next run began following a two year shutdown for upgrades to the LHC and experiments. That run lasted from 2013 to 2018 reaching 13 TeV collision energies. This analysis uses data from the second run.

5.1 LHC Layout and Design

The layout of the LHC is shown in Figure 5.2. The red and blue lines in the figure represent the counter-circulating proton beams. The LHC is divided into eight octants. Octant 4 contains the RF cavities that accelerate the protons and octant 6 contains the beam dump system. Octants 3 and 7 house the collimation systems for beam cleaning. The beams collide inside the four aforementioned experiments. The LHC magnets are built with NbTi superconductors cooled with super-fluid Helium to 2K, creating a 8.3T magnetic field to bend the proton beams.

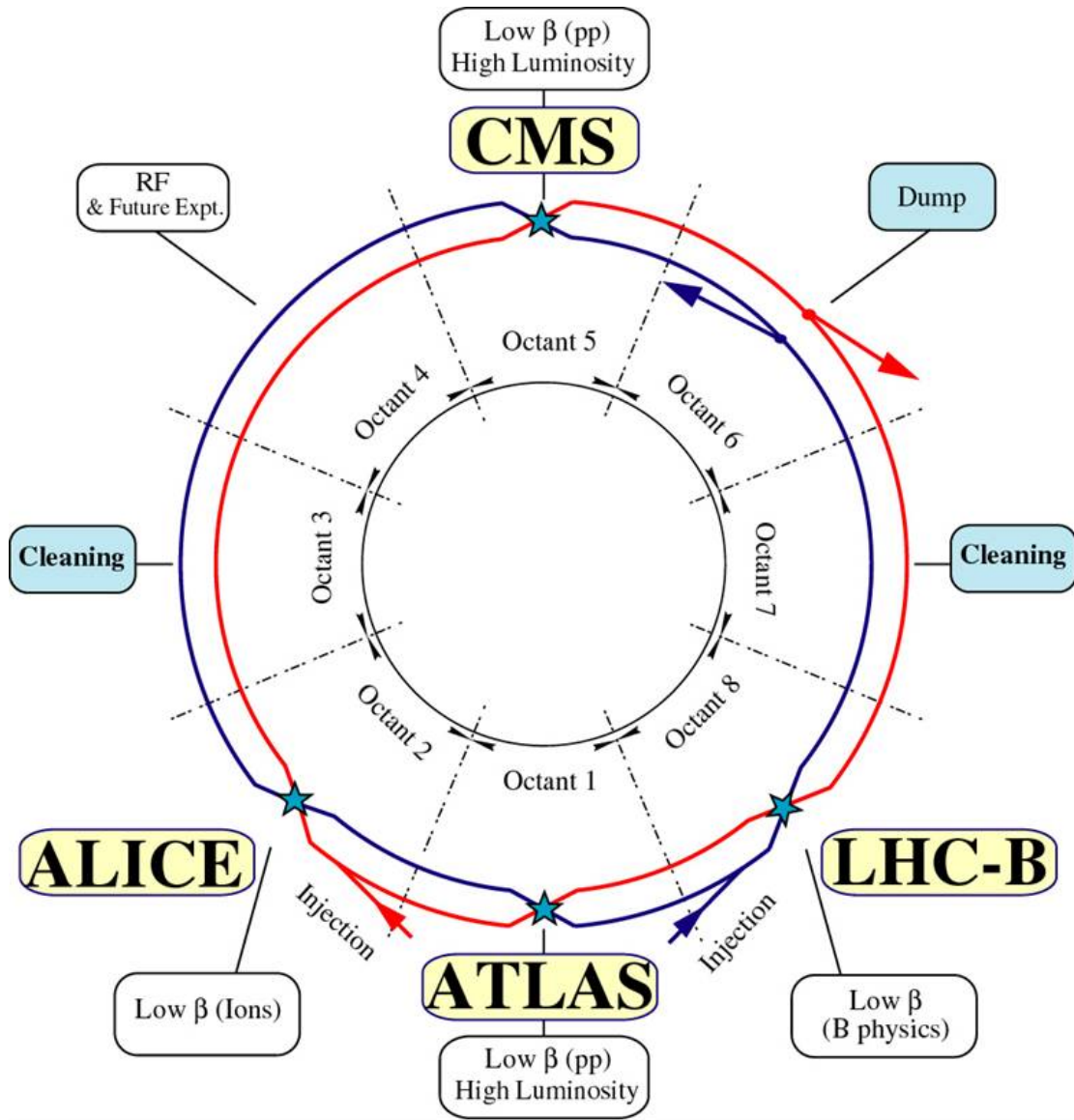


Figure 5.2: The layout of the LHC and the four detectors along the beam line (ATLAS, LHCb, ALICE, CMS).

Four sequential particle accelerators are used to accelerate protons from rest as shown in Figure 5.3. First, Hydrogen gas is ionized to produce protons which are then accelerated to 50 MeV using Linac 2, a linear accelerator. The resulting proton beam is then passed to three circular particle accelerators: Proton Synchrotron Booster, Proton Synchrotron, and Super Proton Synchrotron (SPS),

accelerating protons to 1.4, 25, and 450 GeV, respectively. Once the protons exit the SPS, they are injected into the LHC at octant 2 and 8. Each proton bunch contains $\sim 10^{11}$ protons. The spacing between bunches is 25 ns, which means each beam contains 3564 bunches. However, some bunches are left empty due to injection and safety requirements, yielding 2808 bunches per beam. Once the proton beams are injected they are accelerated to 13 TeV.

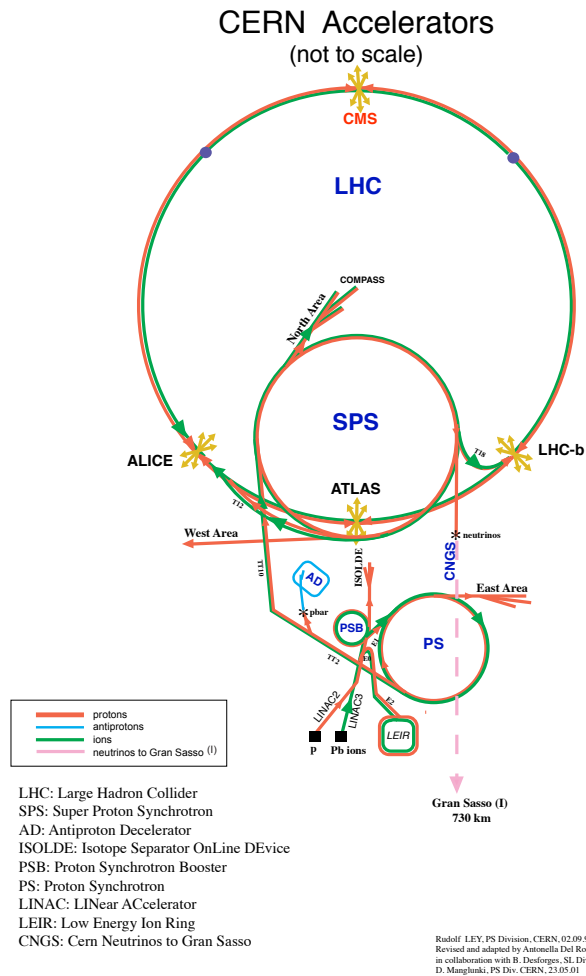


Figure 5.3: An overview schematic of the LHC accelerator subsystems.

Many new physics models predict cross-sections below the electroweak scale. To detect this rare processes, the LHC was designed to operate in high luminosity

conditions, increasing the likelihood of BSM physics in data. The LHC machine luminosity, L , depends only on beam parameters:

$$L = \frac{N_p^2 f}{4\epsilon\beta^*} F \quad (5.1)$$

where N_p is the number of protons per bunch, f is the bunch crossing frequency, ϵ is the transverse beam emittance, β^* is the amplitude function at the collision point, and F is the geometric luminosity reduction factor due to the beams crossing at an angle.

Chapter 6

The ATLAS Detector

The ATLAS detector measures the position, momentum and energy of particles produced in the proton collisions by using magnetic fields, silicon detectors, sampling calorimeters, and gaseous wire detectors. It is located approximately 100 m underground at Point-1 around the LHC beam line and weighs 7000 metric tons. The detector is 46 m long, 25 m high, 25 m wide as shown in Figure 6.1. The detector can be divided into three subsystems: the Inner Detector (ID), the Calorimeters, and the Muon Spectrometer (MS). Figure 6.2 provides an overview of how different particles interact in the detector.

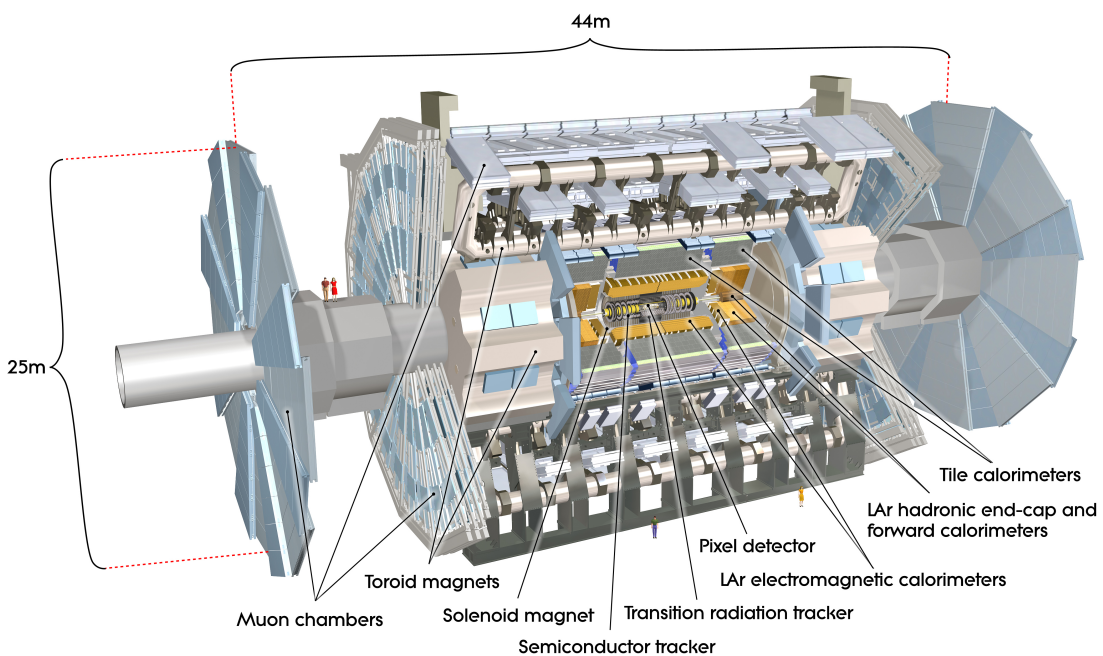


Figure 6.1: Overview schematic of the ATLAS detector.

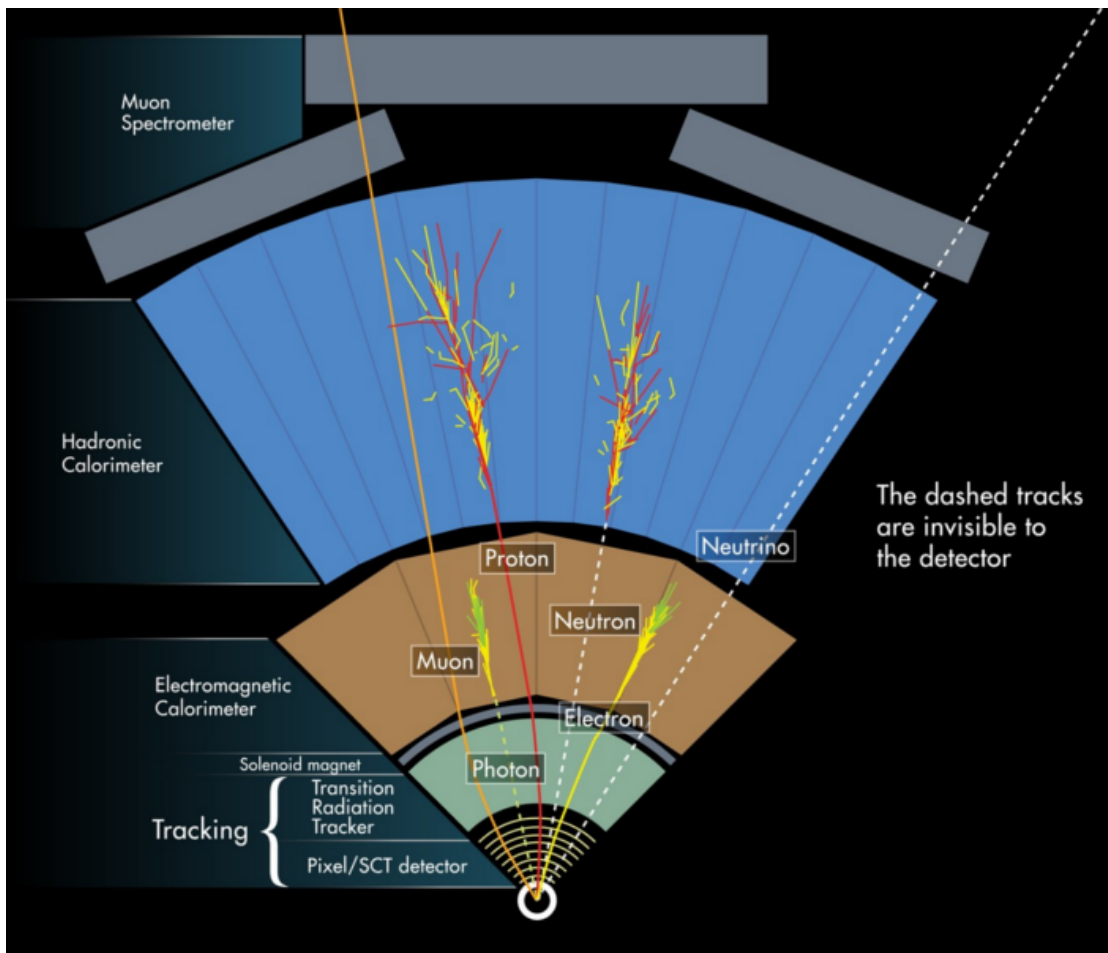


Figure 6.2: A cartoon of how different particles interact and are detected within ATLAS.

6.1 Coordinate System

The trajectory of particles within ATLAS is measured relative to the nominal interaction point. The z -axis points along the beam line, such that when the LHC is viewed from above, the counter-clockwise circulating beam points along the positive- z direction. The $x - y$ plane is transverse to the beam line, with the positive x -axis pointing towards the center of the LHC ring. The positive y -axis points vertically upward. The azimuthal angle, ϕ , is the angular distance about the z -axis, with $\phi = 0$ along the x -axis. The polar angle from the z -axis is denoted as θ . However, this quantity is not Lorentz invariant, like rapidity, $y = \frac{1}{2} \ln \frac{E+p_z}{E-p_z}$, where E is the energy of the particle considered, and p_z , is it's momentum along the z -axis. Pseudorapidity, a related quantity, is defined as: $\eta = -\ln \tan(\frac{\theta}{2})$. It is preferred quantity as it is invariant under boosts along z , particle production is approximately invariant under η , and it is a purely geometric quantity. This quantity is preferred as it is purely a geometric quantity, independent of particle energy.

The angular separation(in $\eta - \phi$) between particles in ATLAS is defined as $\Delta R = \sqrt{\Delta\eta^2 + \Delta\phi^2}$. The distance from the beamline is given by $r = \sqrt{x^2 + y^2}$

6.2 Inner Detector

The Inner Detector (ID) was designed to identify and reconstruct vertices, distinguish pions from electrons, and measure the momentum of charged particles. The ID uses three different technologies for particle reconstruction: the Pixel Detector, Semiconductor Tracker (SCT), and the Transition Radiation Tracker (TRT), shown in Figure 6.3 and 6.4. The entire ID is immersed in a 2 T solenoidal magnetic field parallel to the $+z$ -axis, causing charged particles to bend in the

transverse-plane, allowing particle momentum measurements.

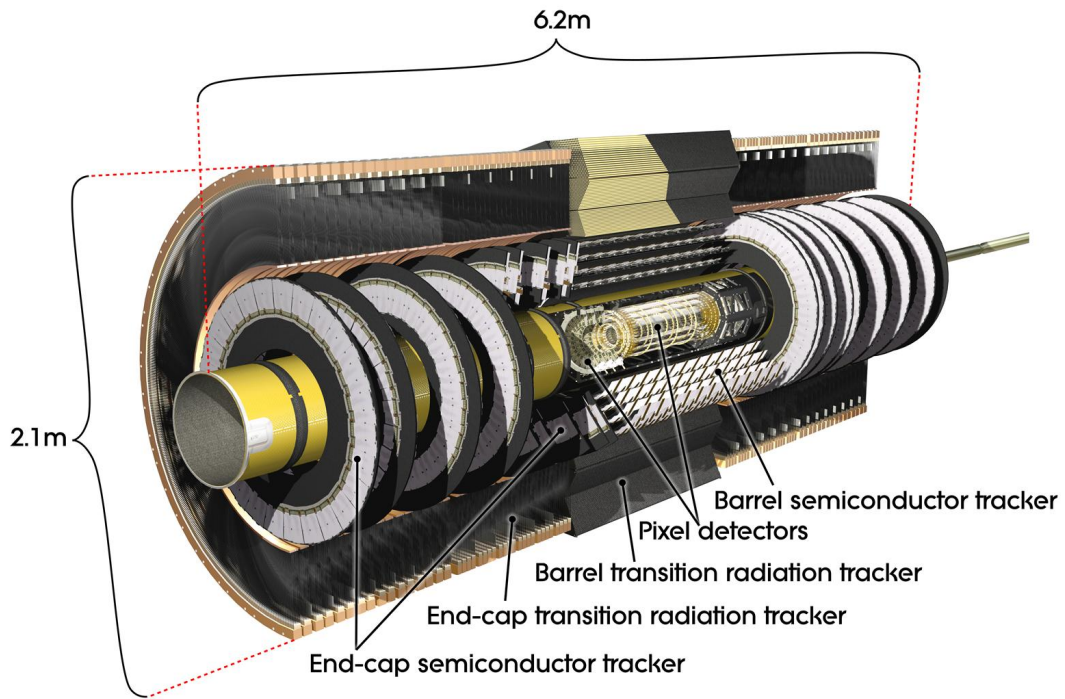


Figure 6.3: Layout of ATLAS Inner Detector

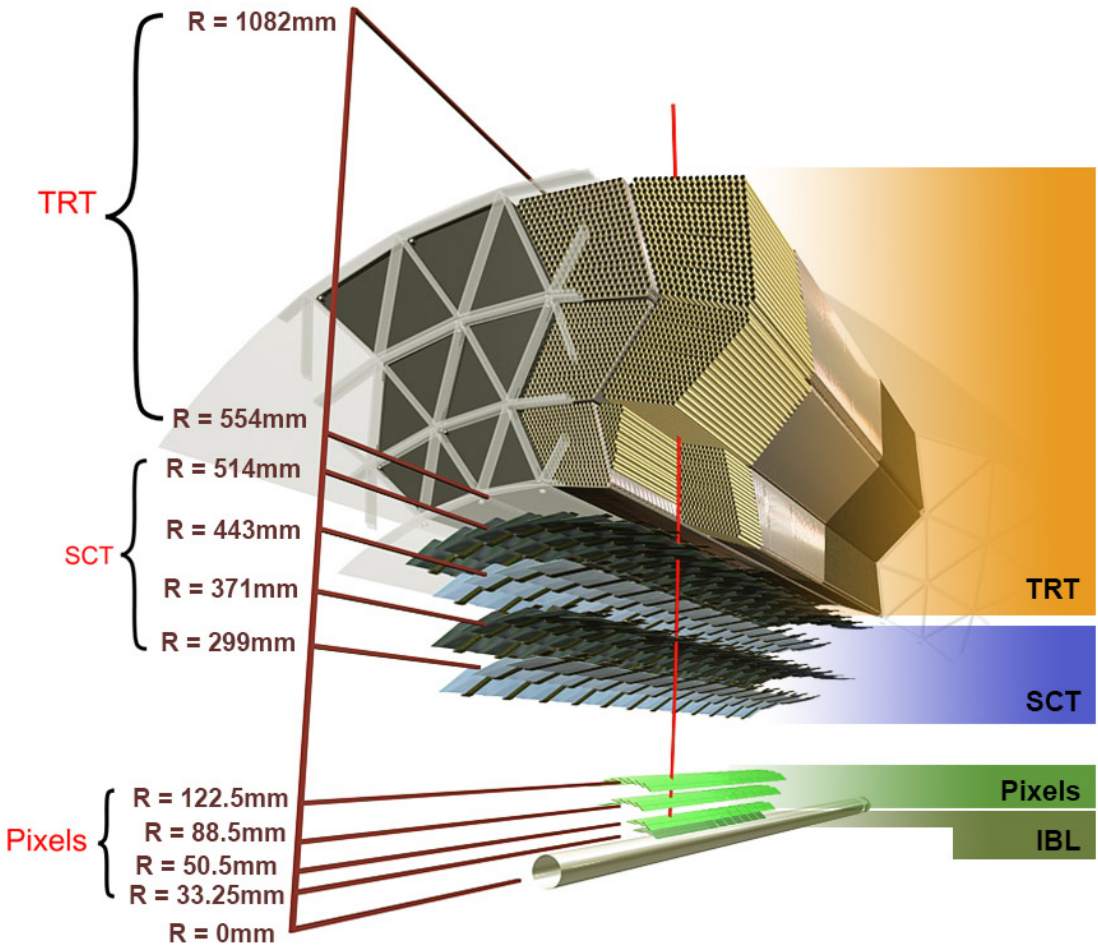


Figure 6.4: Layout of ATLAS ID Barrel System.

6.2.1 Pixel Detector

The pixel detector consists of four barrel layers between $r = 32.7$ and 122.5 mm, extending to $|z| = 400.5$ mm. The remaining detectors are arranged in barrels and forward and backward rings. The innermost pixel barrel, the Insertable b-Layer (IBL), only extends to $|z| = 332$ mm. The pixel detectors closer to the beam line (larger η values) consist of six parallel cylindrical rings of pixel detectors transverse to the beam line. The entire pixel detector consists of 1,744 identical pixel sensors each with 46,080 readout channels, totaling about 80 million individual pixels. Most of the pixel sensors are $50 \times 400 \mu\text{m}^2$. Each pixel has

a position resolution of $14\mu\text{m}$ in ϕ and $115\mu\text{m}$ in the z direction.

6.2.2 Semiconductor Tracker

The SCT is located outside the pixel detector and has the same barrel and endcap geometry as the pixel detector. SCT sensors are $80\mu\text{m} \times 12\text{ cm}$ with a $80\mu\text{m}$ strip pitch. In the barrel the strips are parallel to the z -axis and are segmented in ϕ . In the endcaps, the strips extend radially. Sensors are grouped in modules containing two layers of strips rotated 40 mrad with respect to each other. This offset allows for the two-dimensional position of a track to be determined by identifying the crossing point of the strips that registered a hit. SCT modules measure tracks with an accuracy of $17\mu\text{m}$ in $r - \phi$ and $580\mu\text{m}$ in $z(r)$ in the barrel (end-cap) region.

6.2.3 Transition Radiation Tracker

The transition radiation tracker (TRT), enveloping the SCT, is a gaseous straw-tube tracker mainly used for electron/pion discrimination. Each straw is 4 mm in diameter and filled with a Xe-CO₂-O₂ gas mixture. An anode wire at the center of the straw is held at ground potential, while the walls of the straw are kept at -1.4 kV. When a charged particle passing through the TRT ionizes the gaseous mixture, the resulting ions form an avalanche on the anode wire with a gain of $\sim 10^4$. The signal from the anode wire is then digitized and discriminated. Signals passing a low threshold cutoff are used to distinguish noise from tracks. Signals passing a high threshold cutoff are sensitive to transition radiation (TR). TR photons are emitted when charged particles pass between materials with different dielectric constants. The probability that a charged particle with energy E and mass m passing between two materials emits a TR photon in the keV range is

proportional to $\gamma = E/m$. In the TRT staws, these photons often then convert via the photoelectric effect, causing a large avalanche triggering the high-threshold. Since electrons have a smaller mass than pions, electron tracks are more likely to trigger the high threshold.

The barrel region of the TRT extends from $r = 563\text{-}1066$ mm and $|z| < 712$ mm. Barrel Straws are 144 cm long (divided at $\eta \approx 0$) and orientated parallel to the beam direction. End-cap straws extend radially and are 37 cm long. There are 53,544 straws in the barrel and 160,000 straws in the end-caps. Radiator mats of polypropylene/polyethylene fibers in the barrel are aligned perpendicular to the barrel straws (with holes for the straws to pass through). In the end-cap region, radiator foils are layered between the radial TRT straws.

The arrival time of a TRT pulse is sensitive to the distance between the corresponding charged particle track and the anode wire and allows for a hit resolution of $130\text{ }\mu\text{m}$. The TRT extends to $|\eta| = 2.0$ and provides about 36 hits per track.

6.3 Calorimeters

The ATLAS electromagnetic and hadronic calorimeters (ECAL and HCAL, respectively) absorb and measure the energy of high energy hadrons, photons, and electrons with $|\eta| < 4.9$. Both systems use sampling calorimeters which consist of alternating layers of dense absorbing and active layers. In the absorbing layer particles interact and lose energy, creating showers of particles. These showers are detected and measured in the active layer. The amount of charge measured in the active material scales with the energy of the incident particle, and thus provides a measurement of the particle's energy. An overview of the layout of the calorimeter system is shown in Figure 6.5.

The ECAL measures and contains the energy of electromagnetically interact-

ing particles. It consists of layered accordion-shaped Lead absorber plates and electrodes immersed in liquid Argon with 170k channels. Using accordion-shaped electrode and absorbers ensures ϕ symmetry and coverage. The ECAL is composed of a barrel ($|\eta| < 1.475$), two end-caps ($1.375 < |\eta| < 3.2$), and a presampler ($|\eta| < 1.8$). The presampler, containing only liquid Argon, corrects for upstream energy losses of electrons and photons. The ECAL barrel is segmented into three layers. The first layer has finest segmentation with readout cells extending $\Delta\eta \times \Delta\phi = 0.025/8 \times 0.1$. This provides a precise shower measurements used to separate prompt photons from $\pi^0 \rightarrow \gamma\gamma$ decays. The second layer has coarser segmentation and is approximately 16 radiation lengths long. A radiation length is the average distance an electron travels before losing all but $1/e$ of its energy via bremsstrahlung. The last layer is the most coarse and measures the tail of the electromagnetic shower. A schematic of the ECAL is shown in Figure 6.6.

The hadronic calorimeter located outside the ECAL and is used to contain and measure the energy of hadronically interacting particles. It consists of a tile calorimeter (TileCal), hadronic end-cap calorimeter (HEC), and liquid Argon forward calorimeter (FCAL). TileCal is located behind the ECAL and uses steel absorbers and liquid Argon as the active material. TileCal consists of three barrel layers in the central and forward regions, extending up to $|\eta| < 1.7$. Photons generated from hadronic interactions are collected via wavelength-shifting fibers connected to photomultiplier tubes, as shown in Figure 6.7. The HEC lies behind the ECAL endcap wheels. It uses Copper absorbers and liquid Argon as the active material and covers $1.5 < |\eta| < 3.2$. Finally, the FCAL covers $3.1 < |\eta| < 4.9$ and consists of three modules all using liquid Argon as the active material. The first module uses copper absorber and was designed for electromagnetic measure-

ments. The second and third modules consist of tungsten absorber and are used to measure the kinematics of hadronically interacting particles. A schematic of the HCAL is shown in Figure 6.7.

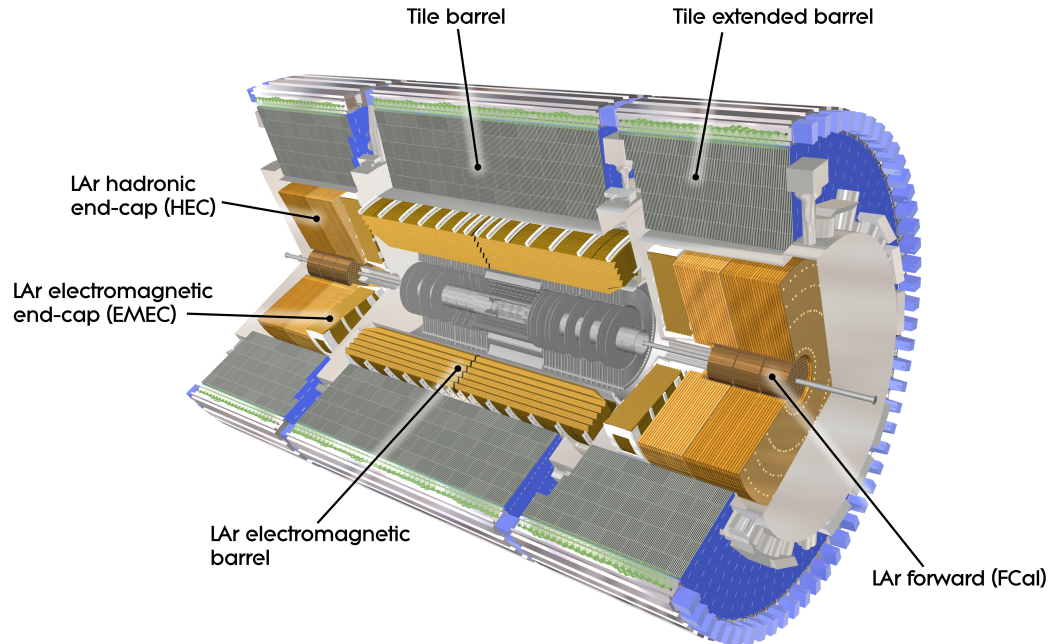


Figure 6.5: Overview of ATLAS electromagnetic and hadronic calorimeters.

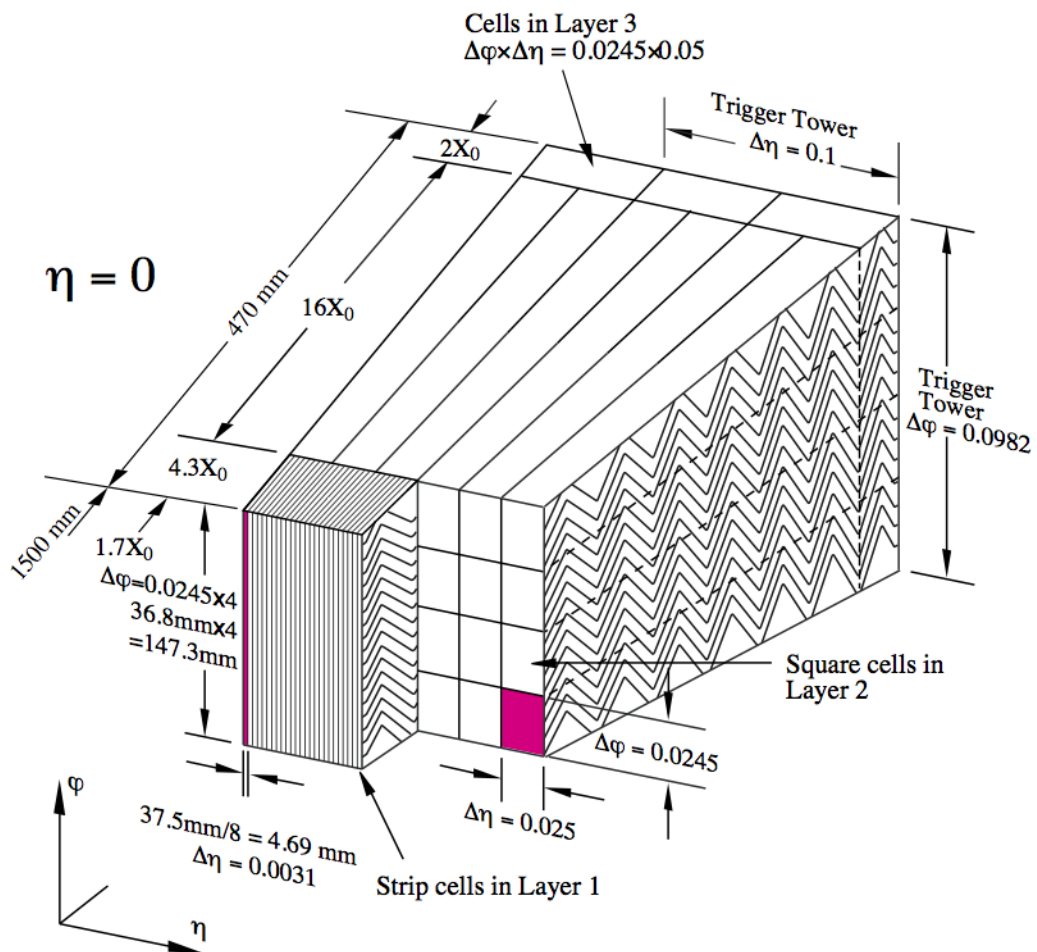


Figure 6.6: Schematic of ECAL.



Figure 6.7: Schematic of HCAL.

The energy resolution of the calorimeter subsystems are:

$$\frac{\sigma_E}{E} = \frac{10\%}{\sqrt{E}} \oplus \frac{0.3\%}{E} \oplus 0.4\% \text{ Electromagnetic Calorimeter}$$

$$\frac{\sigma_E}{E} = \frac{50\%}{\sqrt{E}} \oplus \frac{1.8\%}{E} \oplus 3\% \text{ Hadronic Calorimeter}$$

6.4 Muon Spectrometer

The muon spectrometer (MS) is the outermost detector system in ATLAS. Muons with a $p_T > 4$ GeV are energetic enough to reach the MS. To measure the momentum of these muons barrel and end-cap toroid magnets are used covering $|\eta| < 1.4$ and $1.6 < |\eta| < 2.7$. For $1.4 < |\eta| < 1.6$, a combination of the barrel and end-cap toroidal magnetic fields bend muon trajectories. The detector in the barrel region forms three concentric rings at $R = 5, 7.5, 10$ m and is segmented in ϕ to accommodate the magnet system. The end-cap region consists of three circular planes perpendicular to z and located at $|z| = 7.4, 14, 21.5$ m from the interaction region. An additional detector at $|z| = 10.8$ m covers the transition region between the barrel and end-cap.

The MS readout consists of four subsystems: Monitored Drift Tubes (MDT), Cathode Strip Chambers (CSC), Resistive Plate Chambers (RPC), and Thin Gap Chambers (TGC). The first two subsystems are used primarily for measuring muon track parameters, while the RPC and TGC subsystems are used for muon triggering. A schematic of this system is shown in Figure 6.8.

The MDT subsystem consists of precision tracking chambers for $|\eta| < 2.7$, except for the inner most end-cap layer ($2.0 < |\eta| < 2.7$), where CSCs are used. The basic unit of MDT chambers are thin walled Aluminum tubes with a diameter of 3 cm and length of 0.9-6.2 m. These tubes are filled with a mixture of Ar-CO₂ gas with a 50 μm W-Rn wire running down the center of the tube, which is kept at 3080 V. Since the maximum drift time of these chambers is ~ 700 ns, they are not

used for triggering. MDT chambers consist of 3-4 layers of tubes mounted on a rectangular support system, as seen in Figure 6.9, orientated along ϕ to measure the coordinate in the bending plane of the magnetic field with a resolution of 35 μm .

The MDT subsystem can only handle hit rates below 150 Hz/cm². For this reason, CSCs are used in the innermost end-cap layer where hit rates are larger. CSCs can handle hit rates up to 1000 Hz/cm². CSC are multiwire proportional chambers. These chambers are filled with a Ar-CO₂ gas mixture and evenly spaced wires kept at 1900 V. These wires are orientated in the radial direction but not read out. Instead on one side of the cathode are copper strips parallel to the wires, measuring η , while on the other side of the cathode are strips parallel to the wires measuring ϕ . The width between strips is approximately 1.5 mm providing a resolution of 60 μm in the bending-plane and 5 mm in the non-bending plane.

Since the CSC and MDT systems do not have prompt timing signals, the RPC and TGC systems are used for triggering. The RPC system is used in the barrel region ($|\eta| < 1.05$). RPC consist of two parallel resistive plates separated by a 2 mm insulated spacer with 100 mm spacing kept at 9.8 kV, as shown in Figure 6.10. A gaseous mixture of C₂H₂F₄, C₄H₁₀, and SF₆ fills the space between the two plates. Metallic strips on the outer faces of the plates are used to read out signals produced by the gas ionizing. The middle barrel layer consists of two layers of RPCs on either side of the MDT layer and one layer on the outermost MDT layer. Each layer contains two orthogonal sets of metallic strips providing η and ϕ measurements. The timing resolution of RPCs is 1.5 ns, and therefore may be used to identify bunch crossings.

Finally, the TGCs are used in the end-cap regions and are primarily used to provide L1 trigger decisions and ϕ measurements. TGCs are multi-wire propor-

tional chambers consisting of arrays of gold-coated tungsten wires placed between two cathode planes. These wires are separated by 1.8 mm and cathodes are 1.4 mm from the wires. Orthogonal to the wires, on the opposite side of the cathode plane are copper strips held at 2900 V. The chambers are filled with a mixture of CO₂ and n-pentane gas, the latter acts as a quenching gas to prevent avalanches initiated by secondary γ -rays from the primary avalanche. Figure 6.11 is a schematic of a TGC. The timing resolution of TGCs is less than 25 ns and therefore they are used for bunch crossing measurements.

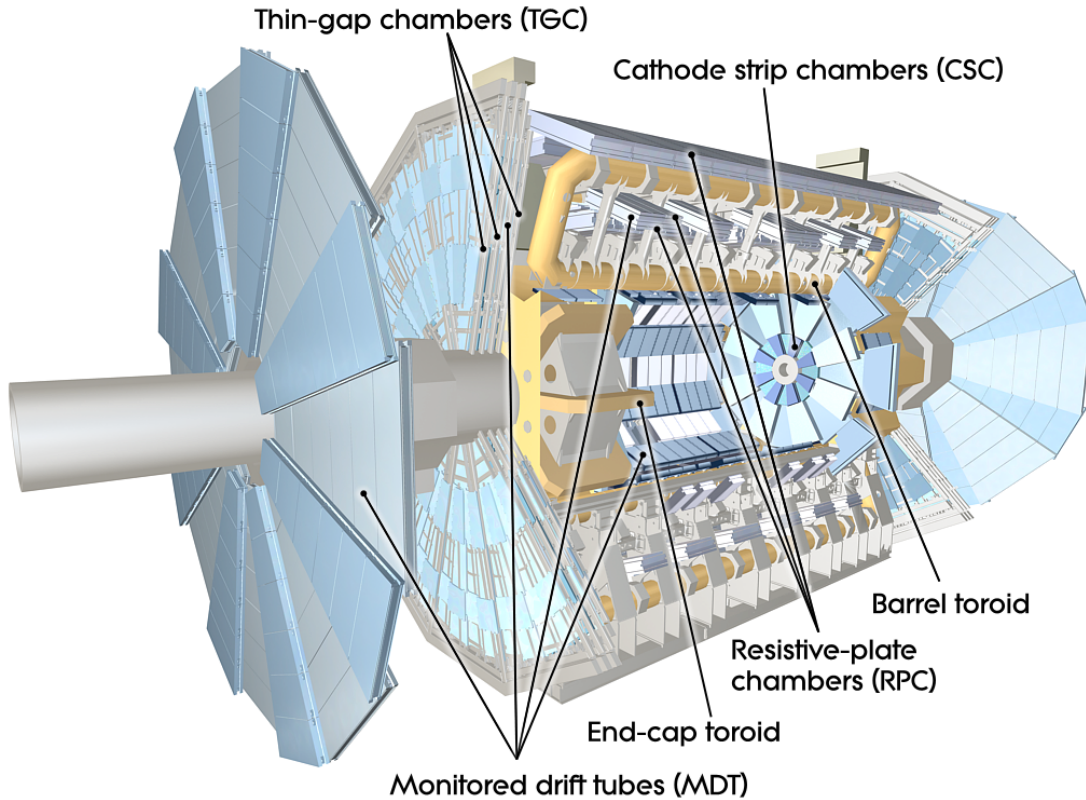


Figure 6.8: Schematic of Muon Spectrometer [16]

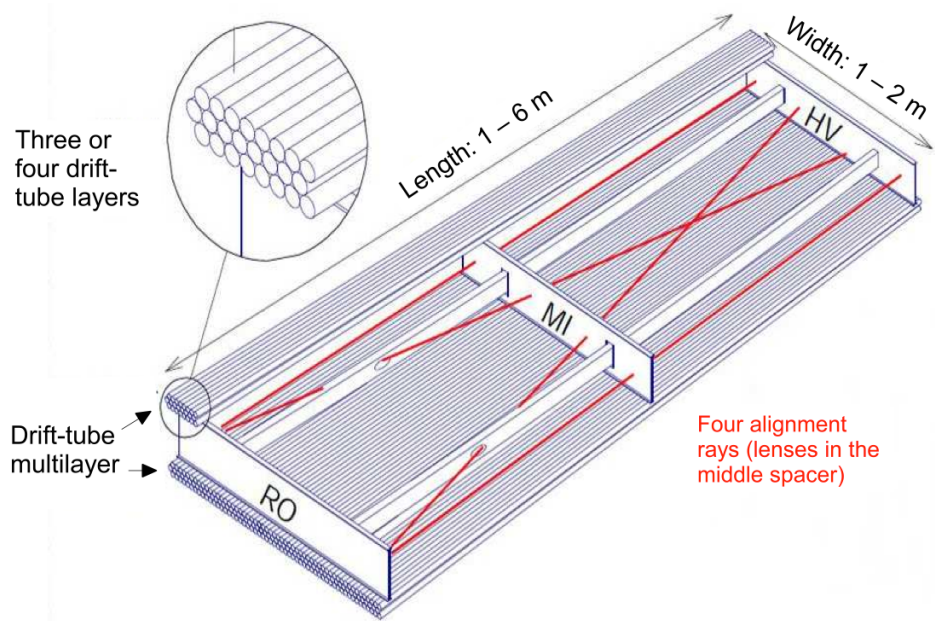


Figure 6.9: Schematic of MDT chamber.

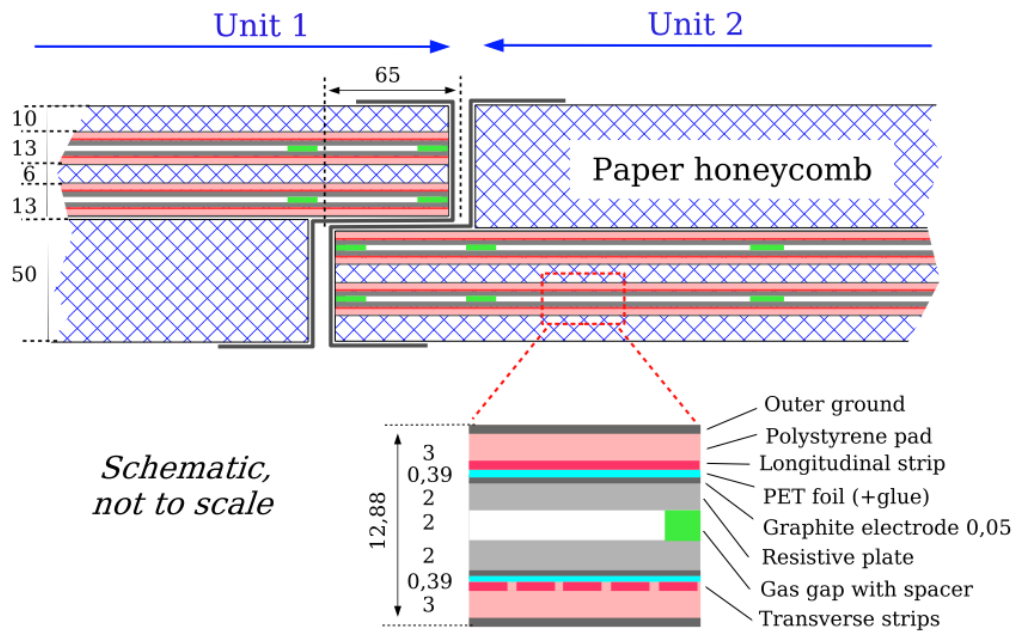


Figure 6.10: Schematic of RPC chamber, which is used for triggering in the central region of the detector.

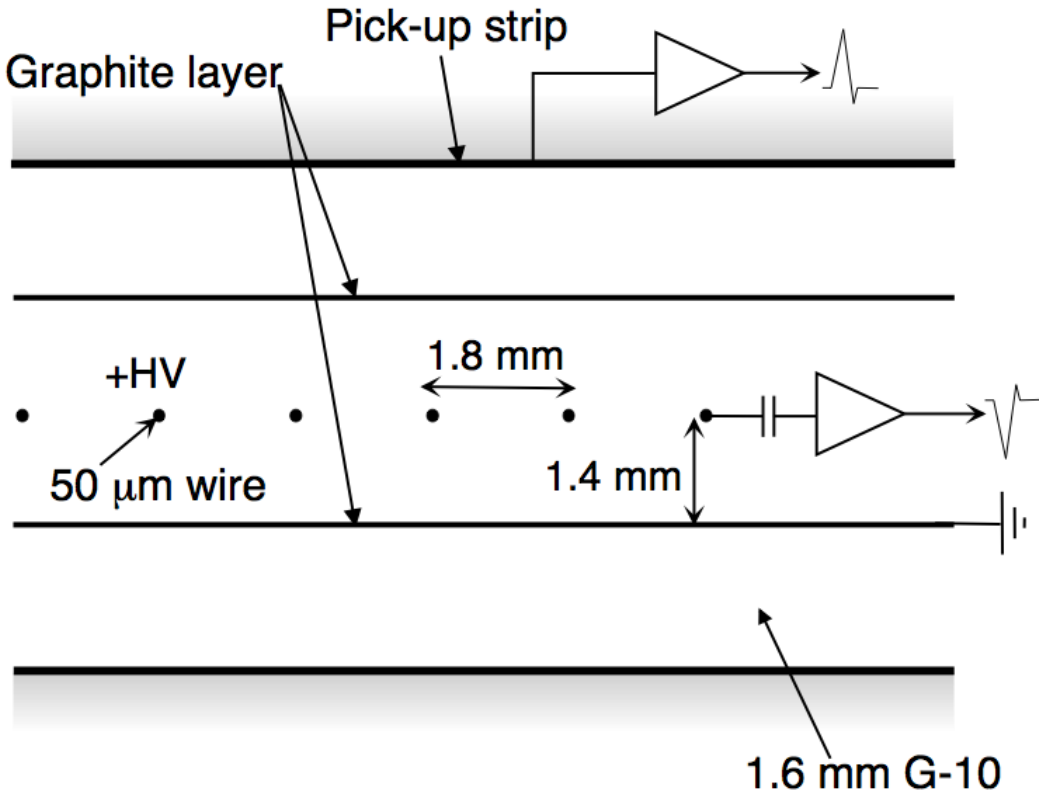


Figure 6.11: Schematic of TGC chamber, which is used for triggering in the muon end-cap region.

6.5 Magnet System

A particle with charge, q and velocity v , moving in magnetic field, B , experiences a force, $F = qv \times B$. This force curves the particle's trajectory, which the ID and MS use to determine the particle's p_T . The central solenoid provides the magnetic field for the ID and the toroidal magnets provide the magnetic field for the MS.

The layout of the magnet system is shown in Figure 6.12. The central solenoid consists of a single-layer Al-stabilized NbTi conductor coil wound inside an Al

support cylinder. The solenoid is 5.8 m long, 50 cm thick and has an inner radius of 1.23 m. It is cooled to 4.5 K to reach superconducting temperatures and shares the liquid argon calorimeter vacuum vessel to minimize material in the detector. A current of 7.730 kA produces a 1.998 T solenoidal magnetic field, pointing in the $+z$ direction.

The toroidal magnet system consists of a barrel and two end-cap toroidal magnets used to create a magnetic field outside the calorimeters that is orientated along ϕ . Each barrel toroid is 25.3 m long with an inner and outer diameter of 9.4 and 20.1 m and weighs 830 tonnes. Endcap toroids are 5 m long with an inner and outer radius of 1.65 and 10.7 m. Both toroid systems use Al-stabilized Nb/Ti/Cu conductors. The magnetic field strength in the barrel and endcap regions are 0.5 and 1 T, respectively.

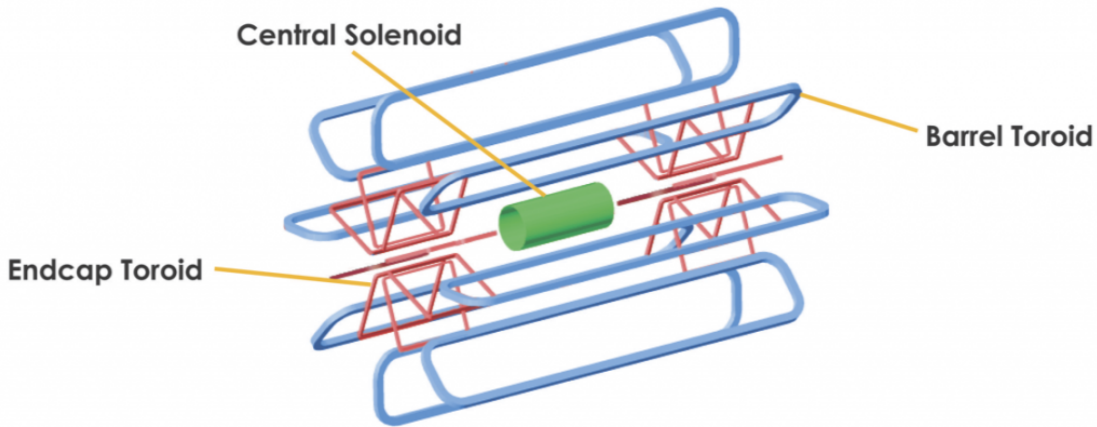


Figure 6.12: Layout of ATLAS magnet systems.

6.6 Trigger System

Since collisions occur every 25 ns and reading out all detector channels and storing that information is not currently feasible (would require saving 60 million MB/s), the majority of events are not kept for analysis. ATLAS uses a multi-stage

trigger system to select approximately 1,000 of the 1.7 billion collisions that occur each second (corresponding to a rate of 1 kHz from the 40 MHz proton collision rate). The first stage of the trigger system is the hardware level (L1) trigger. This trigger reduces the event rate to \sim 100 kHz by identifying Regions-of-Interest (ROIs) containing high p_T leptons, photons, jets, or E_T^{miss} by using information from RPCs, TGCs, and calorimeters to make a $2.5 \mu s$ decision. This information is then passed to a high-level trigger (HLT) which further decreases event rates to ~ 1 kHz. The HLT uses finer granularity measurements from the MS and ID to perform simplified offline reconstruction to decide which are worth saving.

Part IV

The Search for WW and WZ

Resonances in $\ell\nu qq$ final states

Chapter 7

Dataset and Simulated Samples

7.1 Dataset

This analysis uses pp collision data collected from 2015 to 2018 at $\sqrt{s} = 13$ TeV, corresponding to 139/fb of data as shown in Figure 7.1 and 7.2. From this dataset, only those events in which the tracker, calorimeters, and muon spectrometer have good data quality are used. For a given event, the solenoid and toroidal magnets must also be operating at their nominal field strengths. Events with detector subsystem failures (e.g. events with LAr noise bursts, ECAL saturation, TileCal errors, and event recovery issues due to ID failures) are not used. Events with information missing from subsystems (usually from busy detector conditions) are rejected. Events must also contain a primary vertex (PV) with at least two associated tracks, where the PV is the vertex with the largest $\sum p_T^2$ over tracks associated with the vertex with $p_T > 0.5$ GeV.

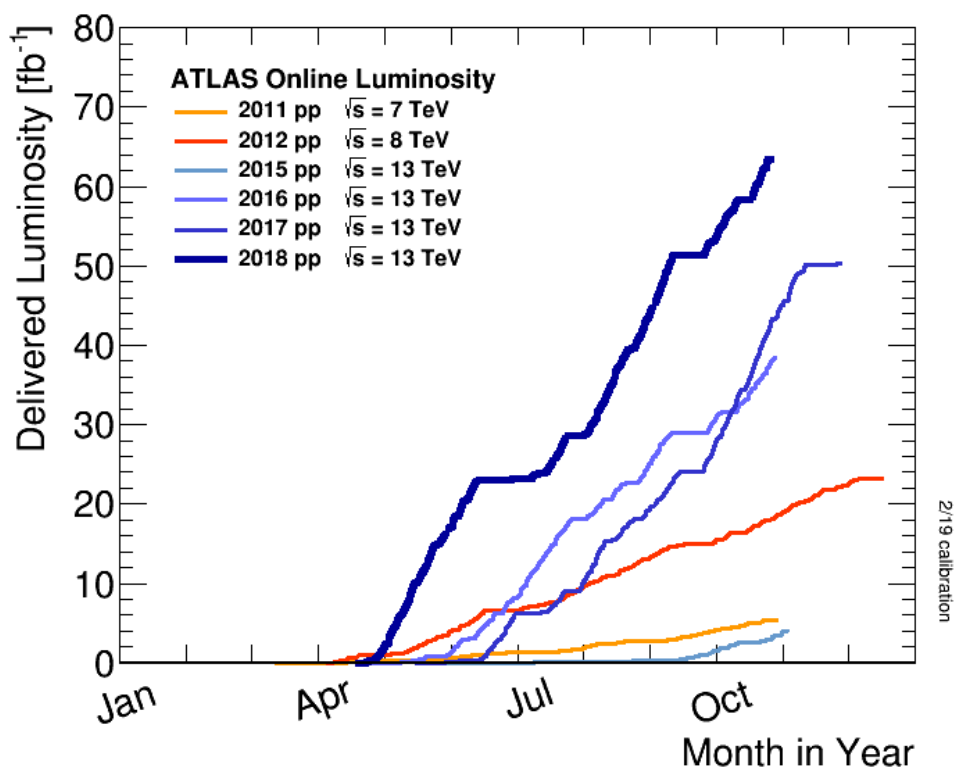


Figure 7.1: Integrated luminosity for data collected from ATLAS from 2011 - 2018



Figure 7.2: Mean number of interactions per crossing for data collected from ATLAS from 2011 - 2018

7.2 Simulated Samples

Samples are simulated in order to model backgrounds, evaluate signal acceptance, optimize event selection and estimate systematic and statistical uncertainties. The dominant backgrounds for this analysis are $W/Z + \text{jets}$, diboson (WZ/WW), $t\bar{t}$, single top and multijet production.

$W/Z+\text{jet}$ events are simulated using Sherpa 2.2.1 at NLO [30] and merged with the Sherpa parton shower using the ME+PS@NLO prescription [31]. These events are then normalized to NNLO cross sections. The $t\bar{t}$ and single-top backgrounds are generated with Powheg-Box with NNPDF3.0NLO PDF sets in the matrix element calculation [10]. For all processes, the parton shower, fragmentation, and underlying event are simulated using Pythia 8.320 with the A14 tune set [10]. Diboson processes are generated using Sherpa 2.2.1.

Signal samples are simulated using MadGraph 5-2.2.2 [9] and Pythia 8.186 with NNPDF230LO. RS Graviton samples are generated with $k/M_{PL}=1$. HVT Model A (B) samples are simulated with $g_V = 1(3)$. To model VBF production of HVT signals, $g_H = 1$ and $g_f = 0$. Signal resonances are generated for masses between 300 GeV and 4 TeV.

Chapter 8

Objects

8.1 Electrons

Electrons are reconstructed from electromagnetic showers in the ECAL. During reconstruction cells of $\Delta\eta \times \Delta\phi = 0.025 \times 0.025$ are grouped into 3×5 clusters. These clusters are then scanned for local maxima that seed electron clusters. These clusters must then be matched to a ID track from the PV. This requirement minimizes non-prompt electron and fake electron backgrounds. Electrons must pass identification and isolation requirements. Electron identification (loose, medium, tight) is based on a multivariate discriminant derived from a likelihood method. For this analysis, events are required to have one tight electron and no additional loose electrons. Electrons are also required to be isolated. The electrons are considered isolated if the quotient of the sum of the transverse momentum (of calorimeter energy deposits) in a cone around the electron of size $\Delta R = 0.2$ and the transverse momentum of the electron to be less than $0.015 * p_T$ or 3.5 GeV, whichever is smaller. This requirement rejects non-prompt photons and fake leptons. Electrons in this analysis are also required to have $p_T > 30$ GeV and $|\eta| < 2.47$.

Electrons are calibrated with data-driven scale factors using $J/\Psi \rightarrow ee$, $Z \rightarrow ee$, $Z \rightarrow \ell\ell\gamma$ processes. These corrections account for the non-uniform response of the detector which introduces modeling and reconstruction uncertainties.

8.2 Muons

As muons traverse the entire detector, they are reconstructed from ID and MS tracks. For this analysis the muon identification and isolation working points are chosen to minimize the contributions from non-prompt muons. Towards this end, each selected event must contain exactly one muon that passes the medium identification working point, and no additional muons (that pass the loose working point). For the medium working point, two types of reconstructed muons are used: combined and extrapolated muons (CB and ME, respectively). For CB muons, ID and MS tracks are reconstructed independently and a combined track fit is performed by adding or removing MS tracks to improve the fit quality. ME muons are reconstructed from only MS tracks with hits in at least two layers, which ensures the track originates from the PV. ME muons extend the acceptance for muon reconstruction outside the ID from $2.5 < |\eta| < 2.7$. The medium identification working point uses CB and ME tracks. CB tracks must have at least 3 hits in two MDT layers. ME tracks are required to have at least three MDT/CSC hits. To further minimize contributions from fake muons, the selected muons are required to be isolated from other tracks, as muons from W, Z decays are often isolated from other particles. To insure the selected muons are isolated, the scalar sum of the transverse momentum of tracks in a cone of $\Delta R = 0.3$ compared to the transverse momentum of the muon must be less than 0.06. Muons are also required to have $p_T > 30$ GeV.

Muons are calibrated using well-studied resonances $J/\Psi \rightarrow \mu\mu$ (for $p_T^\mu < 10$

GeV) and $Z \rightarrow \mu\mu$ (for $p_T^\mu > 10$ GeV). Figure 8.1 shows the combined muon p_T uncertainty from this calibration. The total systematic uncertainty is less than 1% for all p_T ranges considered in this analysis.

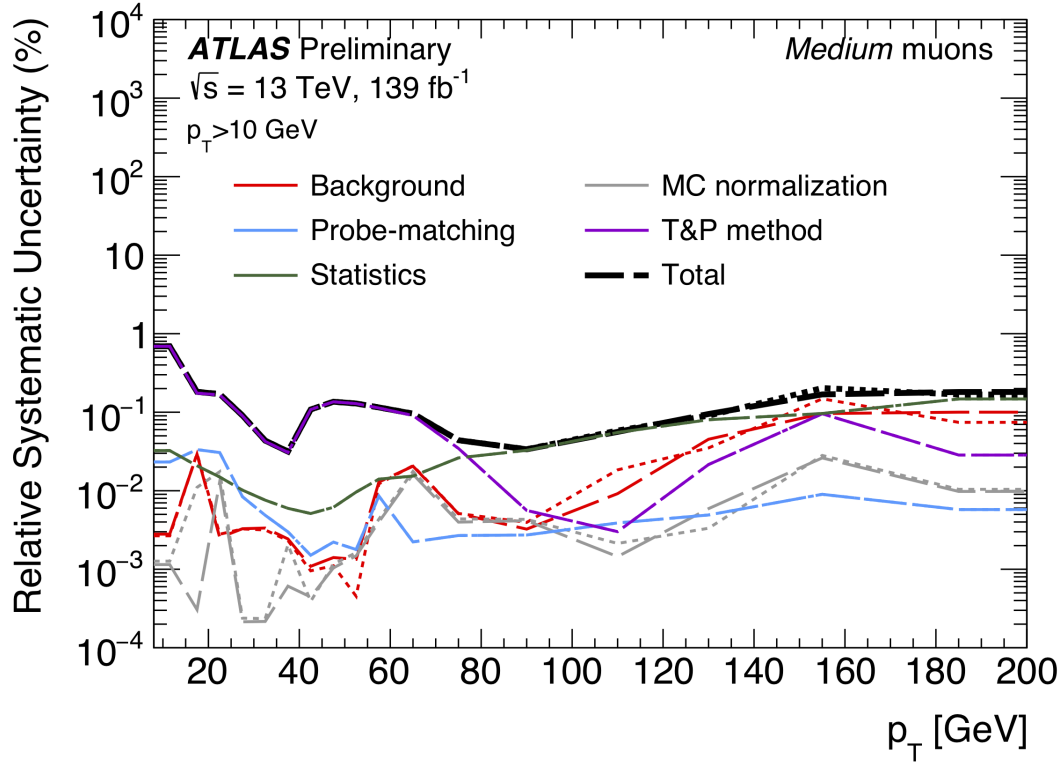


Figure 8.1: This figure shows the breakdown of the muon reconstruction efficiency scale factor measured in $Z \rightarrow \mu\mu$ as a function of the muon p_T [14].

8.3 Jets

Three types of jets are used in this analysis: variable radius, small-R and large-R jets. Variable radius jets are used to reconstruct Z bosons decaying to two b -jets in the jet catchment area of large-R jet in the merged regime. Small-R jets are used to reconstruct the hadronically decaying W/Z candidates in the resolved analysis and the forward jets from resonances produced through vector

boson fusion. Large-R jets are used to reconstruct the hadronically decaying boson in the merged regime.

For these jet collections, the jet energy is calibrated sequentially as shown in Figure 8.2. After the jet direction is corrected to point to the PV, the energy of the jet is corrected. First, the jet energy is corrected to account for pileup contributions based on the p_T and area of the jet (these corrections are extracted from a $pp \rightarrow jj$ sample). Following this, another pileup correction is applied that scales with μ and N_{PV} .

MC-based corrections are then applied that are meant to transform the jet energy and η back to particle level as detailed in [19]. These corrections account for the non-compensating nature of the ATLAS calorimeters and detector inhomogeneities. Following this, the Global Sequential Calibration is applied that reduces the flavor dependence of jet calibrations and accounts for energy leakage of jets outside the calorimeters. Finally, in-situ corrections are applied that account for differences in jet response between data and simulation ($\gamma/Z+jet$ and fake lepton samples are used). These differences can arise from mismodeling the hard scattering process, pile-up, and jet formation.

To further reject jets not arising from the hadronically decaying boson, jets must pass quality requirements based on the following variables [3]:

- f_Q^{LAr} : fraction of energy of jet's LAr cells with poor signal shape
- f_Q^{HEC} : fraction of energy of jet's HEC cells with poor signal shape
- E_{neg} : sum of cells with negative energy
- f_{EM} : fraction of jet's energy deposited in EM calorimeter
- f_{HEC} : fraction of jet's energy deposited in HEC calorimeter

- f_{max} : maximum energy fraction in any single calorimeter layer
- f_{ch} : ratio of the scalar sum of the p_T of a jet's charged tracks to the jet's p_T

Jets selected for the resolved analysis must pass one of the following criteria, to maximize jet efficiency:

- $f_{HEC} > 0.5$ and $|f_Q^{HEC}| > 0.5$ and $\langle Q \rangle > 0.8$, which minimizes jets formed from sporadic noise bursts in the HCAL endcap.
- $|E_{neg}| > 60$ GeV, which minimizes jets formed from sporadic noise bursts in the HCAL endcap.
- $f_{EM} > 0.95$ and $f_Q^{LAr} > 0.8$ and $\langle Q \rangle > 0.8$ and $|\eta| < 2.8$, which minimizes jets formed from coherent noise or isolated pathological ECAL cells.
- $f_{max} > 0.99$ and $|\eta| < 2$, which minimizes jets mistakenly formed due to hardware issues, beam-induced backgrounds, and cosmic muon showers.
- $f_{EM} < 0.05$ and $f_{ch} < 0.05$ and $|\eta| < 2$, which minimizes jets mistakenly formed due to hardware issues, beam-induced backgrounds, and cosmic muon showers.
- $f_{EM} < 0.05$ and $|\eta| > 2$, which minimizes jets mistakenly formed due to hardware issues, beam-induced backgrounds, and cosmic muon showers.

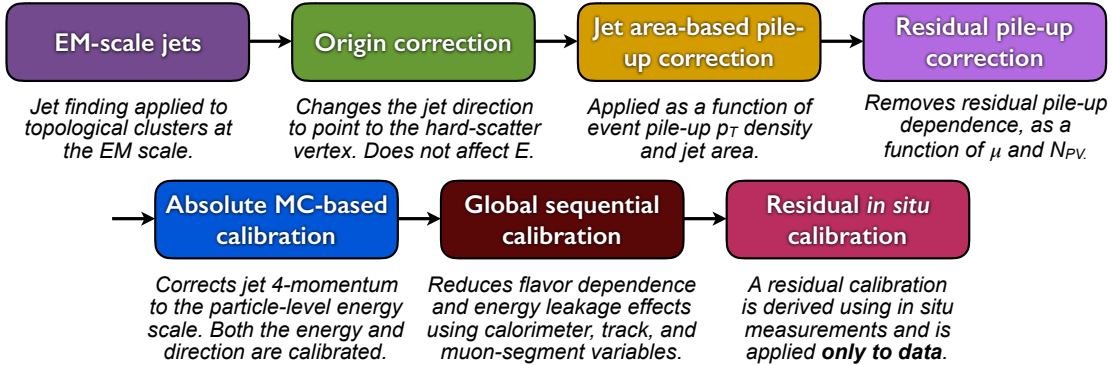


Figure 8.2: This diagram shows the calibration stages for EM jets [21].

8.3.1 Small-R jets

Small-R jets are used to reconstruct the hadronically decaying W/Z candidate when the two resulting jets are well-separated in $\eta\phi$. Small-R jets are also used to identify forward jets from resonances produced through vector boson fusion. Small-R jets are constructed from topologically connected clusters of calorimeter cells (topoclusters), seeded from calorimeter cells with energy deposits significantly above the noise threshold. These cells are then used as inputs to the $anti-k_t$ algorithm [38] with a radius parameter, $R = 0.4$, implemented in the FastJet package [12].

Small-R jets used in this analysis must have $p_T > 30$ GeV and $|\eta| < 2.5$. To further reduce jets not from the hadronically decaying boson, the jet-vertex-tagger (JVT) is used [17]. The JVT uses two track-based variables, corrJVF and R_{p_T} to calculate the likelihood that the jet originated from the PV. The corrJVF variable compares the scalar sum of the p_T of tracks associated with the jet and PV to the scalar sum of the p_T of tracks associated with the jet. This variable also includes a correction that reduces the dependency of corrJVF on the number of reconstructed vertices in the event. The other discriminant, R_{p_T} , is the ratio of the scalar sum of the p_T of tracks associated with the jet and PV and the jet

p_T . Both of these variables peak around zero for pileup jets, as these jets are unlikely to have tracks associated with the PV. JVT cuts are applied to all jets with $p_T > 120$ GeV. Central jets ($|\eta| < 2.4$) are required to have a $\text{JVT} > 0.59$ and forward jets ($2.4 < |\eta| < 2.5$) are required to have $\text{JVT} > 0.11$.

8.3.2 Large-R jets

Large-R ($R = 1.0$) jets are used to reconstruct the hadronically decaying W/Z candidate when the resulting jets are not well-separated in $\eta\text{-}\phi$ space, and overlap forming one large-R jet. Track-Calorimeter Clusters (TCCs) are used to reconstruct these jets [5]. These jets are constructed using a pseudo particle flow method using ID tracks matched to calorimeter clusters [25]. To remove contamination in the jet from pileup and the underlying event, jets are trimmed using a re-clustering algorithm. This algorithm removes subjets with $p_T^{\text{subjett}} < 0.1 p_T^{\text{jet}}$.

The angular resolution of the calorimeter degrades sharply with jet p_T , but the jet energy resolution improves. The tracker has excellent angular resolution which improves with p_T . Therefore, by matching tracks to jets, TCCs have more precise energy and angular resolution than jets constructed from only calorimeter clusters. These jets are required to have $p_T > 200$ GeV, $|\eta| < 2.0$ and $m_J > 50$ GeV.

TCC jets are trimmed as detailed in [35], which suppresses pileup and soft radiation in the jet, the jet mass is calculated as the four-vector sum of the jet's constituents (assuming massless constituents). The jet mass peaks around the W/Z boson mass for $W/Z \rightarrow qq$ jets, and more broadly for single-quark and single-gluon induced jets.

These jets are tagged as W jet if the jet passes optimized jet mass and substructure (D_2) cuts for W bosons, and a Z jet if it passes the cuts for the Z boson.

The jet substructure variable D_2 is a ratio of energy correlation functions. These functions are derived from the energies and pair-wise angles of jet constituents ([36], [37]):

$$D_2^{\beta=1} = E_{CF3} \left(\frac{E_{CF1}}{E_{CF2}} \right)^3 \quad (8.1)$$

where the energy correlation functions are defined as:

$$E_{CF1} = \sum_i p_{T,i} \quad (8.2)$$

$$E_{CF2} = \sum_{ij} p_{T,i} p_{T,j} \Delta R_{ij} \quad (8.3)$$

$$E_{CF3} = \sum_{ijk} p_{T,i} p_{T,j} p_{T,k} \Delta R_{ij} \Delta R_{jk} \Delta R_{ki} \quad (8.4)$$

A two-dimensional optimization of the jet mass and D_2 thresholds was performed to provide maximum sensitivity for this analysis. This optimization was done by maximizing the signal sensitivity (using HVT W' and G_{KK} samples) against the single quark and gluon jet backgrounds in jet p_T bins. Figure 8.3 shows the optimized thresholds on D_2 and jet mass as a function of p_T . Figure 8.4 shows the efficiency of the optimized W/Z taggers as a function of jet p_T .

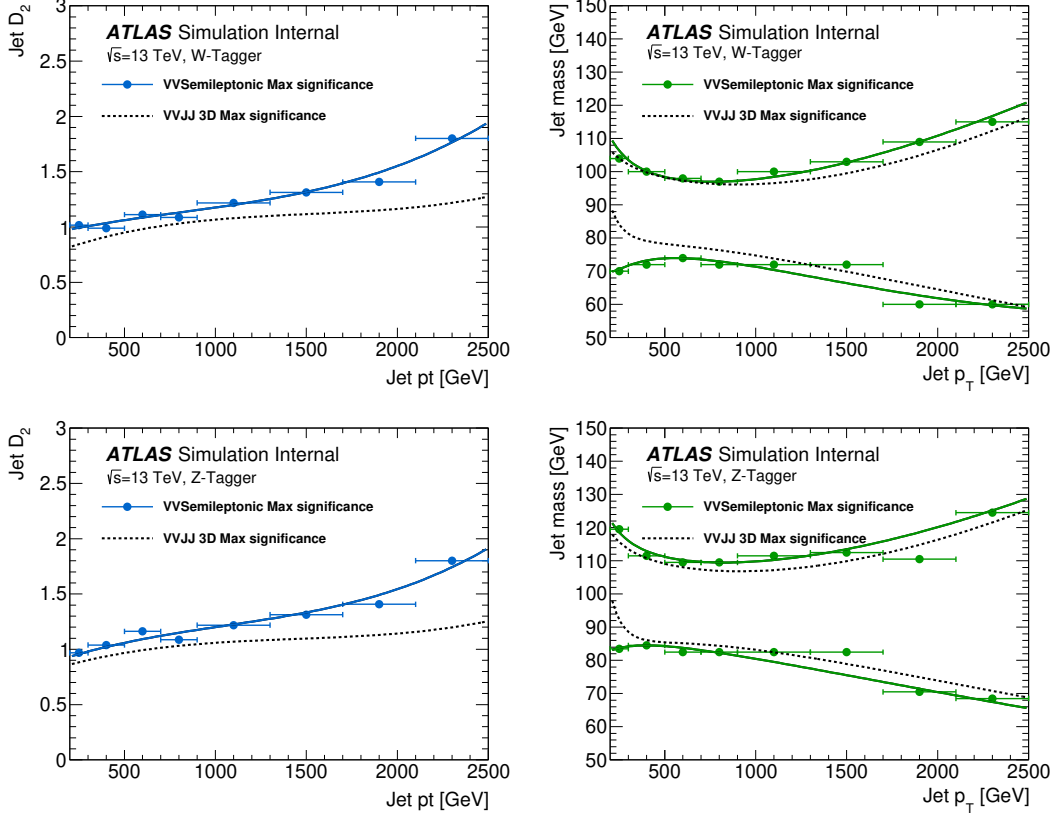


Figure 8.3: The upper cut on D_2 (a) and jet mass window cut i.e. the upper and lower boundary of the mass (b) of the W -tagger as a function of jet p_T . Corresponding values for Z -tagger are shown in (c) and (d). The optimal cut values for maximum significance are shown as solid markers and the fitted function as solid lines. Working points from $VV \rightarrow JJ$ [20] is also shown as dashed lines as a reference.

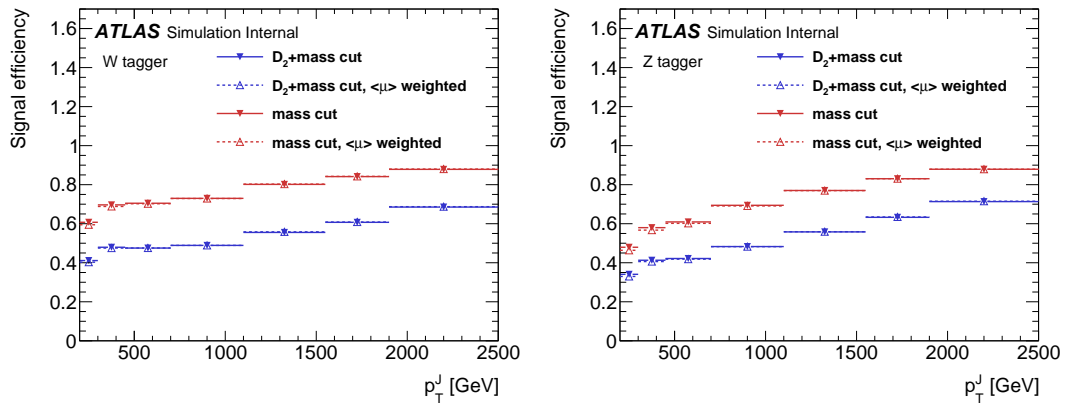


Figure 8.4: The left (right) plot shows the efficiency for the $W(Z)$ tagger mass and D_2 cuts as a function of large-R jet p_T .

8.3.3 Variable Radius jets

To accept more boosted Z bosons decaying to $b\bar{b}$ that would normally be rejected due to topological cuts discussed 9.4, variable radius (VR) track jets are used to identify b -jets (discussed in 8.3.4) within the catchment area of large-R jets [34]. VR jets are constructed from ID tracks using the anti- k_t algorithm with a radius parameter that depends on the p_T of the track, shown in Equation 8.5.

$$R_{eff}(p_{T,i}) = \frac{\rho}{p_{T,i}} \quad (8.5)$$

For this search $\rho = 30$ GeV and a lower and upper limit on cone size are set to 0.02 and 0.4, respectively, to prevent unphysical asymptotic behavior of ρ . Collinear VR jets are possible, so track jets that are not separated by the the smaller jet's cone size are not used. Additionally, VR jets are required to have $p_T > 10$ GeV and $|\eta| < 2.5$.

8.3.4 Jet Flavor Tagging

To more precisely identify jets, the small-R and VR jets originating from a b -quarks are classified using a multivariate b -tagging algorithm (BDT), MV2c10 [4]. This algorithm uses the impact parameters of the jet's ID tracks, secondary vertices (if they exist), and reconstructed flight paths of b and c hadrons in the jet to determine if the jet was induced by a b -quark. For this analysis, the 85% efficient working point of this algorithm is used giving c , τ , and light-flavor jet rejection of 3, 8, and 34 respectively in simulated $t\bar{t}$ samples.

8.4 MET/Neutrinos

Neutrinos are uncharged and colorless particles, so they do not leave tracks or jets in the detector. For this reason, neutrinos are reconstructed as the missing energy in the event, E_T^{miss} . Mathematically, E_T^{miss} is the negative vector p_T sum of all the physics objects and an extra soft term. The soft term accounts for energy deposits not associated with any of the objects in the event. In this analysis, the soft term is the p_T sum of all ID tracks not associated with objects in the event. The selected tracks must be matched to the PV, which decreases pile-up contamination [2].

8.5 Overlap Removal

Reconstructed jets and leptons in this analysis can arise from the same energy deposits. For instance, a cluster of energy from an electron can also be a valid calorimeter seed for a jet. To mitigate this confusion of multiple objects originating from a single jet or lepton overlapping objects are removed via a procedure referred to a overlap removal.

The overlap selections used in this analysis are described below.

- when an electron shares a track with another electron: the lower p_T electron is rejected, as it is more likely to be a fake electron
- when a muon and electron share a track: the muon is rejected if it is a calo-muon, otherwise the electron is rejected
- when $\Delta R < 0.2$ for an electron and jet: the jet is rejected to maximize signal acceptance

- when $\Delta R > 0.2$ for an electron and jet: the electron is rejected as it likely originated from decays within the jet
- when $\Delta R < \min(0.4, 0.04 + 10\text{GeV}/p_T^\mu)$ for a muon and jet: the muon is rejected, again maximizing signal acceptance, otherwise the jet is rejected
- when $\Delta R < 1.0$ for the a large-R jet and electron: the jet is rejected

8.6 Reconstructed Resonance Mass (m_{WV})

The WV system mass, m_{WV} , is reconstructed from the lepton, neutrino, and hadronically-decaying boson candidate. The momentum of the neutrino along the z -direction is obtained by constraining the W boson mass of the lepton neutrino system to be $80.3 \text{ GeV}/c^2$. For complex solutions to this constraint, p_Z is taken as the real component of the solution. For real solutions, the one with the smaller absolute value is used. For the resolved analysis, m_{WV} is reconstructed by constraining the $W(Z)$ dijet system in the SRs and TCRs (not the WCRs):

$$p_{T,jj}^{corr} = p_{T,jj} \times \frac{m_{W/Z}}{m_{jj}} \quad (8.6)$$

$$m_{jj}^{corr} = m_{W/Z} \quad (8.7)$$

where m_{jj} and $m_{W/Z}$ are the reconstructed invariant mass of the hadronically-decaying W/Z boson and the PDG values of the W/Z boson masses, respectively. This correction improves the m_{WV} mass distribution by $\sim 10\%$.

The reconstructed resonance mass is the final discriminating variable in this analysis. The distribution of this variable in SRs is used in the final likelihood fit to search for evidence of an excess of events due to BSM resonances. Distributions of m_{WV} are shown in Figures 13.1-13.7.

Chapter 9

Event Selection and Categorization

To effectively search for these new resonances, the simulated background and signal samples are analyzed to determine a series of optimized cuts used to create SRs containing leptonic and hadronic resonance decay products. In these regions, the resonance mass is calculated as the combined system mass of the leptonic and hadronic systems as described in 8.6. The expected resonance mass distribution from the backgrounds and signal samples are compared to data to search for the existence of these BSM signals (also known as a bump hunt). Control regions enriched in the dominant backgrounds, $t\bar{t}$ and $W+\text{jets}$ (TCR and WCR, respectively) are constructed to be orthogonal to SRs and used to determine the normalization of the $t\bar{t}$ and $W+\text{jets}$ backgrounds in SRs.

Events are classified as produced via non-VBF or VBF processes using a Recursive Neural Network (RNN) described in 9.3. VBF W' and Z' and ggF W' and Z' resonances studied have unique SR and CR selections to maximize analysis sensitivity. RS Graviton signals are probed using the same selections as the ggF Z' signal.

The more massive the resonance, the more likely W/Z bosons are to be boosted in this search. As the boost of the hadronically decaying boson increases the separation of its hadronic decay products decreases. When the hadronically decaying boson has sufficient boost, the two quarks will overlap and not be identified separately. For this reason, a set of resolved selections are used when the hadronic decay products are reconstructed separately, and merged selections when the decay products overlap and identified as a single merged jet in the event. A W/Z tagger identifies merged jets as originating from a W/Z bosons based on jet substructure and mass cuts. However, the more boosted the jet is the less likely it is to pass the jet substructure cut, due to track merging. Consequently, the merged analysis uses a high purity region (HP), which requires that the jet pass both cuts, and low purity (LP) region where the jet can fail the jet substructure cut. These selections are summarized in 9.4.

The aforementioned SR definitions veto events with b -jets to minimize $t\bar{t}$ contamination. However, b -jets are anticipated from W' resonances from the hadronically decaying Z boson. To increase the signal acceptance of these resonances, a $Z \rightarrow bb$ tagger is used to construct additional SR and CRs called the "tagged" regions (and "untagged" if the event fails the $Z \rightarrow bb$ tagger).

9.1 Pre-selection

Before applying topological cuts, preselection cuts are applied which include trigger and event requirements to reduce background contamination and the dataset size. Events must contain exactly one tight lepton (no additional loose leptons), the $p_T^{\ell\nu} > 75$ GeV, and there must be at least two small-R jets or one large-R jet.

9.2 Trigger

The data were collected using the lowest unprescaled single-lepton or E_T^{miss} triggers, as summarized in Table 9.1. Since the muon term is not considered in the trigger E_T^{miss} calculation, the E_T^{miss} trigger is fully efficient to events with high- p_T muons. For this reason, the E_T^{miss} trigger is used for events where $p_T^\mu > 150 \text{ GeV}$, to compensate for the poor efficiency of the single muon trigger above $p_T^\mu > 150 \text{ GeV}$.

Table 9.1: The list of triggers used in the analysis.

Data-taking period	$e\nu qq$ channel	$\mu\nu qq$ ($p_T(\mu\nu) < 150$ GeV) channel	$\mu\nu qq$ ($p_T(\mu\nu) > 150$ GeV) channel
2015	HLT_e24_lhmedium_L1EM20 OR HLT_e60_lhmedium OR HLT_e120_lhloose	HLT_mu20_iloose_L1MU15 OR HLT_mu50	HLT_xe70
2016a (run < 302919) $(L < 1.0 \times 10^{34} \text{ cm}^{-2} \text{ s}^{-1})$	HLT_e26_lhtight_nod0_ivarloose OR HLT_e60_lhmedium_nod0 OR HLT_e140_lhloose_nod0 HLT_e300_etcut	HLT_mu26_ivarmedium OR HLT_mu50	HLT_xe90_mht_L1XE50
2016b (run ≥ 302919) $(L < 1.7 \times 10^{34} \text{ cm}^{-2} \text{ s}^{-1})$	same as above	same as above	HLT_xe110_mht_L1XE50
2017	same as above	same as above	HLT_xe110_pufit_L1XE55
2018	same as above	same as above	HLT_xe110_pufit_xe70_L1XE50

9.3 non-VBF/VBF RNN

To classify events as originating from non-VBF or VBF processes a RNN is used [47]. This approach is more powerful than a cut-based classification as it improves analysis sensitivity by exploiting correlations between variables that the RNN learns. In particular, a RNN architecture is ideal as it can handle variable numbers of jets in the events.

The RNN uses the four-momentum of candidate VBF jets to classify events as VBF or non-VBF topologies. Sometimes jets are incorrectly reconstructed, so the number of jets in the event is expected to vary across the input samples. VBF candidate jets are identified by removing jets from the event that are likely from $W/Z \rightarrow qq$. For the resolved regime this means removing the two leading small-R jets from the VBF candidate jet list. For the merged regime this means removing small-R jets separated by less than $\Delta R = 1.0$ from the large-R jet. VBF candidate jets are also required to be within $|\eta| < 4.5$. From the list of remaining VBF candidate jets, the two highest- p_T jets are chosen.

The architecture of the RNN is shown in Figure 9.1. The RNN is composed of Long Short Term Memory Cells (LSTM) that extract meaningful information and retain it. The logic embedded in the LSTM is shown in Figure 9.2. LSTMs are useful for VBF event classification for events with two jets, where using the kinematic properties of both jets (and their correlations) will lead to more efficient event classification.

In this RNN architecture, the VBF candidates are first passed to a masking layer which checks the number of jets in the event. If there is only one jet, only one vertical LSTM layer is used. The output of masking is then passed to a LSTM, with a tanh activation function. The output of the LSTM is then passed to a second horizontal LSTM layer (and vertical LSTM layer if there are two jets in

the event). Finally the output of the last LSTM cell is passed to a dense layer and then to a sigmoid activation layer, leading to an overall RNN score.

The weights and other parameters of the network are learned by training the network with HVT VBF and non-VBF signals and all simulated backgrounds over 200 epochs with an Adam Optimizer [32]. To prevent overfitting during training, dropout is applied to RNN weights and training is truncated if the network parameters are unchanged after ten iterations [49]. Figure 9.4 shows the ROC curve for the RNN using k-fold cross validation [43].

Figure 9.3 shows the RNN discriminant for backgrounds, non-VBF signals, and VBF signals. The RNN score is ~ 0 for non-VBF signals and background processes and ~ 1 for VBF processes. Figure 9.5 shows the limits for various signal processes based on the RNN cut applied. Requiring the RNN score to be > 0.8 was chosen as it provided the best analysis significance for this final state and the $\nu\nu qq$ and $\ell\ell qq$ channels, which this channel will be combined with for future publications.

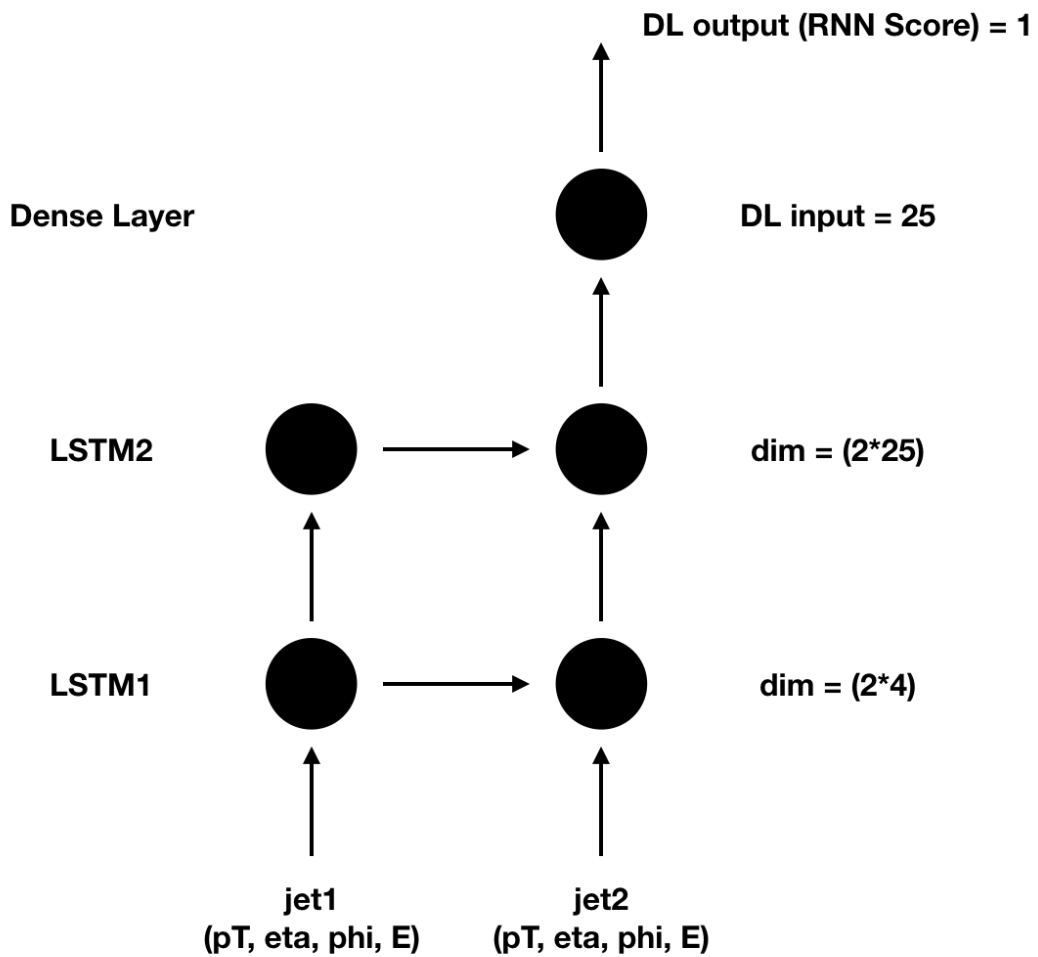


Figure 9.1: This figure shows the architecture of the RNN used to classify events as non-VBF/VBF. The two VBF candidate jet's variable are passed to a through two layers of LSTMs. The vector output of the final LSTM is combined to give the scalar output of the RNN used to classify the event as non-VBF/VBF.

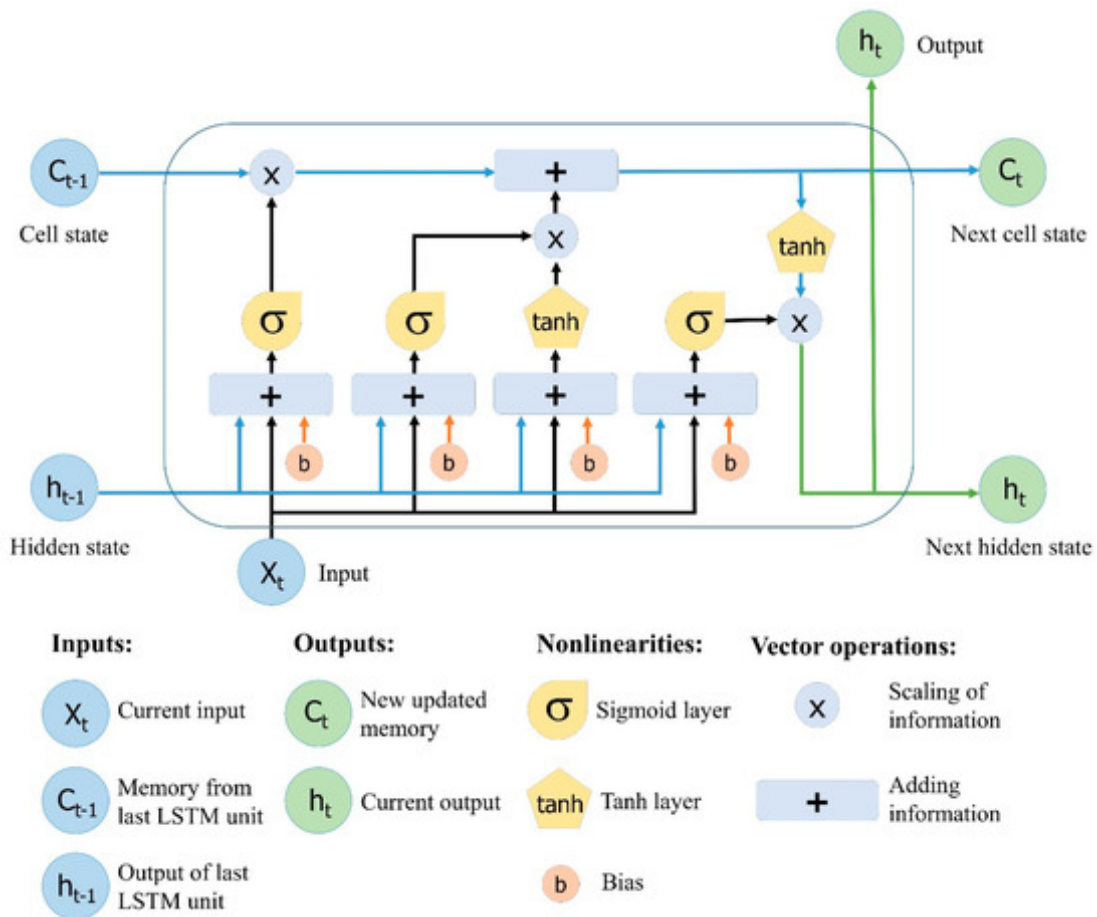


Figure 9.2: This figure shows the embedded logic in LSTM cells. This image was taken from [48], where a more in depth discussion about LSTMs may be found.

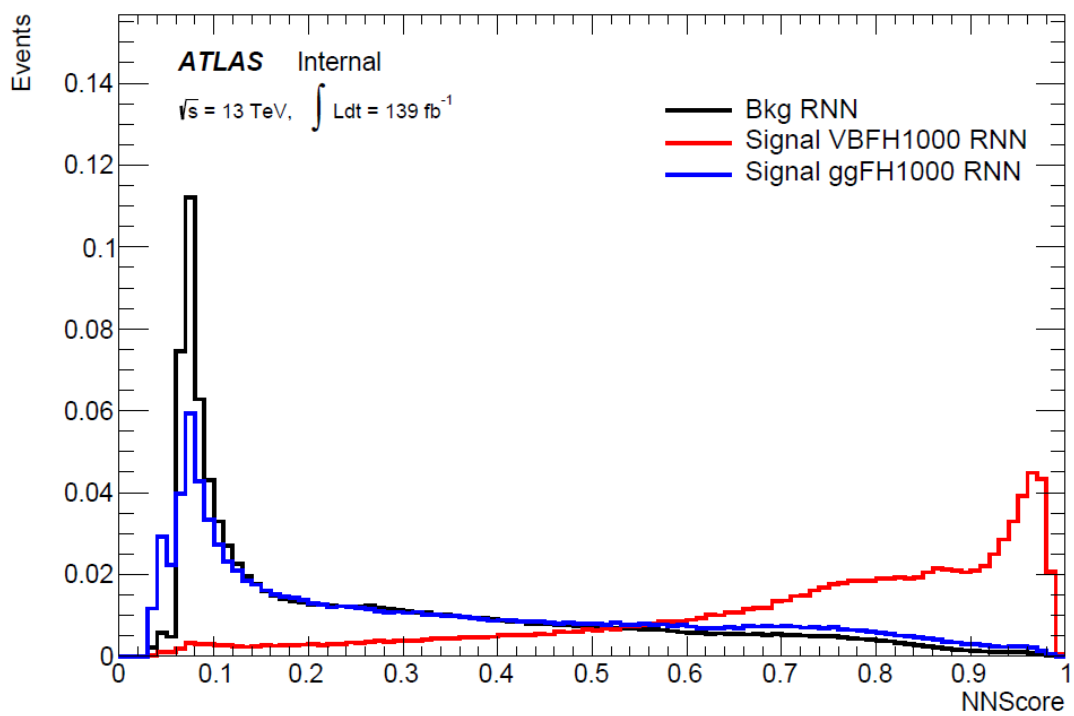


Figure 9.3: RNN Score distribution for ggF and VBF signals and backgrounds.

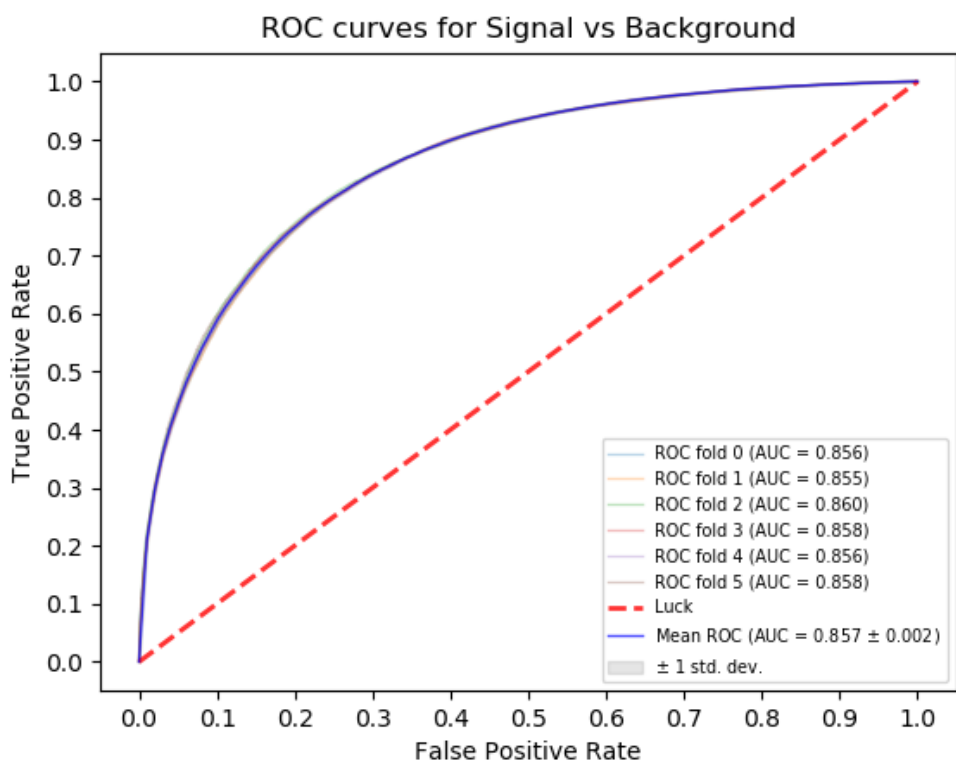


Figure 9.4: ROC curve using k-fold validation for RNN.

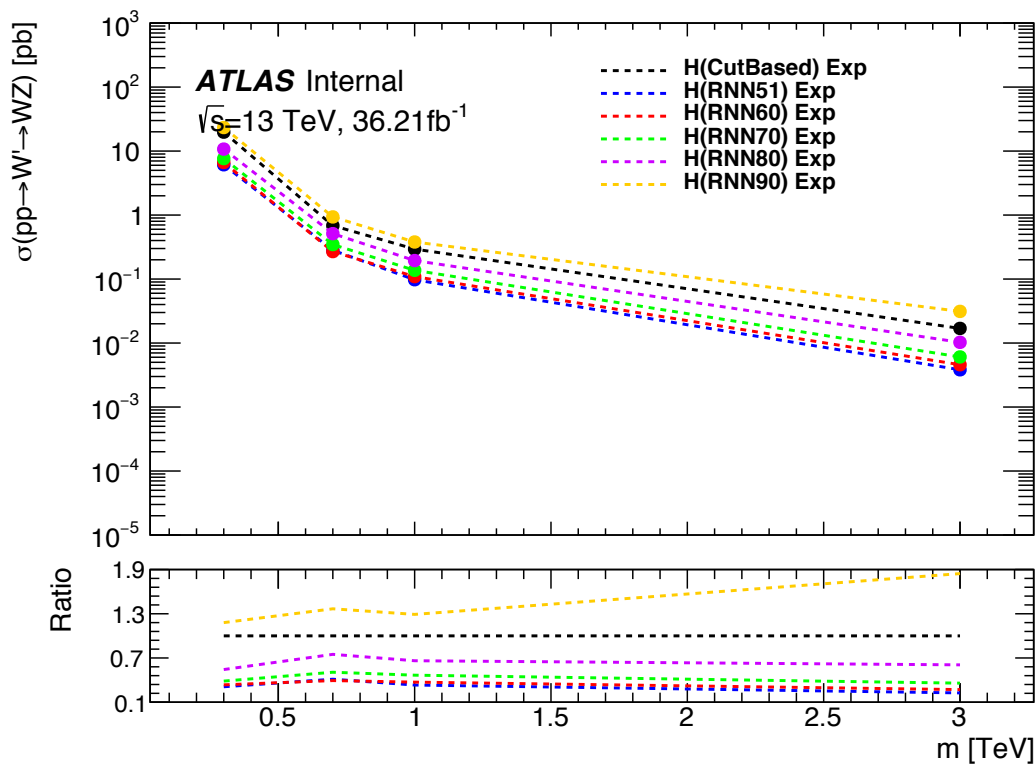


Figure 9.5: Comparison of ggF Z' limits for different RNN score selections. The bottom panel shows the ratio of the upper limits set for different RNN cuts to the cut-based analysis. In this panel smaller numbers, indicate that the expected upper limit is smaller than the cut-based analysis, which is desired.

9.4 Signal Region Definitions

Signal regions are constructed to be dominated by signal and used in the final likelihood fit to look for a bump in the reconstructed resonance mass distribution. Once an event is classified by the RNN, it must pass topological cuts that maximize S/\sqrt{B} . To efficiently select events with a $W \rightarrow \ell\nu$ candidate exactly one tight lepton is required and $E_T^{miss} > 100(60)$ GeV and $p_{T,\ell\nu} > 200(75)$ GeV in the merged (resolved) analysis to suppress the fake lepton backgrounds.

The resonances this search probes are expected to be produced approximately at rest with the two resulting bosons produced back-to-back. For this reason, it is required that the minimum value of $(p_{T,\ell\nu}, p_{T,J})/m_{WV} > 0.35(0.25)$ for the non-VBF (VBF) category.

To reduce $t\bar{t}$ contamination in the merged HVT Z' and G_{KK} analyses, events with at least one b -jet with $\Delta R > 1.0$ from the large-R jet are excluded. High purity signal regions require the D_2 and W/Z mass window cut to be passed, whereas the low purity region only requires the W/Z mass window cut to be passed. More boosted jets, are more likely to fail the D_2 cut due to track merging. Therefore, by using high and low purity regions, the signal acceptance is increased.

The HVT W' resonance search uses tagged and untagged regions to minimize backgrounds and increase signal acceptance. For events to be classified as tagged the large-R jet must contain exactly two b -tagged VR jets. Untagged events must have no more than one b -tagged jet matched to the large-R jet. These selections are shown in Table 9.2.

Events failing the merged selection are then re-analyzed in the resolved category. To enhance resolved signals, the event should contain one leptonic and one hadronic boson candidate that are back-to-back in ϕ as shown by the selections in Table 9.3. Again, to suppress the $t\bar{t}$ backgrounds, events are required to have no

Table 9.2: Summary of selection criteria used to define the signal region (SR), W +jets control region (W CR) and $t\bar{t}$ control region ($t\bar{t}$ CR) for merged 1-lepton channel.

Selection		SR		W CR (WR)		$t\bar{t}$ CR (TR1)	
		HP	LP	HP	LP	HP	LP
$W \rightarrow \ell\nu$	Num of Tight leptons	1					
	Num of Loose leptons	0					
	E_T^{miss}	$> 100 \text{ GeV}$					
	$p_T(\ell\nu)$	$> 200 \text{ GeV}$					
$W/Z \rightarrow J$	Num of large- R jets	≥ 1					
	D_2 cut	pass	fail	pass	fail	pass	fail
	W/Z mass window cut	pass	pass	fail	fail	pass	pass
	Numb. of associated VR track jets b -tagged	For $Z \rightarrow J$: ≤ 1 ($= 2$) for untagged (tagged) category					
	$\min(p_{T,\ell\nu}, p_{T,J}) / m_{WV}$	$> 0.35(0.25)$ for DY/ggF (VBF) category					
	Top-quark veto	Num of b -tagged jets outside of large- R jet	0			≥ 1	
Pass VBF selection			no (yes) for DY/ggF (VBF) category				

additional b -jets for the HVT Z' and G_{KK} analyses. A summary of the resolved selections is shown in Table 9.3.

The analysis cutflow in Figure 9.6 shows how the different categories are prioritized. Events classified as VBF events are classified as merged high purity, merged low purity or resolved signal region selections sequentially. If the event does not pass any of these selections but passes a VBF control region selection it is classified as a VBF CR event.

If the event fails all VBF categories, it is then checked if it passes the merged high purity, merged low purity or resolved signal region selections (NB: for the WZ decay modes all the regions have tagged and untagged categories). If the event fails all of the non-VBF signal region selections, it is then kept for non-VBF control region selections, if it passes those selections. Control region selection are discussed more in 10.1.

Overall, for the DY HVT Z' and ggF G_{KK} signals there are 3 signal regions. For the DY HVT W' signal there are 6 signal regions. For VBF HVT W' and Z' signals there are 3 signal regions.

Table 9.3: The list of selection cuts in the resolved analysis for the WW and WZ signal regions (SR), $W+jets$ control region (WR) and $t\bar{t}$ control region (TR).

cuts	SR	W CR (WR)	$t\bar{t}$ CR (TR1)		
$W \rightarrow \ell\nu$	Number of Tight leptons	1			
	Number of Loose leptons	0			
	E_T^{miss}	> 60 GeV			
	$\cancel{p}_T(\ell\nu)$	> 75 GeV			
$W/Z \rightarrow jj$	Number of small-R jets	≥ 2			
	Leading jet p_T	> 60 GeV			
	Subleading jet p_T	> 45 GeV			
	$Z \rightarrow q\bar{q}$	$78 < m_{jj} < 105$ GeV	$50 < m_{jj} < 68$ GeV or $68 < m_{jj} < 98$ GeV	$105 < m_{jj} < 150$ GeV	$50 < m_{jj} < 150$ GeV
	Num. of b -tagged jets	For $Z \rightarrow jj$: ≤ 1 ($= 2$) for untagged (tagged) category			
Topology cuts	$\Delta\phi(j, \ell)$	> 1.0			
	$\Delta\phi(j, E_T^{\text{miss}})$	> 1.0			
	$\Delta\phi(j, j)$	< 1.5			
	$\Delta\phi(\ell, E_T^{\text{miss}})$	< 1.5			
	$\min(p_{T,\ell\nu}, p_{T,jj}) / m_{WV}$	$> 0.35(0.25)$ for DY/ggF (VBF) category			
Top veto	Number of additional b -tagged jets	0	≥ 1		
	Pass VBF selection	no (yes) for DY/ggF (VBF) category			

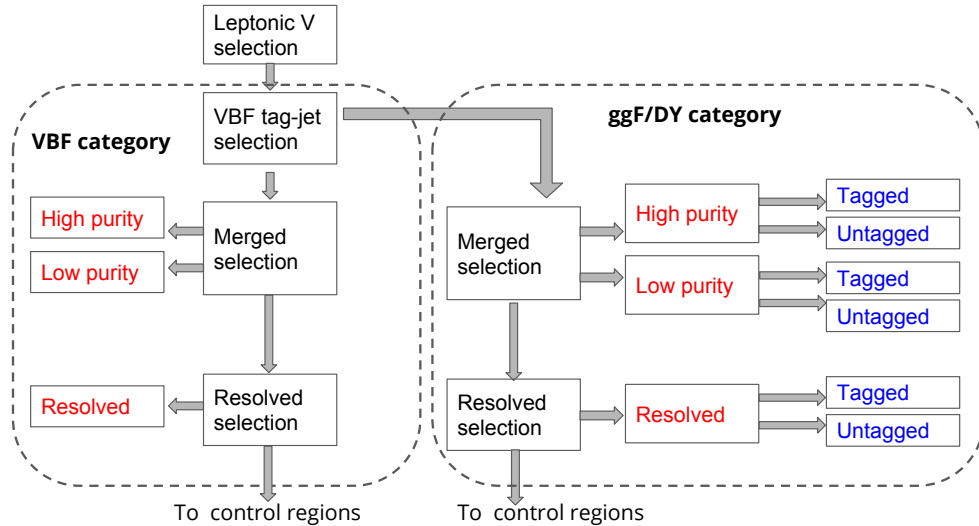


Figure 9.6: This diagram shows the prioritization scheme used to classify events into the various SRs and CRs. The VBF regions are prioritized over the non-VBF regions and the merged analysis is prioritized over the resolved analysis.

9.5 Selection Acceptance and Efficiency

The signal acceptance is the ratio of the number of signal events selected to the number of signal events generated at truth level, which does not account for detector effects. The signal efficiency is the ratio of the number of reconstructed events selected and the number of truth events selected, which accounts for detector effects. The expected number of signal events is given by the product of these two quantities:

$$A \cdot \epsilon = \frac{N_{\text{events selected}}^{\text{truth}}}{N_{\text{events generated}}^{\text{truth}}} \cdot \frac{N_{\text{events selected}}^{\text{reco}}}{N_{\text{events selected}}^{\text{truth}}} = \frac{N_{\text{events selected}}^{\text{reco}}}{N_{\text{events generated}}^{\text{truth}}} \quad (9.1)$$

The distributions of $A \cdot \epsilon$ as a function of the resonance mass for the different spin models are shown in Figures 9.7 - 9.8.

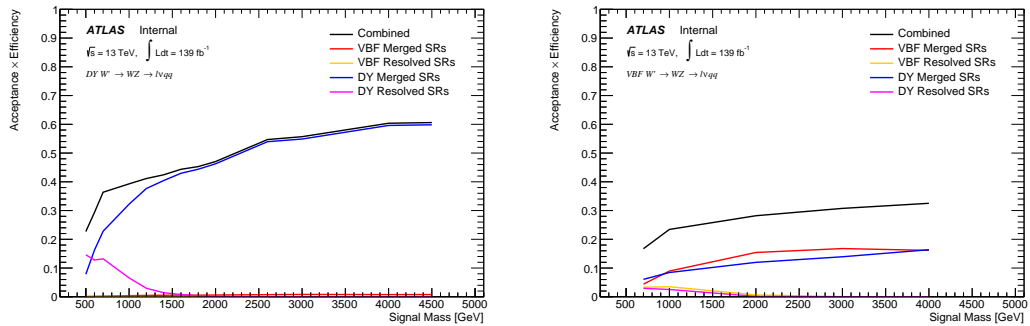


Figure 9.7: Selection acceptance times efficiency for the $W' \rightarrow WZ \rightarrow \ell\nu qq$ events from MC simulations as a function of the W' mass for Drell-Yan (left) and VBF production (right), combining the merged HP and LP signal regions of the $WV \rightarrow \ell\nu J$ selection and the resolved regions of the $WV \rightarrow \ell\nu jj$ selection. Note: the VBF selection acceptance for the DY W' is approximately zero in the left plot.

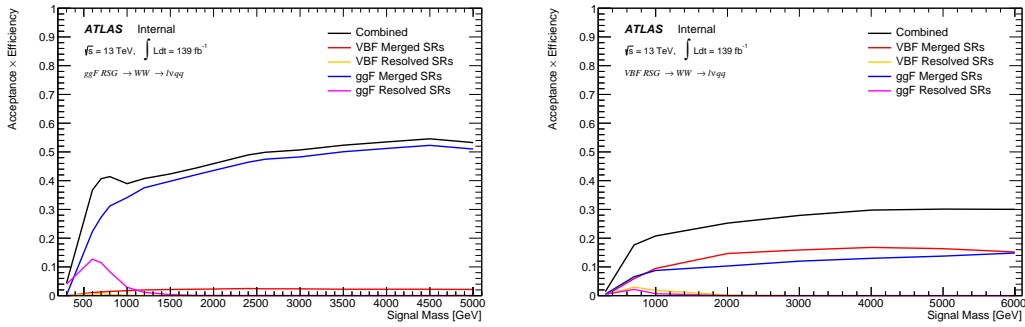


Figure 9.8: Selection acceptance times efficiency for the $G \rightarrow WW \rightarrow \ell\nu qq$ events from MC simulations as a function of the G mass for (a) Drell-Yan and (b) VBF production, combining the merged HP and LP signal regions of the $WW \rightarrow \ell\nu J$ selection and the resolved regions of the $WW \rightarrow \ell\nu jj$ selection. Note: the VBF selection acceptance for the ggF G''_{KK} is approximately zero in the left plot.

Chapter 10

Background Estimate

Backgrounds from VV , $t\bar{t}$, single-top, $W+\text{jets}$, $Z+\text{jets}$ are simulated as described in 7.2. The dominant backgrounds for this search are from $W+\text{jet}$ and $t\bar{t}$ processes. To more accurately model the m_{VV} distribution from these backgrounds in the SRs, CRs are constructed for each as described in 10.1. The $t\bar{t}$ and $W+\text{jets}$ control regions are called TCR and WCR, respectively. There are separate control regions for VBF and non-VBF regions as well as for each region (merged HP, merged LP, resolved). For the HVT W' search there are also tagged and untagged control regions (where tagged refers to events with two b -jets inside the large-R jet).

The shape of the aforementioned backgrounds containing real leptons are well-modeled with simulated samples. Backgrounds with fake leptons (also referred to as the multijet background) are not well-modeled with simulation. For this reason, the multijet background is extracted from data as described in 10.2.

10.1 Control Regions

The CRs are constructed to accurately model $W+\text{jets}$ and $t\bar{t}$, the two dominant backgrounds in this search. These control regions are dominated by these processes and constrain the normalization of these backgrounds in the final likelihood fit . The TCRs use the same selections as the SRs, but must also contain at least one b -jet in the event (that is not within the catchement area of the large-R jet for the merged analysis). The WCR shares the SR selections as well, but uses different jet mass requirements. For the merged analyses, the large-R jet must fail the W/Z tagger jet mass cut. In the resolved analyses, m_{jj} must be $50 < m_{jj} < 68$ GeV or $105 < m_{jj} < 150$ GeV.

The TCR distributions of variables used in merged analysis (e.g. m_{WV} , $p_T(\nu)$, $p_T(J)$), in the non-VBF and VBF: HP and LP regions, are shown in Figures 10.1-10.4. The TCR distributions for the variables used in the resolved analysis (e.g. m_{WV} , $p_T(\nu)$, $p_T(j_1), p_T(j_2)$) are shown in Figures 10.5 and 10.6. In general, in these plots the simulated distributions match the data well, which is necessary to have confidence in the prediction yields in the signal regions.

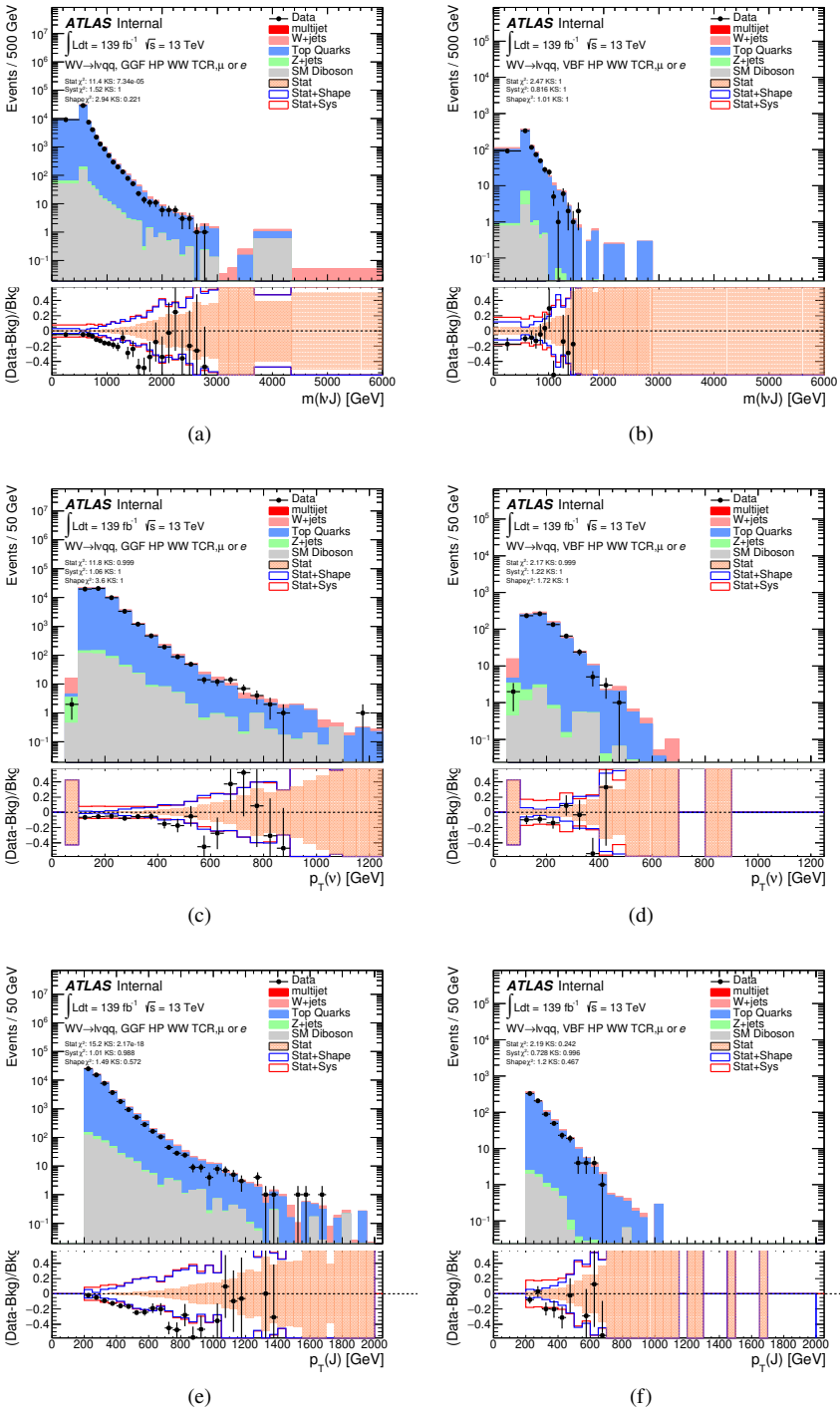


Figure 10.1: Data MC comparison for the merged WW HP TCR. The bottom panel shows the ratio of the difference between data and simulation to simulation. The red bands include the all systematic and statistical uncertainties on the background.

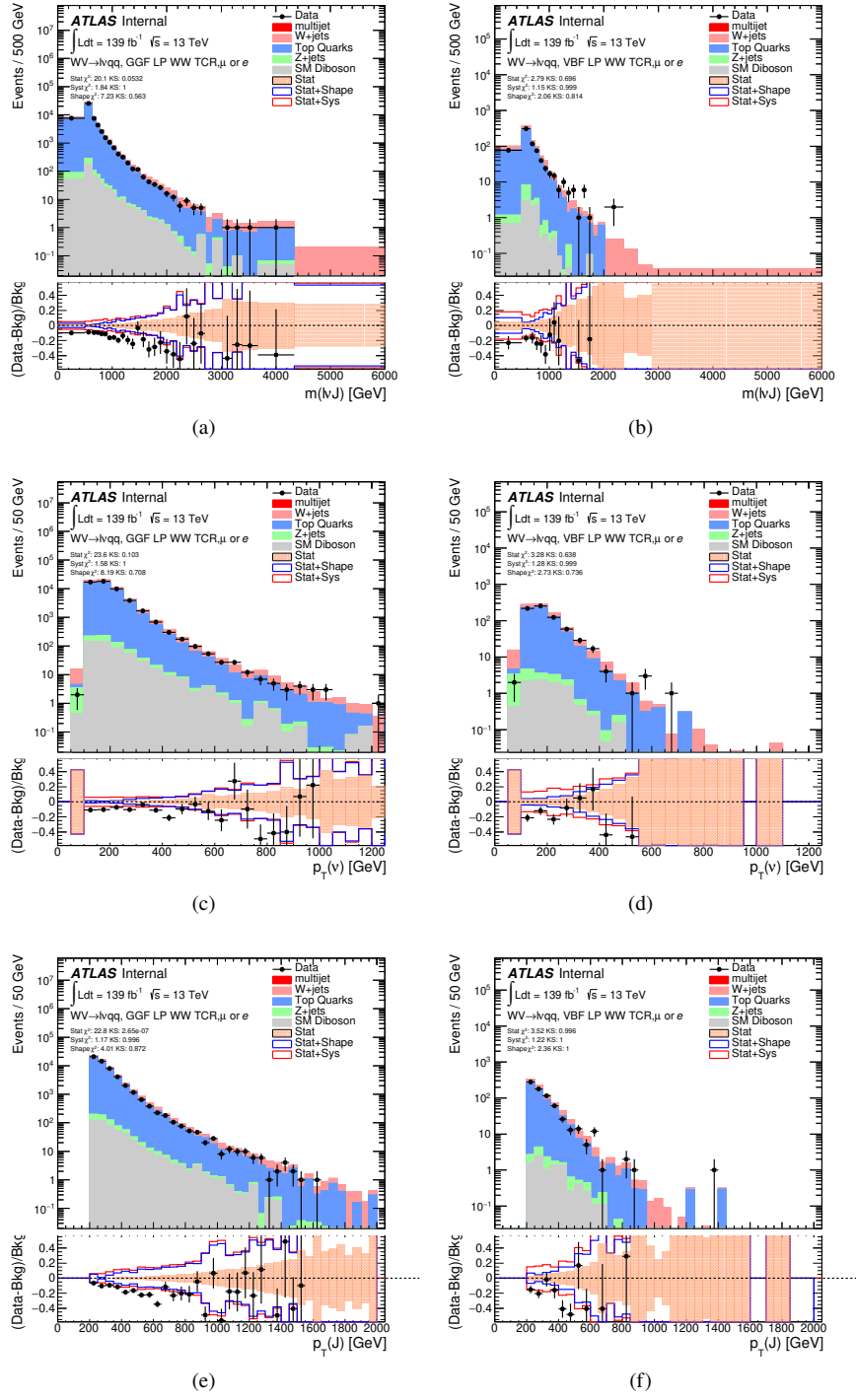


Figure 10.2: Data MC comparison for the merged WW LP TCR. The bottom panel shows the ratio of the difference between data and simulation to simulation. The red bands include the all systematic and statistical uncertainties on the background.

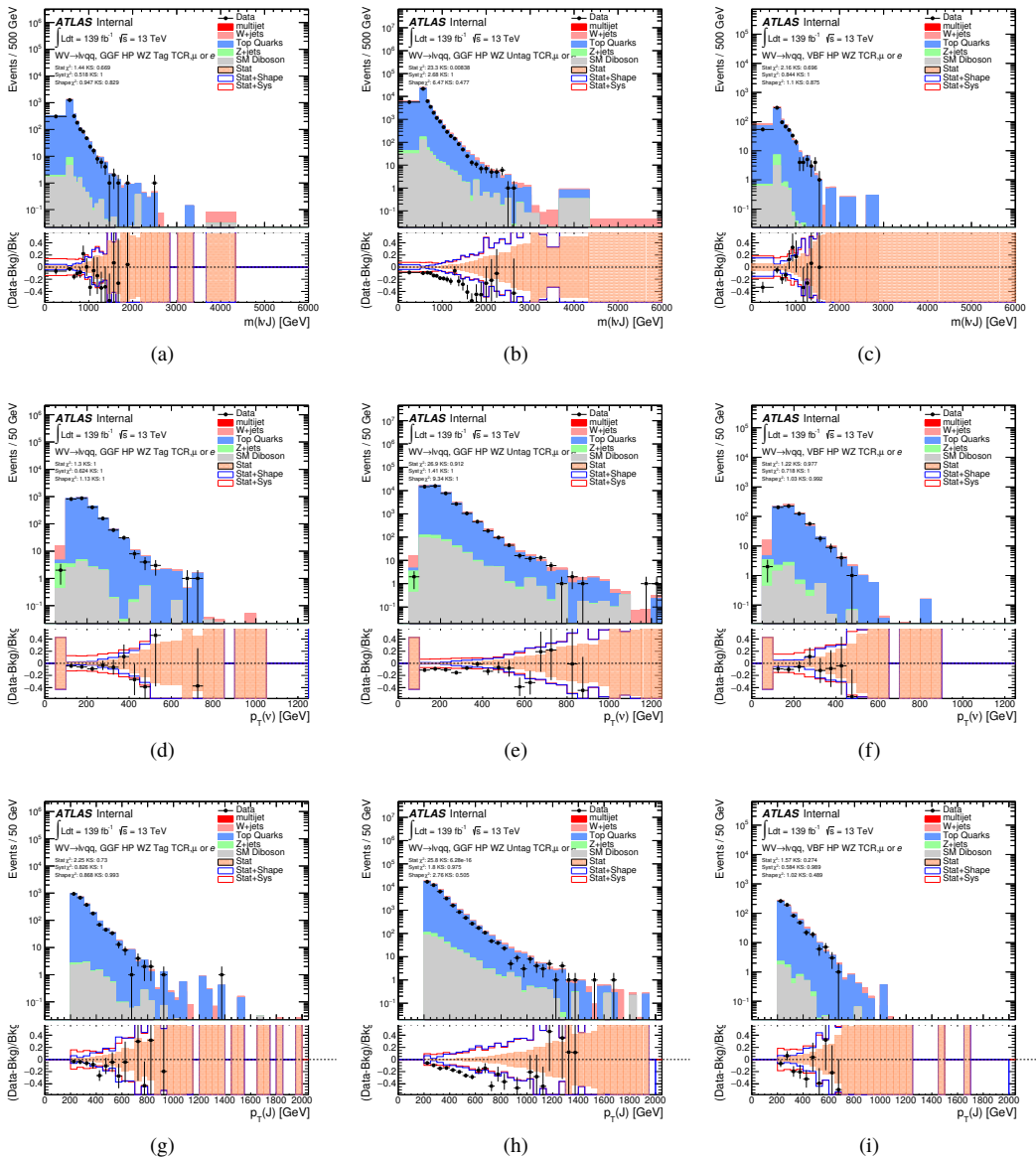


Figure 10.3: Data MC comparison for the merged WZ HP TCR. The bottom panel shows the ratio of the difference between data and simulation to simulation. The red bands include the all systematic and statistical uncertainties on the background.

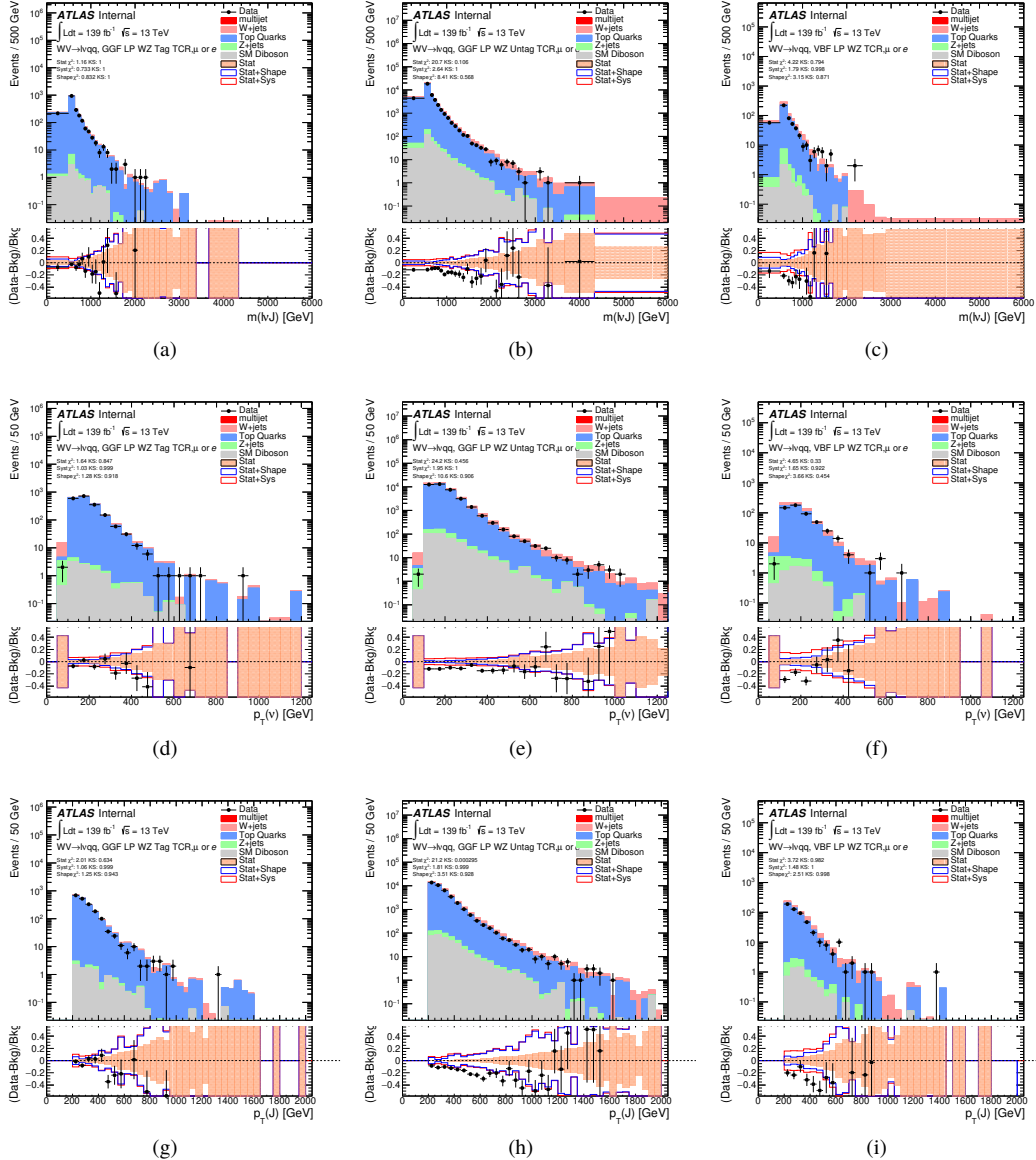


Figure 10.4: Data MC comparison for the merged WZ LP TCR. The bottom panel shows the ratio of the difference between data and simulation to simulation. The red bands include the all systematic and statistical uncertainties on the background.

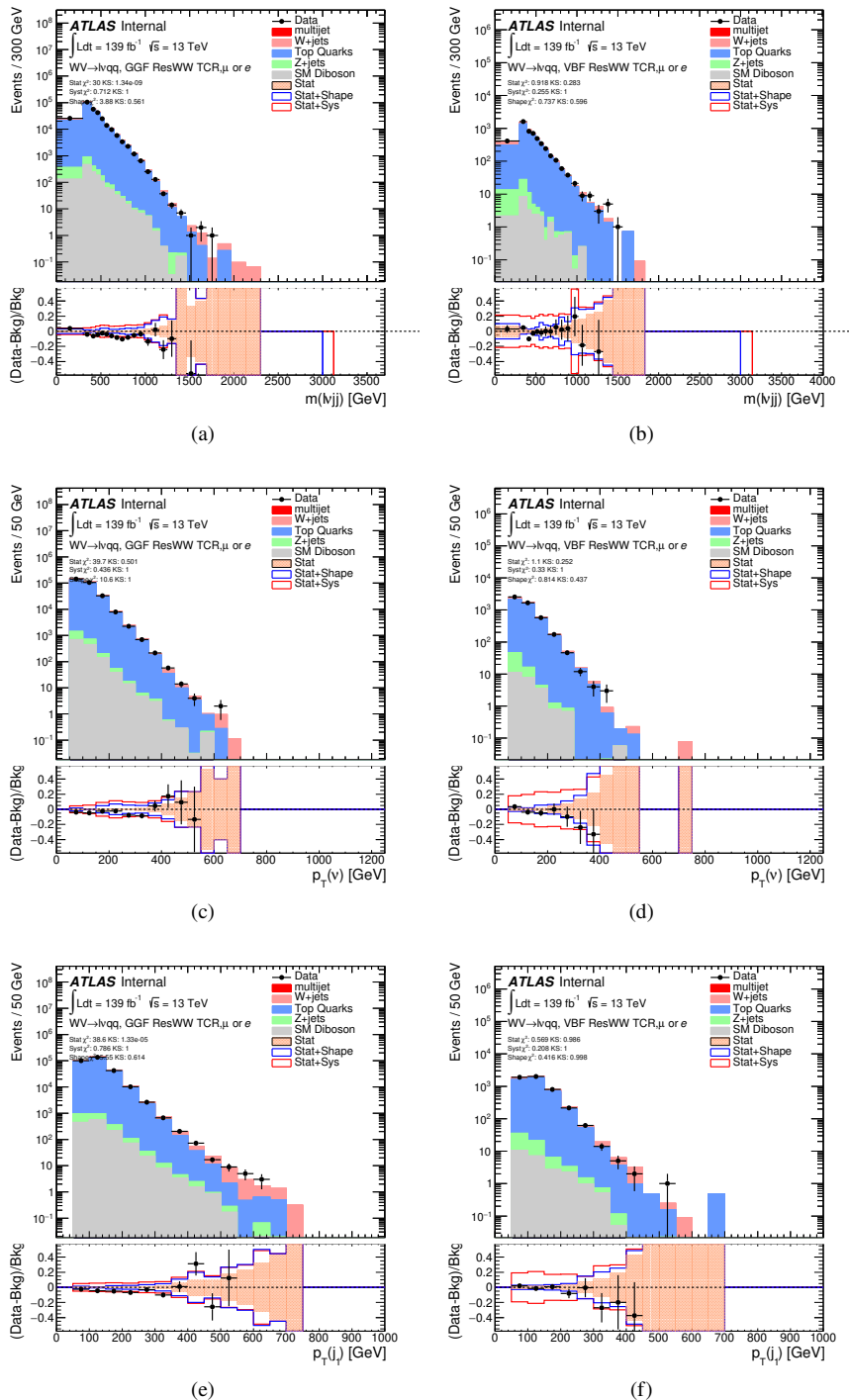


Figure 10.5: Data MC comparison for the resolved WW TCR. The bottom panel shows the ratio of the difference between data and simulation to simulation. The red bands include the all systematic and statistical uncertainties on the background.

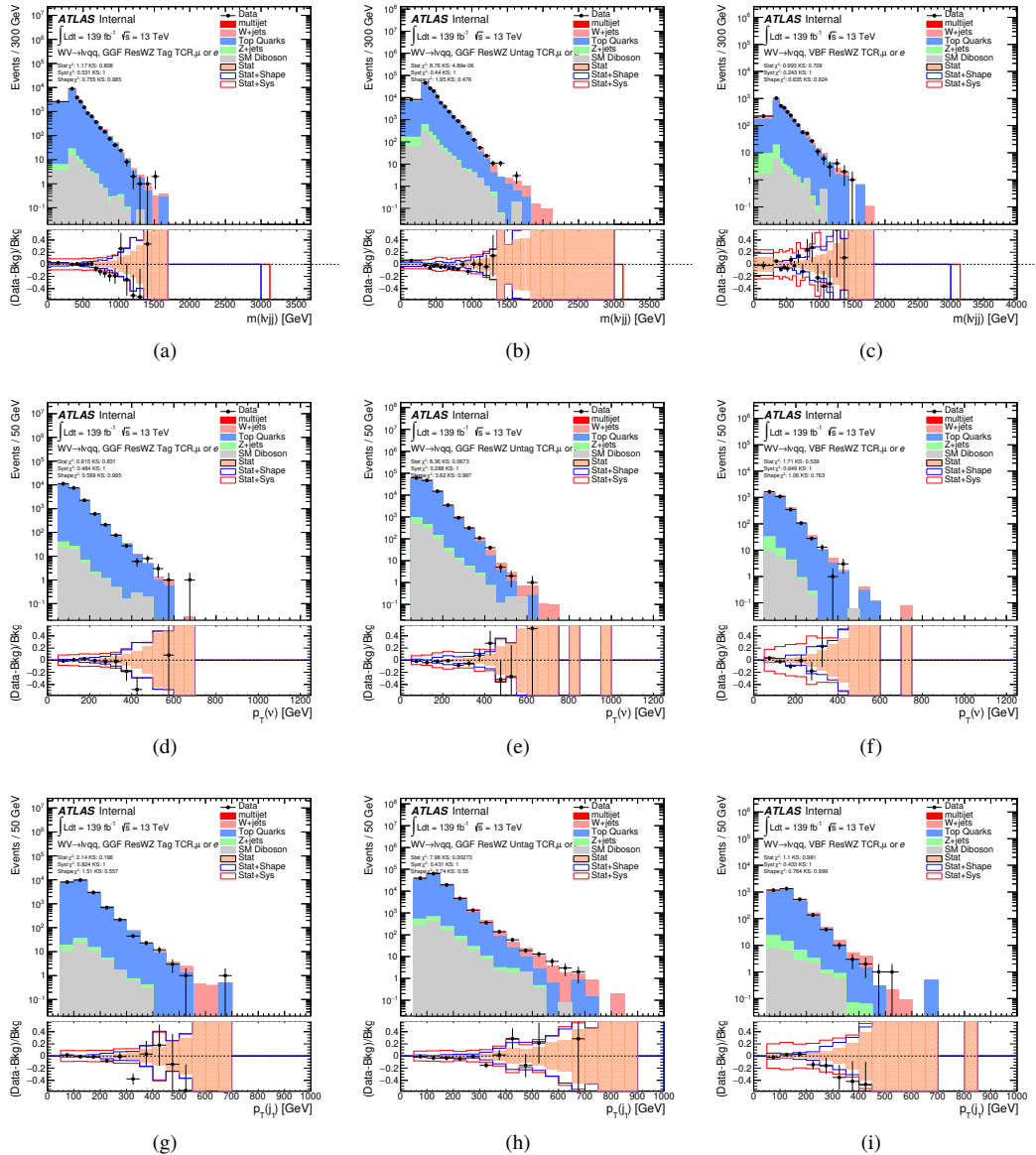


Figure 10.6: Data MC comparison for the resolved WZ TCR. The bottom panel shows the ratio of the difference between data and simulation to simulation. The red bands include the all systematic and statistical uncertainties on the background.

10.2 Fake Lepton Backgrounds

The fake lepton backgrounds for this search are not well-modeled with simulation. For this reason, this background is extracted from data. Fake electrons arise from fake jets and converted photons. Non-prompt muons often arise from heavy flavor decay products. This predominately occurs for lower lepton momentum, and therefore is only considered in the resolved analysis.

Fake electrons generally fail the electron ID criteria and fake muons fail the muon isolation requirement. Therefore, separate multijet samples are derived for the fake electron and muon samples. For each sample the m_{WV} template shape is derived for the SR and WCR selections using the same SR and WCR cuts but with inverted lepton requirements as seen in Table 10.1. NB: By inverting the lepton isolation/identification criteria the SRs and CRs are orthogonal.

To derive the multijet template in a given SR, first the multijet template in the WCR is derived, called the MJCR template. This template is calculated using events that pass the WCR selection but with the inverted lepton criteria. The E_T^{miss} distribution for the MJCR is given by the difference between data and the simulated samples in the MJCR. The E_T^{miss} distribution of those events is then added to the simulated backgrounds in the WCR. The floating background and multijet normalizations of the MJCR in this region are then fit to the data. The fitted MJCR is then used as the multijet sample in the WCR.

The fitted normalizations from the MJCR template are then used to construct the multijet template in the SR (MJSR). The MJSR is constructed from events that pass the SR selections but with the inverted lepton criteria. Again, the difference between the data and simulated backgrounds in this region gives MJSR template shape in m_{WV} . This shape is then scaled by the fitted normalizations from the MJCR. These fitted electron and muon muon multijet templates are then

used as the multijet samples in the SRs. The normalizations of the electron and muon multijet samples are parameters in the final likelihood fit.

This template method was validated using WCR and full Run 2 data. The results of the fit are shown in Table 10.2. The multijet contribution in the muon channel for $p_T^W > 150$ GeV is consistent with zero, and therefore neglected in the final fit. Applying the extracted normalization factor to MJCR in WCRs for various kinematic variables such as E_T^{miss} , W transverse mass, lepton p_T , and the invariant mass as show in Figures 10.8 -10.17. These figures show good agreement between the data and background estimate.

Table 10.1: Definitions of “inverted” leptons used in multijet control region. For the inverted muon selection, $ptvarcone30$ is given by sum of the p_T of tracks in a cone around the muon candidate divided by the muon p_T . The size of the cone, δR used is $10\text{GeV}/p_T^\mu$ or 0.3, whichever is smaller. So, as the p_T of the muon increases, the cone size used decreases. This is useful as more boosted muons are more likely to be produced in dense environments and using a smaller cone size more accurately determines the quality of the muon.

	Criterion	signal lepton	inverted lepton
Electron	ID	TightLH	MediumLH !TightLH
	Calo Isolation	FixedCutHighPtCaloOnlyIso	FixedCutHighPtCaloOnlyIso
Muon	ID	WHSignalMuon	WHSignalMuon
	Track Isolation	FixedCutTightTrackOnlyIso	!FixedCutTightTrackOnlyIso $ptvarcone30/p_t < 0.07^*$
*Only applied to events with $pTW < 150\text{GeV}$			

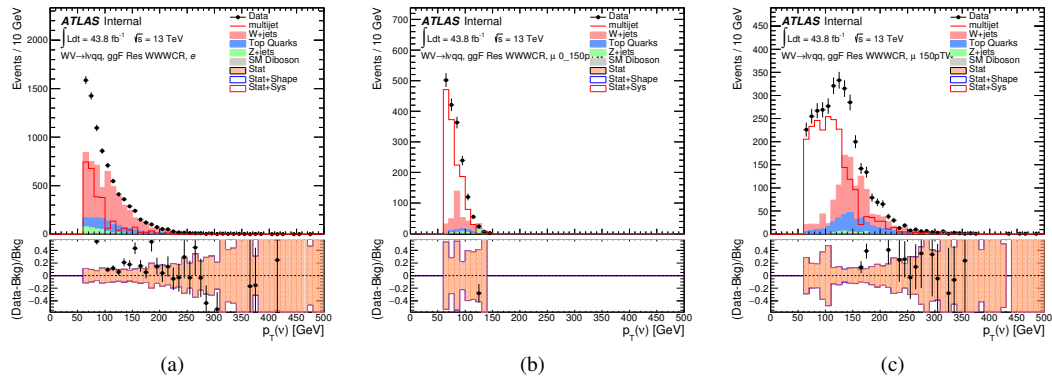


Figure 10.7: The E_T^{miss} distribution in MJCR for 2017 data in the electron channel(left), muon channel with W-boson $p_{\text{T}} < 150$ GeV (center) and > 150 GeV (right). Multi-jet templates are given by the difference between the data and simulated distributions.

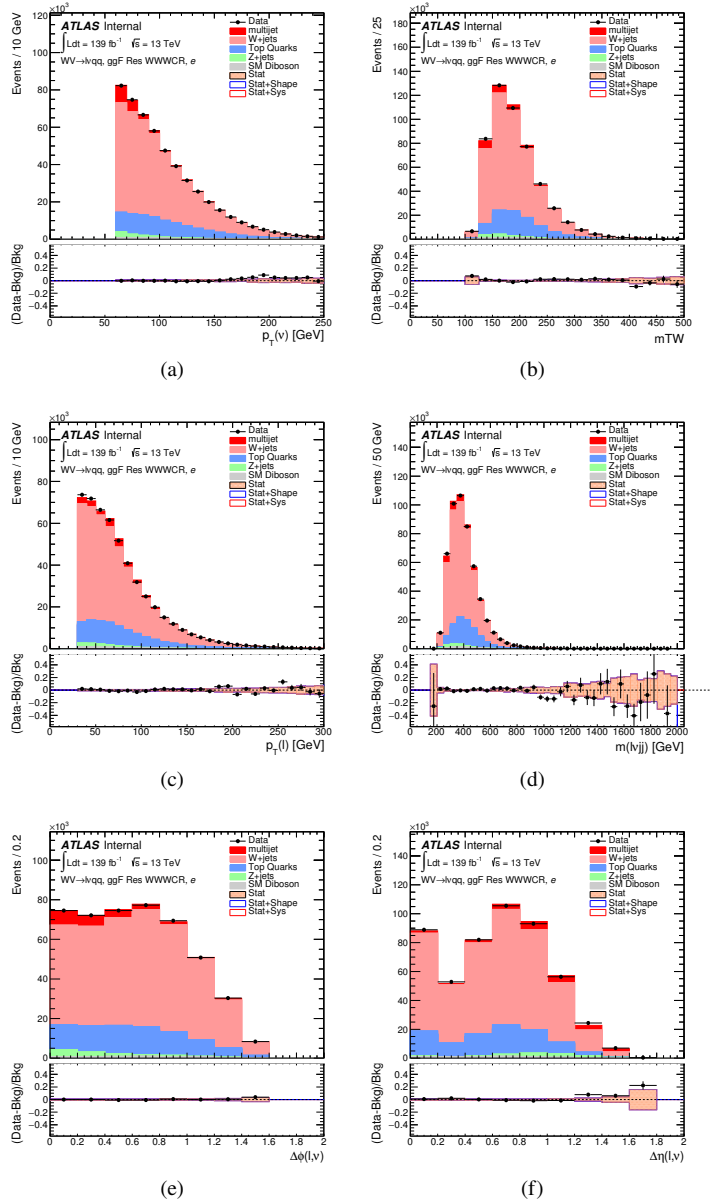


Figure 10.8: Postfit Data/MC comparison of distributions of E_T^{miss} , m_T , lepton and neutrino p_T , $m_{l\nu jj}$, lepton- ν angular distance in the WW electron channel. The MJ template is obtained from the pre-MJ-fit.

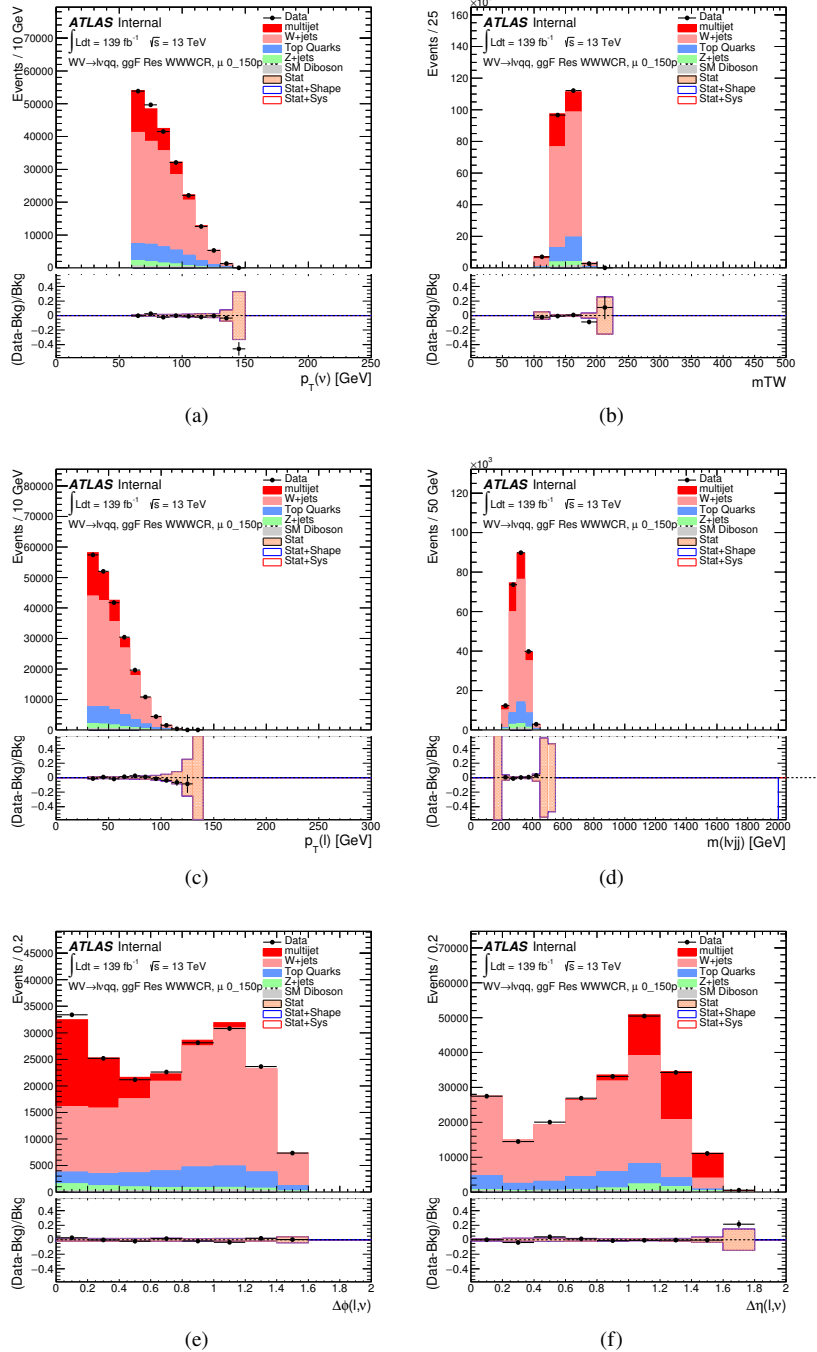


Figure 10.9: Postfit Data/MC comparison of distributions of E_T^{miss} , m_T^W , lepton and neutrino p_T , $m_{\ell\nu jj}$, lepton- ν angular distance in the WW muon channel. The MJ template is obtained from the pre-MJ-fit.

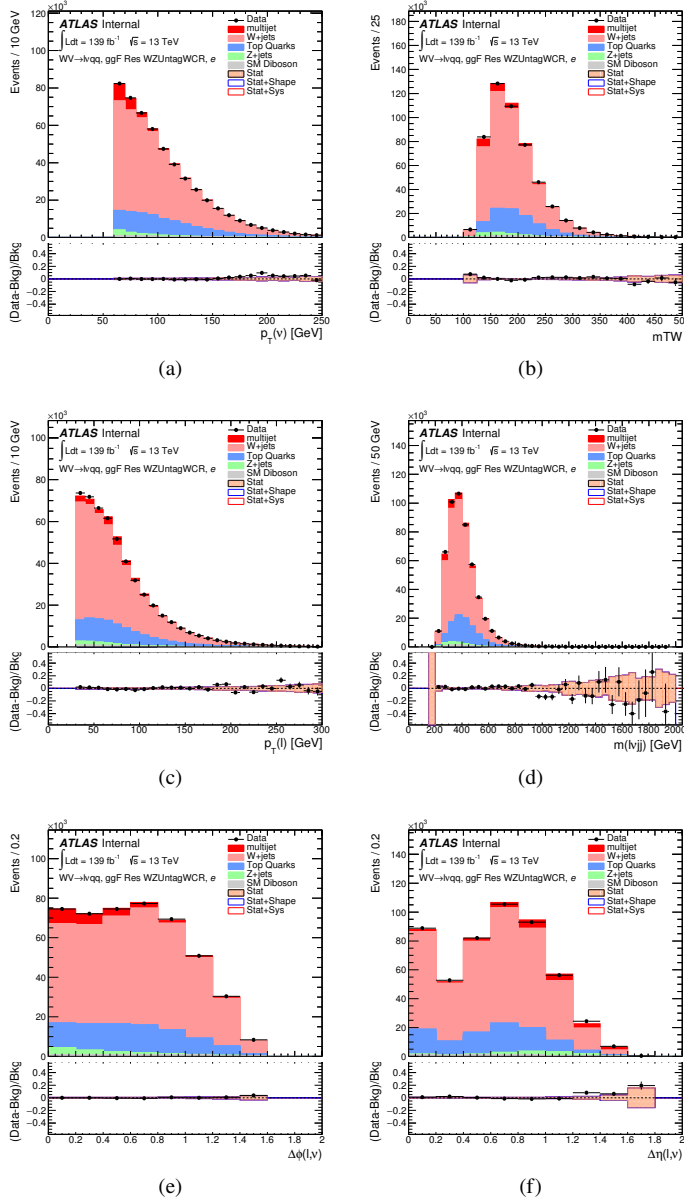


Figure 10.10: Postfit Data/MC comparison of distributions of E_T^{miss} , m_T^W , lepton and neutrino p_T , $m_{l\nu jj}$, lepton- ν angular distance in the WZ untag electron channel. The MJ template is obtained from the pre-MJ-fit.

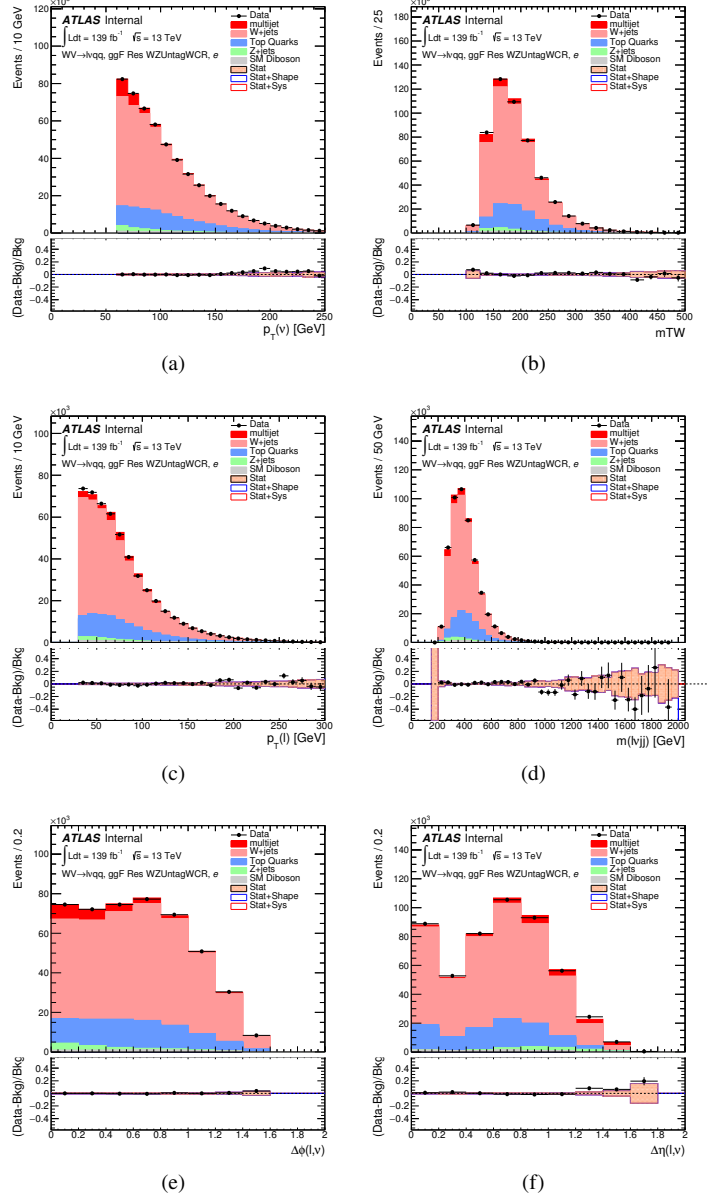


Figure 10.11: Postfit Data/MC comparison of distributions of E_T^{miss} , m_T^W , lepton and neutrino p_T , $m_{\ell\nu jj}$, lepton- ν angular distance in the WZ untag muon channel. The MJ template is obtained from the pre-MJ-fit.

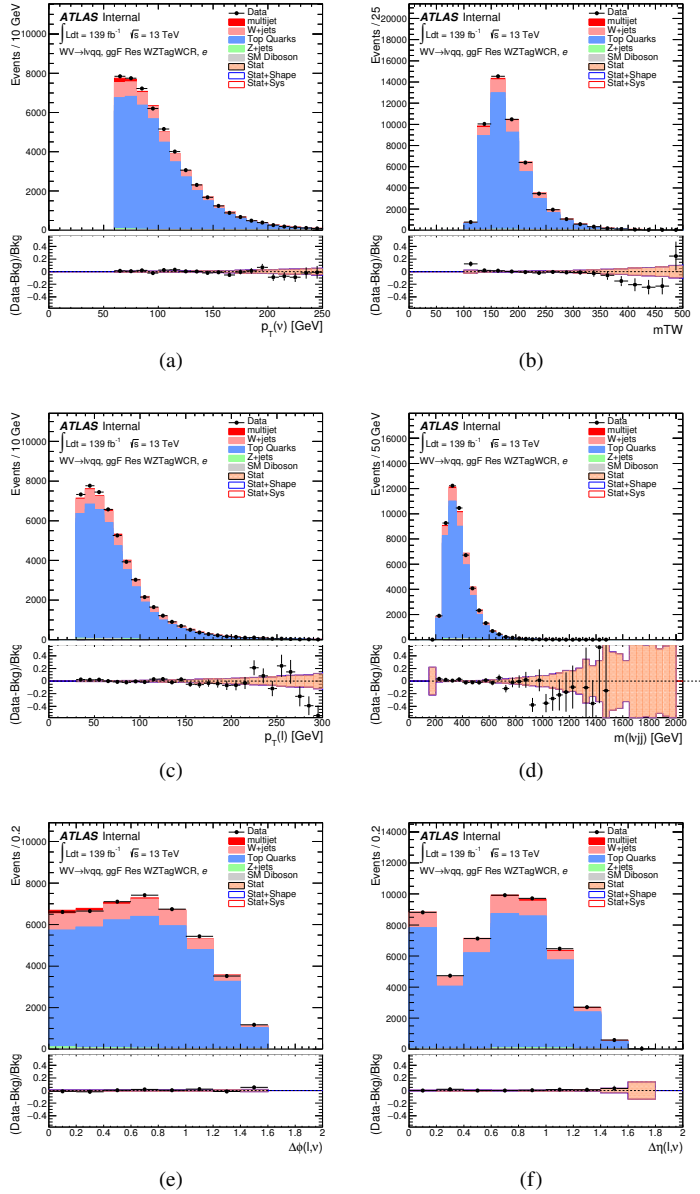


Figure 10.12: Postfit Data/MC comparison of distributions of E_T^{miss} , m_T^W , lepton and neutrino p_T , $m_{\ell\nu jj}$, lepton- ν angular distance in the WZ untag electron channel. The MJ template is obtained from the pre-MJ-fit.

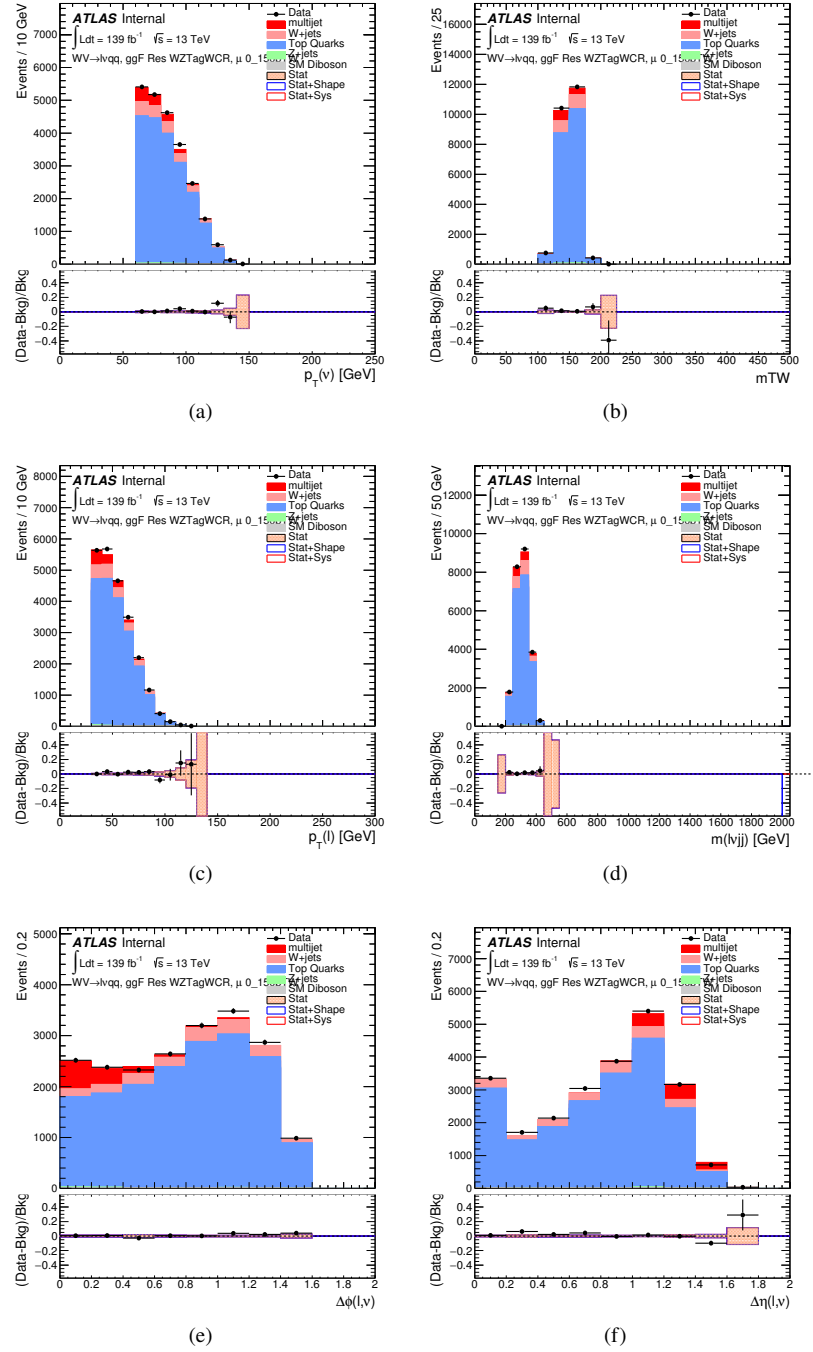


Figure 10.13: Postfit Data/MC comparison of distributions of E_T^{miss} , m_T , lepton and neutrino p_T , $m_{l\nu jj}$, lepton- ν angular distance in the WZ untag muon channel. The MJ template is obtained from the pre-MJ-fit.

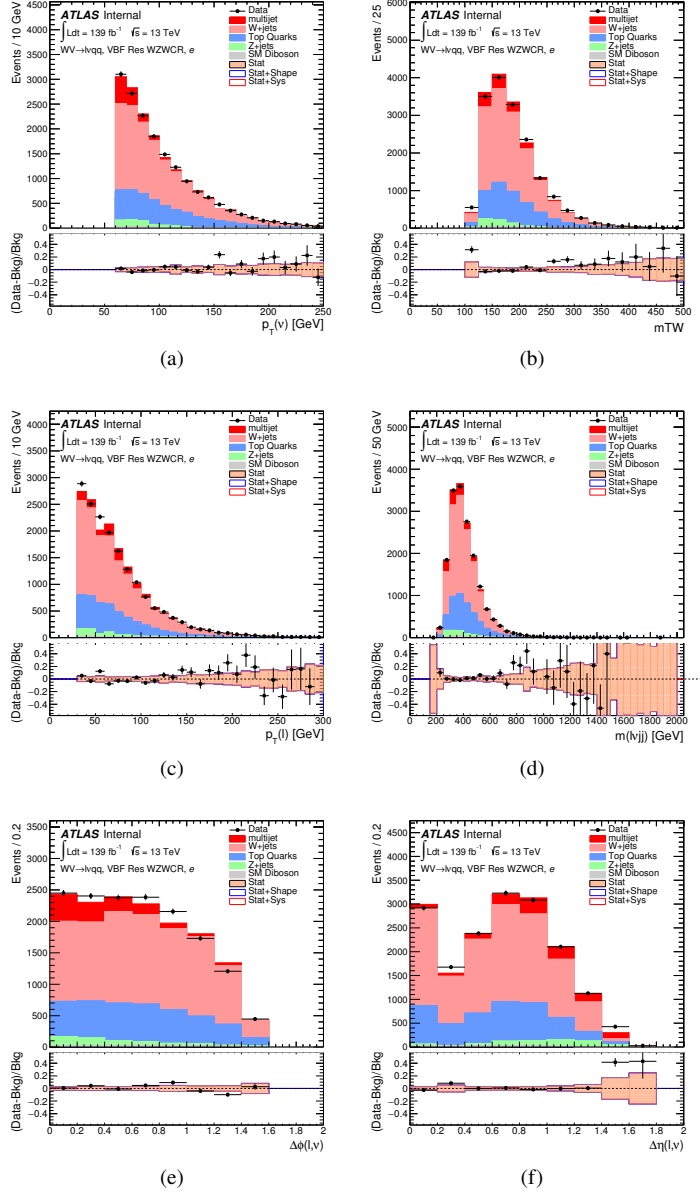


Figure 10.14: Postfit Data/MC comparison of distributions of E_T^{miss} , m_T^W , lepton and neutrino p_T , $m_{l\nu jj}$, lepton- ν angular distance in the VBF WW electron channel. The MJ template is obtained from the pre-MJ-fit.

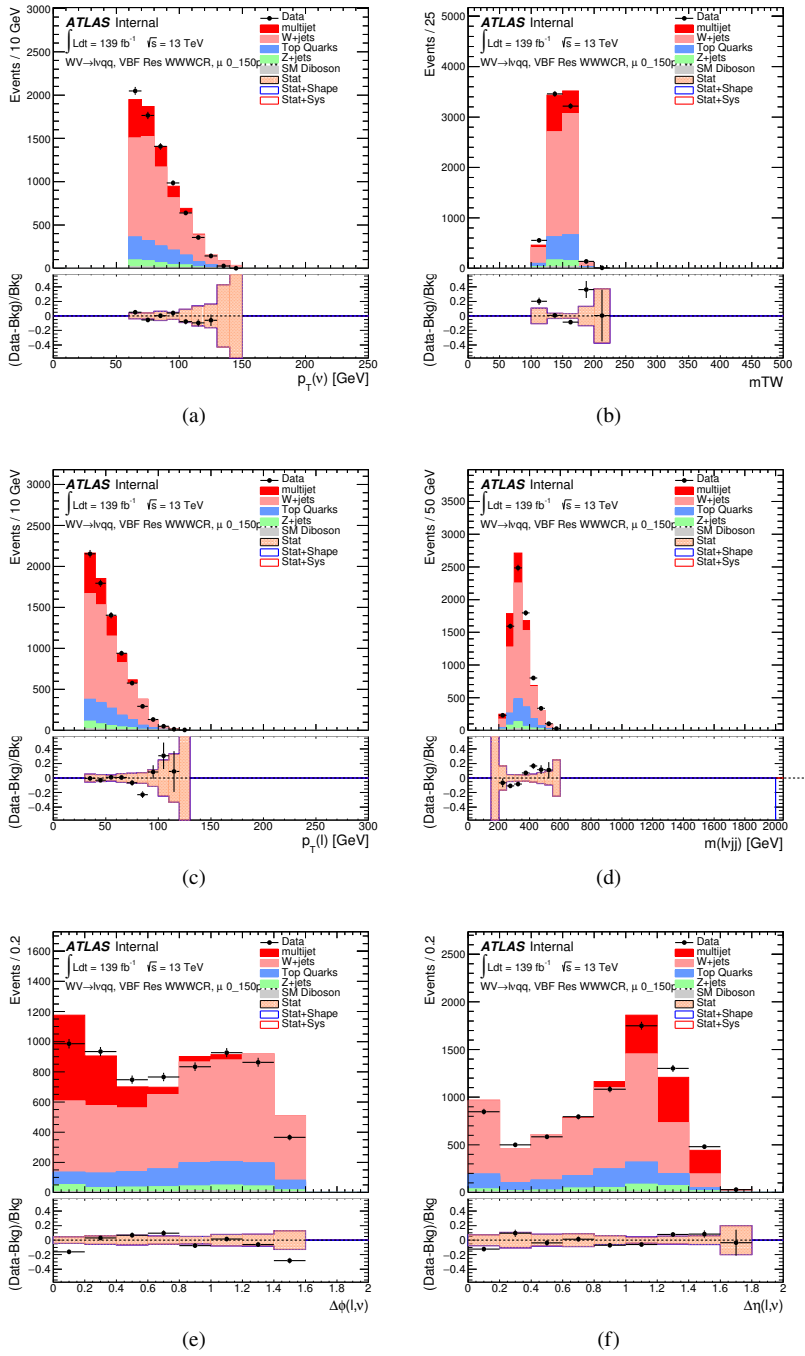


Figure 10.15: Postfit Data/MC comparison of distributions of E_T^{miss} , m_T^W , lepton and neutrino p_T , $m_{l\nu jj}$, lepton- ν angular distance in the VBF WW muon channel. The MJ template is obtained from the pre-MJ-fit.

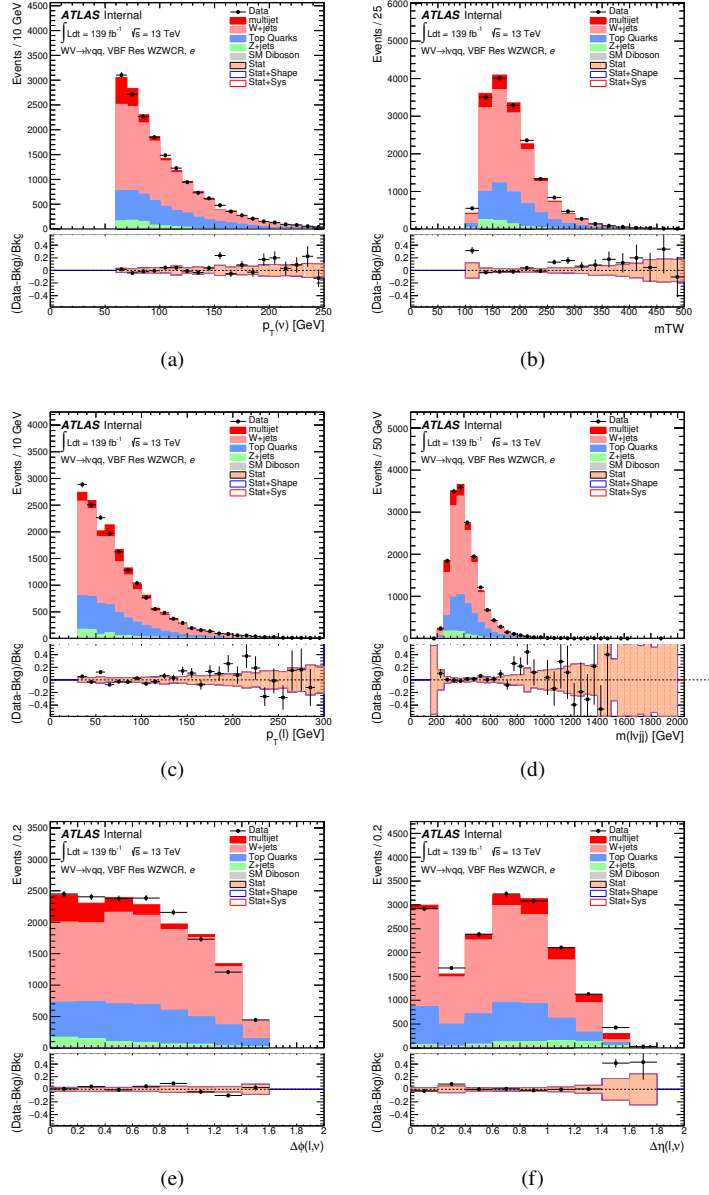


Figure 10.16: Postfit Data/MC comparison of distributions of E_T^{miss} , m_T^W , lepton and neutrino p_T , $m_{\ell\nu jj}$, lepton- ν angular distance in the VBF WZ electron channel. The MJ template is obtained from the pre-MJ-fit.

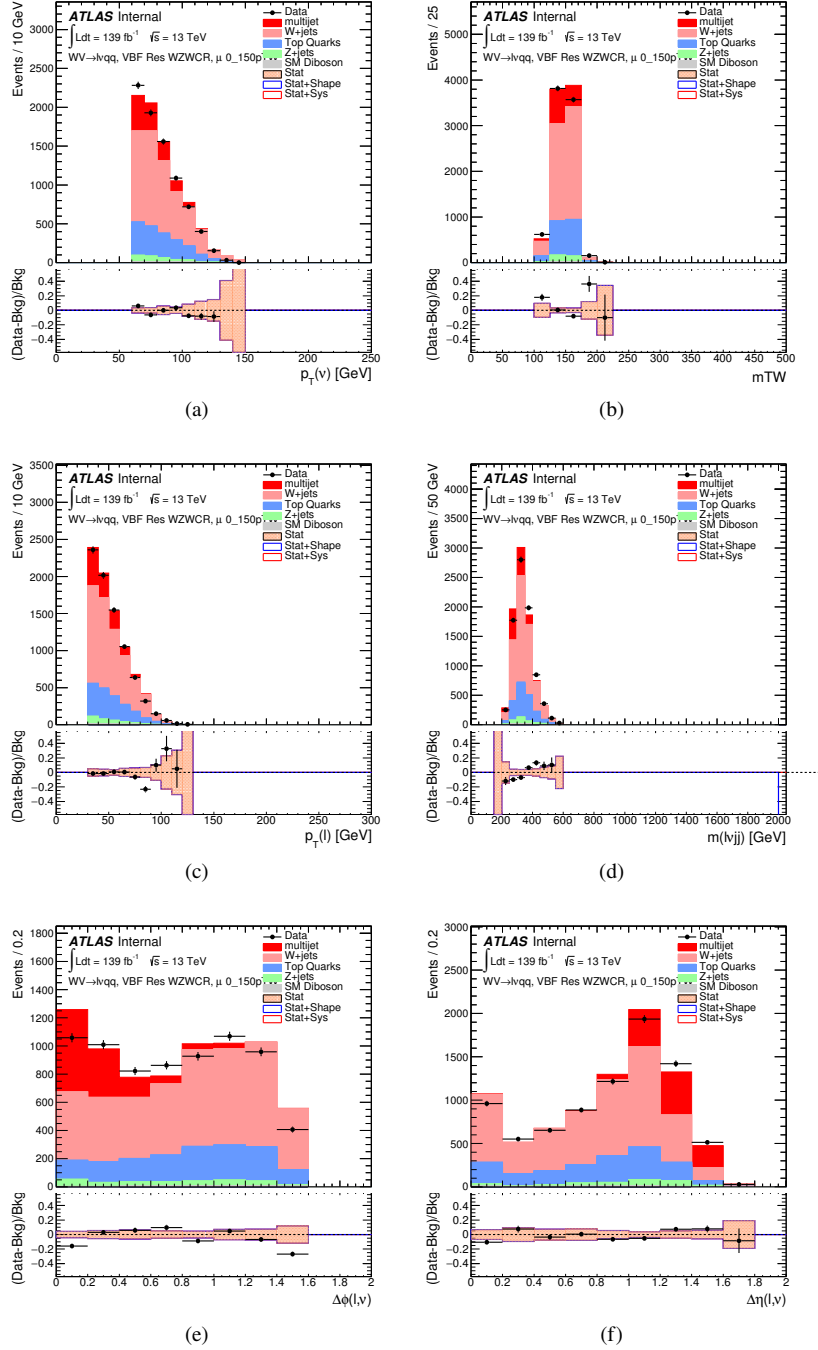


Figure 10.17: Postfit Data/MC comparison of distributions of E_T^{miss} , m_T^W , lepton and neutrino p_T , $m_{l\nu jj}$, lepton- ν angular distance in the VBF WZ muon channel. The MJ template is obtained from the pre-MJ-fit.

Region	Sample	Yield	R.U.	SF
non-VBF WW WCR	Top&W	650000 ± 1900	0.31%	0.99
	Z&VV	24000	fixed	
	MJ_el	24000 ± 1200	5.1%	4.0
	MJ_mu	35000 ± 920	2.6%	9.0
non-VBF WZ untag	Top&W	640000 ± 1900	0.31%	0.99
	Z&VV	24000	fixed	
	MJ_el	24000 ± 1200	5.1%	3.9
	MJ_mu	36000 ± 920	2.6%	8.7
non-VBF WZ tag	Top&W	71000 ± 690	0.97%	1.0
	Z&VV	520	fixed	
	MJ_el	600 ± 450	75%	0.094
	MJ_mu	1200 ± 220	19%	0.29
VBF WW WCR	Top&W	19000 ± 360	1.9%	0.93
	Z&VV	1100	fixed	
	MJ_el	1400 ± 210	15%	0.24
	MJ_mu	1300 ± 160	11%	0.31
VBF WZ WCR	Top&W	21000 ± 390	1.8%	0.94
	Z&VV	1100	fixed	
	MJ_el	1400 ± 230	16%	0.23
	MJ_mu	1300 ± 160	12%	0.31

Table 10.2: Fit validation result in WCRs for 2015+16 data. The fit is done in various WCRs, in order to obtain the corresponding scale factors for MJ templates: non-VBF resolved WCR for the $WW \rightarrow lvqq$ selection, non-VBF resolved untagged WCR for the $WZ \rightarrow lvqq$ selection, non-VBF resolved tagged WCR for the $WZ \rightarrow lvqq$ selection, VBF resolved WCR for the $WW \rightarrow lvqq$ selection, and VBF resolved WCR for the $WZ \rightarrow lvqq$ selection. Post-fit event yields for electroweak processes and MJ contributions are shown. The SF column shows the corresponding normalization scale factors for electroweak processes from the fit. R.U. stands for relative uncertainty.

Chapter 11

Systematic Uncertainties

This section describes the sources of systematic uncertainties of the m_{WV} distribution. These uncertainties are divided into experimental and modeling uncertainties. Each systematic uncertainty is treated as a nuisance parameter in the final likelihood fit. The dominant systematics in this analysis arise from jet reconstruction and the generator choice for the $V + \text{jets}$ backgrounds.

11.1 Experimental Systematics

The uncertainty on the integrated luminosity of the dataset used is 1.7% and a systematic in the final fit. This uncertainty was calculated using $x - y$ beam separation scans [18].

Another source of systematic uncertainty is assigned to the pileup modeling in MC samples. This ensures simulated detector response and particle reconstruction conditions are as similar as possible. The distribution of the average number of interactions per bunch crossing applied to simulation is called the μ profile. The pileup modeling uncertainty is accounted for by reweighting simulated events so the average number of interactions per bunch crossing varies within its uncertainty

due to systematics from vertex reconstruction [46]. The associated reweighting factors are propagated through the entire analysis chain to construct a systematic uncertainty on m_{VV} .

The single-lepton and E_T^{miss} triggers used are not fully efficient, so scale factors are applied to simulation to more accurately model the data. These scale factors are given by the ratio of the distribution of offline objects before trigger selection and after trigger selection. The associated uncertainty on these scale factors are used in the final fit.

Uncertainties on small-R jet energy scale and resolution are measured in-situ by calculating the response between data and simulation. This analysis uses a reduced set of jet energy scale and resolution (JES and JER, respectively) uncertainties (totaling 30 and 8 systematics, respectively). This reduced set of systematics is determined using a principal component analysis, yielding largely uncorrelated independent systematics. The JES and JER systematics account for the dependence on p_T , η , μ , flavor response and global sequential corrections. Systematic uncertainties associated with b -tagging are also considered. These systematics are evaluated as scale factor uncertainties, accounting for the difference in b -tagging efficiencies in data and MC, and the flavor dependence (between b , c , and light jets).

The p_T scale uncertainty of the large-R jets is determined by comparing the jet's p_T^{calo} to p_T^{track} in di-jet simulation and data. In addition to this, uncertainties from tracking, modeling (Pythia vs Herwig), and statistical constraints are also used. The large-R jet p_T resolution is given by smearing the jet p_T with a Gaussian with a 2% width.

The W/Z tagging efficiency scale factor is estimated by comparing the tagging efficiency in simulation with that in data for four regions of the W/Z tagger (D_2

fail, m_J fail; D_2 pass, m_J fail; D_2 fail, m_J pass; D_2 pass, m_J pass). Additionally, separate scale factors are determined for events with large-R jets from W bosons and top backgrounds. A simultaneous template fit is used to fit the signal jets (jets initiated by W/Z bosons or top quarks) and background jets (all other jets from the simulated backgrounds) to the data in the four regions using the m_J distributions. The scale factor for a given region is then given by:

$$SF = \frac{\epsilon_{data} = \frac{N_{fitted-signals}^{region}}{N_{fitted-signals}^{all-regions}}}{\epsilon_{MC} = \frac{N_{signal}^{region}}{N_{signal}^{all-regions}}} \quad (11.1)$$

The effects of experimental and theoretical uncertainties on the efficiency scale factor are determined by taking the ratio of efficiencies in data and simulation. By taking this ratio, uncertainties not arising for jet mass and D_2 cancel.

Lepton identification, reconstruction, isolation systematic uncertainties are determined by reconstructing the Z mass peak with a tag and probe method ([6],[28]). The lepton energy and momentum scales are also measured with the Z mass peak. The effect of these systematics on the m_{WV} distribution are < 5%.

As E_T^{miss} is calculated using all the physics objects in the event, all those objects associated errors result in an uncertainty on E_T^{miss} . Additionally, the unassociated tracks used to construct E_T^{miss} contribute to the uncertainty on E_T^{miss} .

11.2 Theoretical Systematics

Theoretical uncertainties for signal and background processes arise from uncertainties in MC parameters used. In particular for the $t\bar{t}$, $W/Z+jets$, diboson backgrounds and signal samples, the QCD scale, PDF, generator and hadronization uncertainties are considered. To assess the QCD scale uncertainty, the renor-

malization and factorization scales are scaled up and down by a factor of two at the event generation stage of sample production. Uncertainties from the PDF choice are evaluated by reweighting samples from the nominal PDF to a set of error PDFs which account for the uncertainty of the fits used to produce the PDF set. In addition to this, samples are re-weighted to different PDF sets to account for the arbitrariness of the PDF choice. The difference between the m_{WV} distributions using different event generators is assessed by comparing samples generated with different generators. Similarly, the uncertainty in hadronization models is accounted for by comparing samples created using different hadronization models (e.g. $t\bar{t}$ Powheg is compared to aMC@NLO, W +jets compares Sherpa and MadGraph+Pythia samples). Figures 11.1 - 11.8 show the impact of these uncertainties on the $t\bar{t}$ and $W/Z + \text{jets}$ backgrounds. Additionally, contributions to the diboson background for the VBF analysis were found to be small and are accounted for by including a 10% systematic in the diboson normalization in the final fit.

The normalization of the $t\bar{t}$ and W +jets processes impact the fake lepton template shape. The impact of these normalizations was assessed by including a shape systematic on the multijet background from varying the $t\bar{t}$ and W +jets normalization factors. The overall normalization of the template is a systematic in the final likelihood fit (account for other systematic effects on the template).

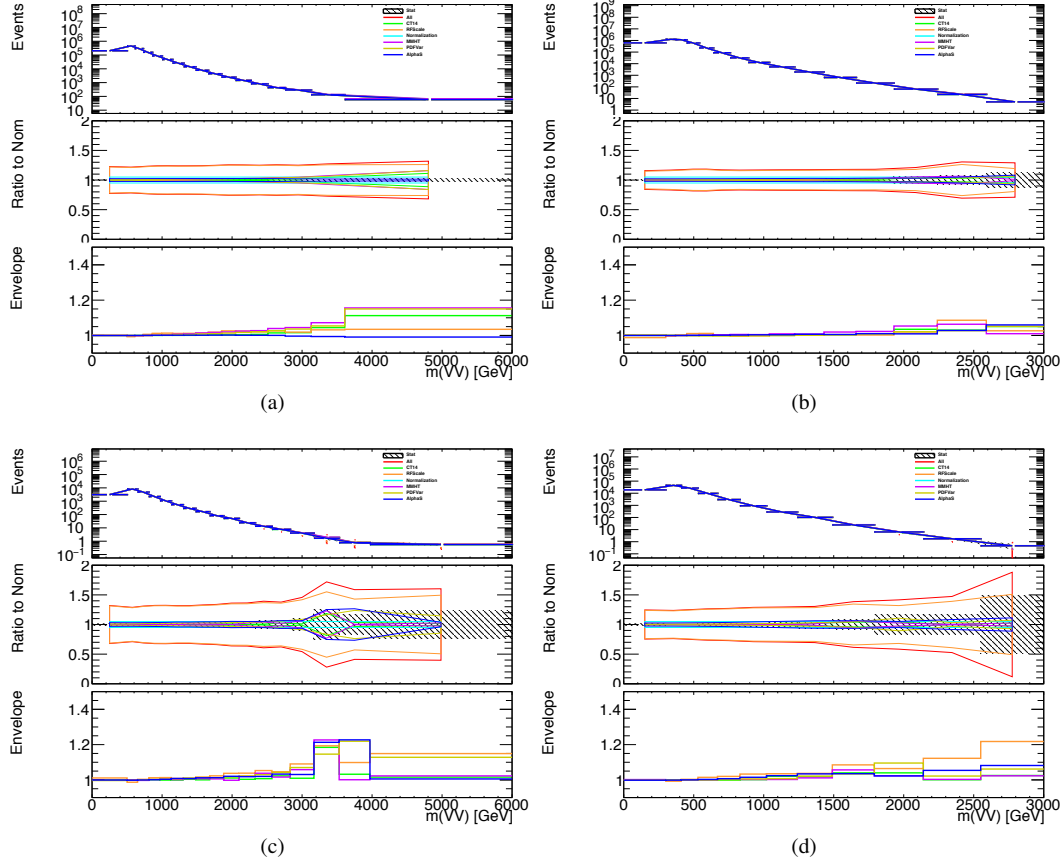


Figure 11.1: The $W/Z + \text{jet}$ systematics for the a) Merged ggF, b) Resolved ggF, c) Merged VBF, and d) Resolved VBF regions. The top subplot shows the nominal and variation distributions/bands, the middle shows the ratio of the two, and the final shows just the shape of the envelope (the final uncertainty).

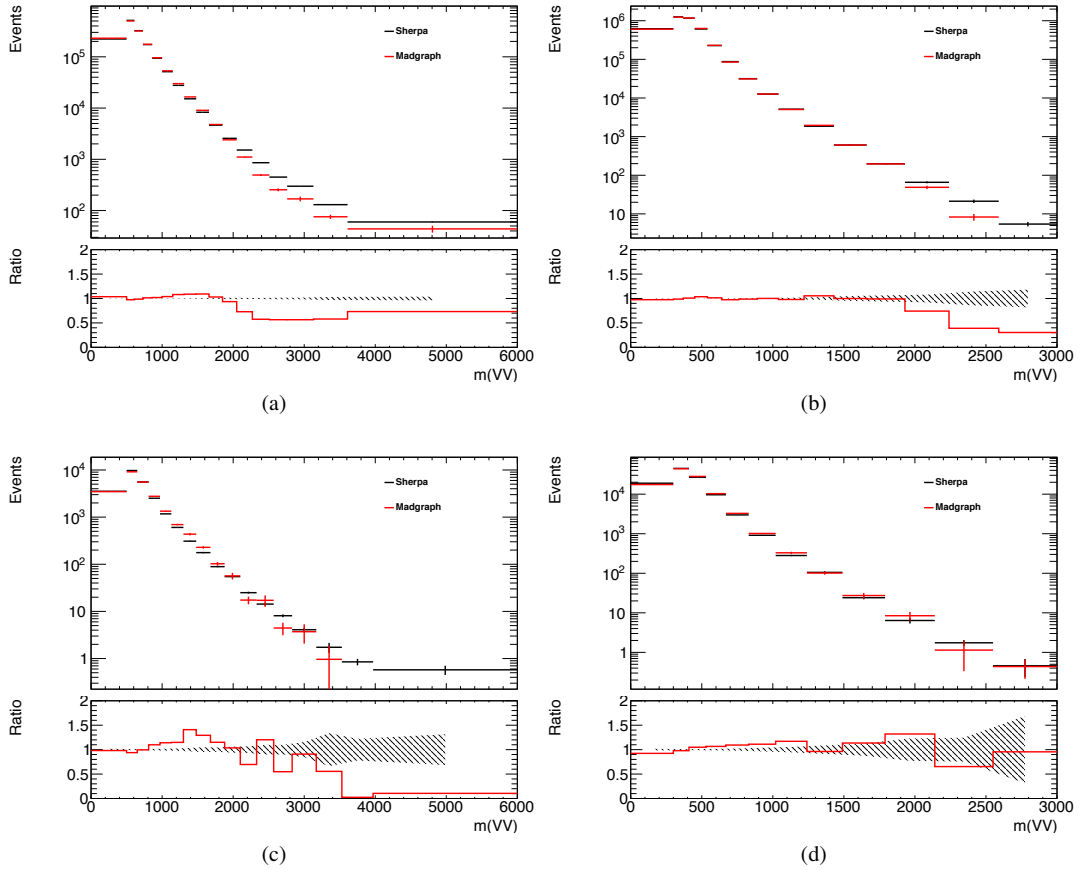


Figure 11.2: The two-point generator comparison between Sherpa and MadGraph for the $W/Z + \text{jet}$ samples in the a) Merged ggF, b) Resolved ggF, c) Merged VBF, and d) Resolved VBF regions. The normalization of the Madgraph sample is set to the Sherpa value to consider only shape effects. The bottom inlet shows the ratio of the two.

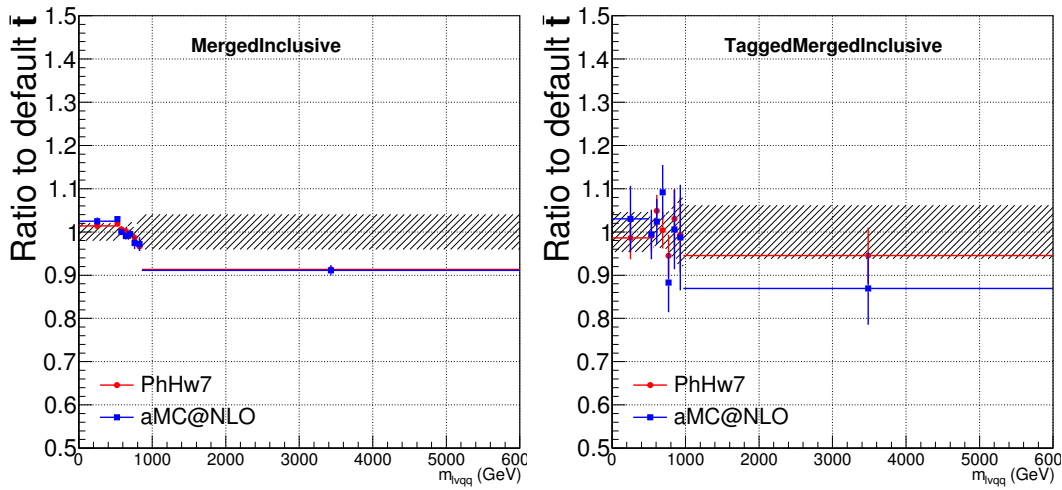


Figure 11.3: Ratio between the variations of generator (red) and hadronization (blue) variations for the Merged regime for $t\bar{t}$ sample.

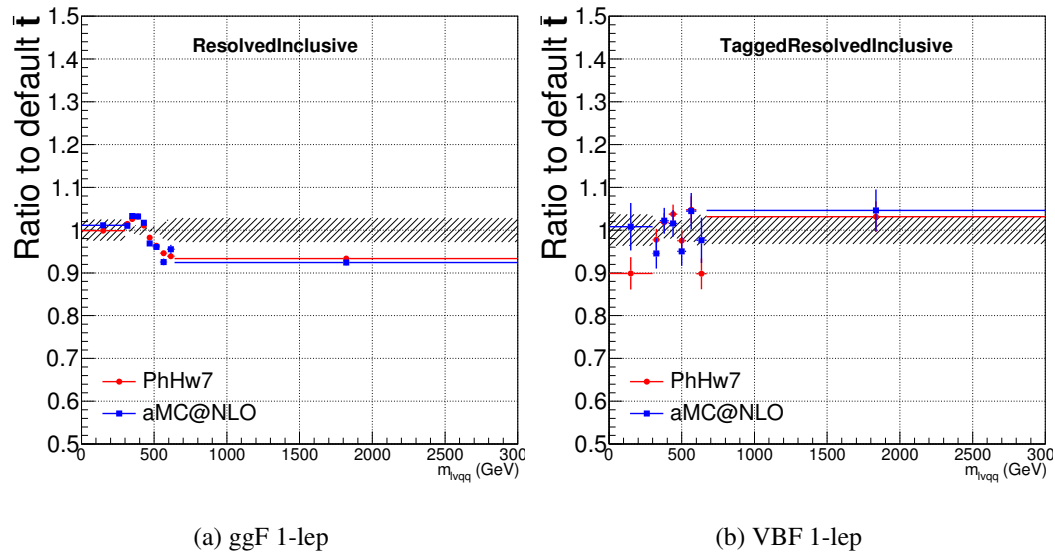


Figure 11.4: Ratio between the variations of generator (red) and hadronization (blue) variations for the Resolved regime for $t\bar{t}$ sample.

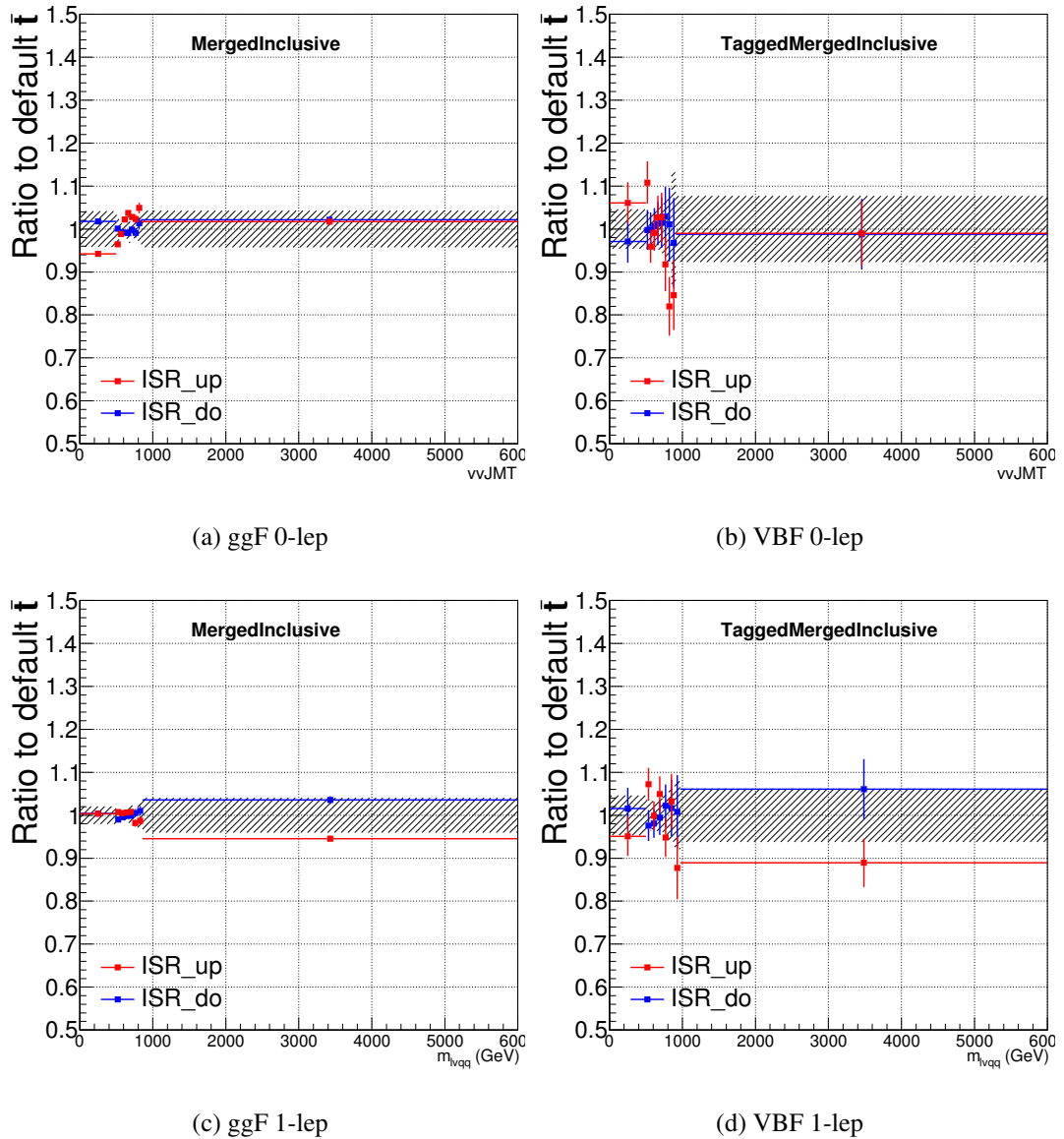


Figure 11.5: Ratio between the variations of ISR up (red) and down (blue) variations for the Merged regime for $t\bar{t}$ sample.

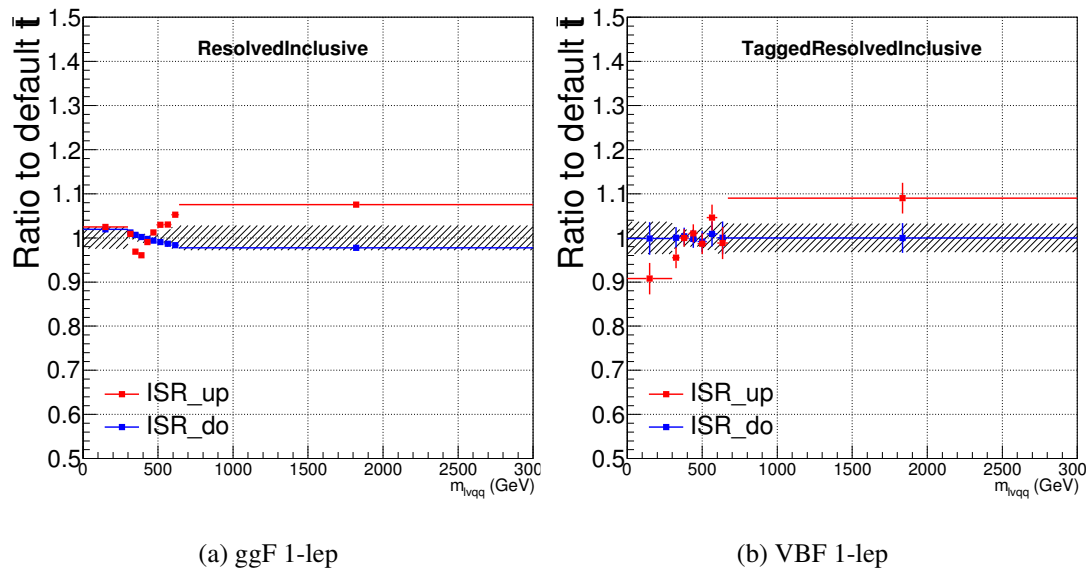


Figure 11.6: Ratio between the variations of ISR up (red) and down (blue) variations for the Resolved regime for $t\bar{t}$ sample.

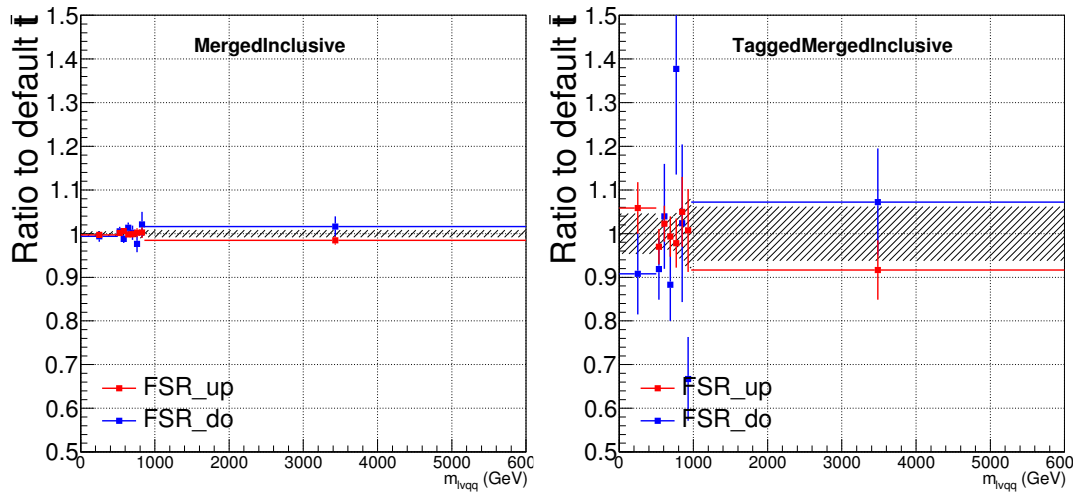


Figure 11.7: Ratio between the variations of FSR up (red) and down (blue) variations for the Merged regime for $t\bar{t}$ sample.

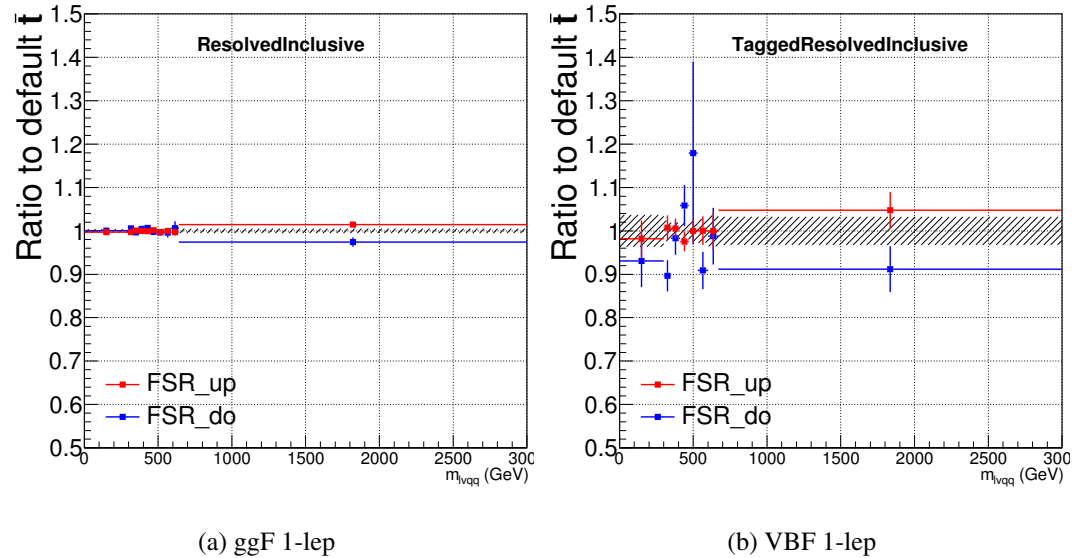


Figure 11.8: Ratio between the variations of FSR up (red) and down (blue) variations for the Resolved regime for $t\bar{t}$ sample.

Chapter 12

Statistical Analysis

A statistical procedure based on a likelihood function is used to determine the compatibility of the data collected with the proposed resonances. This test compares the distribution of m_{WV} for the background-only (which only considers SM processes, no new physics processes) hypothesis with the background and signal hypothesis (see Figures 13.3 - 13.7 for m_{WV} SR distributions). A discovery test is used to measure the compatibility of the observed data with the background-only hypothesis. If the observed data are sufficiently incompatible with the background only hypothesis, this could indicate a discovery. In the absence of discovery, upper limits on the signal strength parameter, μ , are assessed using the CLs method. These μ limits are then translated into upper limits on the allowed cross section of new physics processes.

For signal masses below 500 GeV only the resolved analysis is used, as the merged analysis is not applicable for such small resonance masses. Similarly, it is unlikely that the two jets from the hadronically decaying boson will be well separated for signal masses exceeding 1 TeV. Therefore, only the merged analysis is used above 1 TeV. For signal masses between 500 - 1000 GeV, the merged and resolved analyses are combined.

12.1 Likelihood Function

The likelihood function used is product of Poisson probabilities over all m_{WV} bins and the associated systematics:

$$\mathcal{L}(\mu, \boldsymbol{\theta}) = \prod_c \prod_i \frac{(\mu s_{ci}(\boldsymbol{\theta}) + b_{ci}(\boldsymbol{\theta}))^{n_{ci}}}{n_{ci}!} e^{-(\mu s_{ci}(\boldsymbol{\theta}) + b_{ci}(\boldsymbol{\theta}))} \prod_k (\theta'_k | \theta_k) \quad (12.1)$$

Here c are the analysis channels (e.g. merged SRs and CRs and resolved SRs and CRs) considered and i runs over all the m_{WV} bins used in the fit. The signal strength parameter, μ , multiplies the expected signal yield in each analysis bin, s_{ci} . The background content for channel c and bin i is given by b_{ci} . The dependence of signal and background predictions on systematic uncertainties is described by the aforementioned set of nuisance parameters $\boldsymbol{\theta}$, which are parameterized by Gaussian or log-normal priors, denoted here as θ_k . Statistical uncertainties of the simulated bin contents are also included as systematic uncertainties. Most systematics are correlated among all the analysis regions and considered to be independent from other systematics. The validity of this assumption is checked by evaluating the covariance of nuisance parameters.

12.2 Fit Configuration

The binning of m_{WV} in signal regions for the likelihood fit depends on the signal mass resolution and statistical uncertainties of m_{WV} bins. For each signal mass point, the signal mass resolution is set to the fitted Gaussian width in m_{WV} . The fitted signal widths are then fit to a line to give a parameterized signal mass width, as shown in Figures 12.1 and 12.2. Bin widths are set first to this parameterized signal mass resolution. Then if the statistical uncertainty of

the data or simulated background is more than 50% in any bin, bins are merged until the statistical uncertainty in all bins is less than 50%. All control regions contain only a single bin.

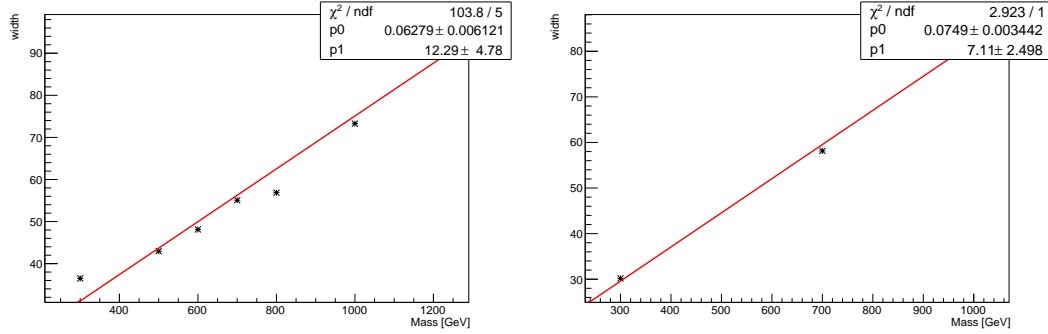


Figure 12.1: The HVT signal mass resolution as a function of mass fit with a straight line in the Resolved ggF region (left) and VBF (right) region.

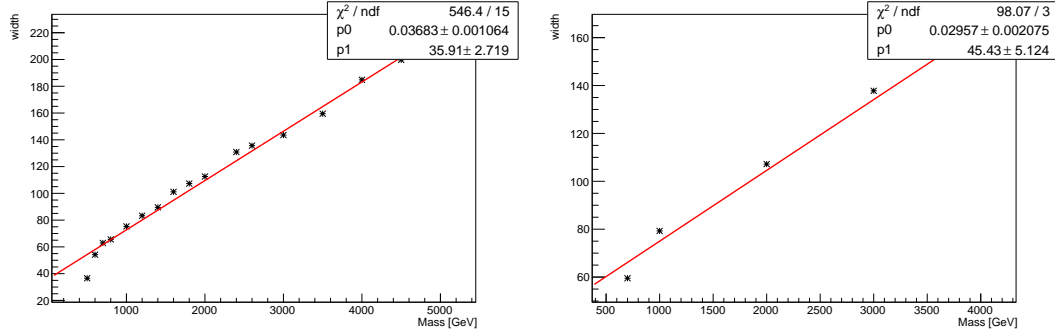


Figure 12.2: The HVT signal mass resolution as a function of mass fit with a straight line in the Merged ggF region (left) and VBF (right) region.

For each signal model is fit simultaneously in the merged and resolved channels. The $W+jets$ and $t\bar{t}$ normalizations are given by the best fit values in the overall fit and these fitted normalizations are then applied to those backgrounds in the SRs, as mentioned previously.

The m_{WW} distributions for a given systematic may contain unphysically large fluctuations due to m_{WW} bins with few events. This can lead to artificial pulls

and/or constraints in the fit. To remove such issues a multi-step smoothing procedure is applied to all systematic variation distributions. First, distributions are rebinned until the statistical error per bin is at least 5%. Next all local extrema are identified. The bins around smallest extrema are iteratively merged until only four local extrema remain. Then distributions are rebinned so that statistical uncertainties in each bin are < 5%.

For some systematics, up and down variations may be in the same direction with respect to the nominal distributions. This causes the variations to not cover the nominal choice, and the interpretation of the confidence interval is skewed as the nominal distribution should be bracketed by the up and down variations. This asymmetry may also lead to underconstrained systematics in the fit. To handle such asymmetric systematics, if the up and down variation for a given systematic are in the same direction for at least three m_{VV} bins, the variation is averaged for those bins. The averaging procedure replaces bin-by-bin the up and down variation bins by $b_{\pm}^{new} = b_{nom} \pm \frac{|b_+ - b_-|}{2}$, where b_{nom} is the nominal bin content and b_{\pm} are the original up and down variation bin content. The same procedure is also applied to any variations where the integral of the difference between the up/down variation and the nominal distribution is twice that of the other down/up variation, further ensuring variations are symmetric around the nominal distribution.

Finally, systematics that have a negligible effect on the m_{VV} distribution are not considered in the fit. Shape systematics where no bin in the variational distribution deviates more than 1% from the nominal distribution (after normalizing all histograms to the nominal) are not included in the fit. Also, statistical bin uncertainties < 1% are ignored.

12.3 Best Fit μ

The best-fit signal strength parameter is denoted by $\hat{\mu}$ and calculated by maximizing the likelihood function over the entire m_{WV} distribution with respect to all systematics and μ . The corresponding set of systematics that maximize the likelihood are given by $\hat{\theta}$. The first term in the likelihood is maximized when the expected number of signal and background events over all m_{WV} bins is equal to the number of events in data (per bin this means: $n_{ci} = \mu s_{ci} + b_{ci}$) . Thus, by maximizing the likelihood, the fit determines value of μ and θ that give the best agreement between expected and measured event yields. The second term in the likelihood is a penalty term which decreases the likelihood when systematics are shifted from their nominal values. This prevents the fit from profiling (unexpectedly constraining or shifting the fitted systematic value far from its nominal value) systematics in unphysical ways to maximize the likelihood. The uncertainty on μ is calculated by varying μ up and down until the natural log of the likelihood function shifts by one-half.

12.4 Discovery Test

To determine if the observed dataset is consistent with a given signal model a likelihood ratio is constructed:

$$\lambda(\mu) = \frac{\mathcal{L}(\mu, \hat{\theta}_\mu)}{\mathcal{L}(\hat{\mu}, \hat{\theta})} \quad (12.2)$$

The denominator in this equation is the maximized value of \mathcal{L} over all systematics and μ . The numerator is the maximized likelihood over all systematics for a given μ value, where the maximized systematics are given by $\hat{\theta}_\mu$. To test for the existence of signal the observed dataset the null hypothesis (H_0) is defined as

the background only hypothesis and the alternate hypothesis includes signal and background (H_1). This test quantifies the compatibility of observed data with H_0 by calculating a p-value representing the probability of observing data as discrepant or more than the observed data under the H_0 . The test statistic used to calculate this p-value is given by (r_0):

$$r_0 = \begin{cases} -2 \ln \lambda(0), \hat{\mu} > 0 \\ +2 \ln \lambda(0), \hat{\mu} < 0 \end{cases} \quad (12.3)$$

The expected distribution of the the test statistic under H_0 ($f(r_0|0)$) is used to calculate the p-value:

$$p_0 = \int_{r_0,obs}^{\infty} f(r_0|0) dr_0 \quad (12.4)$$

Small p-values indicate the observed data is poorly described by H_0 . This equivalent Z-score of a given p-value is usually used to further quantify the agreement between the observed data and H_0 . The Z-score is given by the number of standard deviations away from the mean of a Gaussian distribution, the integral of the upper tail of the distribution would equal the p-value. Mathematically:

$$Z = \Phi^{-1}(1 - p_0) \quad (12.5)$$

where Φ is the Gaussian cumulative distribution function. The statistical significance of these tests are expressed as the Z -score. In particle physics, 3σ is considered evidence for new phenomena and 5σ is the threshold for discovery.

12.5 Exclusion Limits

In the absence of discovery, upper limits on the signal strength, μ are set using the CLs method [44]. The test statistic for this test, q_μ , is constructed as:

$$\tilde{\lambda}_\mu = \begin{cases} \frac{\mathcal{L}(\mu, \hat{\theta}_\mu)}{\mathcal{L}(\hat{\mu}, \hat{\theta})}, \hat{\mu} > 0 \\ \frac{\mathcal{L}(\mu, \hat{\theta}_\mu)}{\mathcal{L}(0, \hat{\theta}_0)}, \hat{\mu} < 0 \end{cases} \quad (12.6)$$

$$\tilde{q}_\mu = \begin{cases} -2 \ln \tilde{\lambda}(\mu), \hat{\mu} < \mu \\ +2 \ln \tilde{\lambda}(\mu), \hat{\mu} > \mu \end{cases} \quad (12.7)$$

As defined, larger values of q_μ correspond to increasing incompatibility between the observed data and the background + signal hypothesis. The observed value of the test statistic, $q_{\mu,obs}$, is then compared to its expected distribution, f , to calculate p-values to assess the likelihood of the background+signal hypothesis. Using these distributions, CL_s values are computed as:

$$CL_{s+b} = \int_{q_{\mu,obs}}^{\infty} f(q_\mu | \mu) dq_\mu \quad (12.8)$$

$$CL_b = \int_{q_0^{obs}}^{\infty} f(q_\mu | \mu = 0) dq_\mu \quad (12.9)$$

$$CL_s = \frac{CL_{s+b}}{CL_b} \quad (12.10)$$

CL_{s+b} is the p-value for the signal + background hypothesis and CL_b is the p-value for the background only hypothesis. The CL_s value is interpreted as the probability to observe the background + signal hypothesis normalized to the probability of background-only hypothesis. Normalizing by CL_b prevents setting artificially strong exclusion limits due to downward fluctuations in data.

For a given signal hypothesis, μ values are scanned simultaneously over all

m_{WV} bins to find the μ value that yields $CL_s=0.05$, meaning the likelihood of finding data more incompatible with the background + signal hypothesis (relative to the background only hypothesis) is 5%. The 95% upper limit on the signal cross section is then calculated as the product of $\hat{\mu}$, BR, and theory cross section.

Chapter 13

Results

13.1 Expected and Measured Yields

The yield tables for the four analysis regions are shown in Tables 13.1 - 13.5. The fitted background normalizations are shown in Tables 13.6-13.9. The control region $m_{\ell\nu qq}$ distributions are shown in Figures 13.1 - 13.2. The signal region $m_{\ell\nu qq}$ distributions are shown in Figures 13.3 - 13.7.

	HP WCR	LP WCR	Resolved WCR
Electron Multi-jet	-	-	16500 ± 2300
Muon Multi-jet	-	-	20000 ± 2800
Diboson	1800 ± 180	3300 ± 320	9100 ± 960
Single-top	2200 ± 400	3500 ± 660	20000 ± 3800
$t\bar{t}$	16000 ± 340	24000 ± 450	140000 ± 2000
$W+jets$	40000 ± 360	88113.06 ± 490	670000 ± 4100
$Z+jets$	780 ± 79	1800 ± 180	17000 ± 1700
Total	60000 ± 660	120000 ± 1000	890000 ± 7200
Data	60264	120852	895362
	HP TCR	LP TCR	Resolved TCR
Electron Multi-jet	-	-	-
Muon Multi-jet	-	-	-
Diboson	420 ± 38	550 ± 53	1000 ± 120
Single-top	4700 ± 850	3500 ± 630	17000 ± 3300
$t\bar{t}$	39000 ± 850	34000 ± 640	220000 ± 3200
$W+jets$	2300 ± 20	6600 ± 36	23000 ± 140
$Z+jets$	66 ± 7	210 ± 21	850 ± 85
Total	46000 ± 1200	45000 ± 900	270000 ± 4600
Data	46354	44629	266443
	WW SR	LP SR	Resolved 1-lepton SR
Electron Multi-jet	-	-	11000 ± 1500
Muon Multi-jet	-	-	16000 ± 2200
Diboson	5000 ± 400	3900 ± 310	17000 ± 1500
Single-top	3000 ± 600	2000 ± 400	20000 ± 4000
$t\bar{t}$	14000 ± 300	11000 ± 210	130000 ± 1800
$W+jets$	25000 ± 220	60080.66 ± 330	440000 ± 2700
$Z+jets$	500 ± 50	1200 ± 120	12000 ± 1200
Total	47000 ± 780	78000 ± 650	650000 ± 6000
Data	47330	78380	645610

Table 13.1: Expected and Measured for DY WW $W+jets$, $t\bar{t}$ control regions and signal regions.

	HP Untagged WCR	LP Untagged WCR	Resolved Untagged WCR
Electron Multi-jet	-	-	15000 ± 2300
Muon Multi-jet	-	-	27000 ± 3000
Diboson	1500 ± 150	2800 ± 280	9000 ± 730
Single-top	1800 ± 310	2900 ± 520	21000 ± 3500
$t\bar{t}$	13000 ± 240	22000 ± 330	140000 ± 2600
$W+jets$	41000 ± 330	88000 ± 500	670000 ± 4400
$Z+jets$	770 ± 78	1800 ± 180	17000 ± 1700
Total	58000 ± 540	120000 ± 860	890000 ± 7500
Data	57699	117306	895362
	HP Tagged WCR	LP Tagged WCR	Resolved Tagged WCR
Electron Multi-jet	-	-	400 ± 60
Muon Multi-jet	-	-	600 ± 190
Diboson	30 ± 5	50 ± 80	260 ± 28
Single-top	300 ± 60	400 ± 70	5800 ± 1000
$t\bar{t}$	2000 ± 50	2041.48 ± 70	58000 ± 600
$W+jets$	600 ± 80	1100 ± 90	12000 ± 900
$Z+jets$	13 ± 1	23 ± 2	320 ± 33
Total	2600 ± 100	3600 ± 130	78000 ± 1500
Data	2565	3546	77973
	HP Untagged TCR	LP Untagged TCR	Resolved Untagged TCR
Electron Multi-jet	-	-	-
Muon Multi-jet	-	-	-
Diboson	290 ± 28	350 ± 36	700 ± 70
Single-top	3100 ± 540	2300 ± 390	9600 ± 1700
$t\bar{t}$	31000 ± 560	30000 ± 400	92000 ± 1700
$W+jets$	2200 ± 18	4900 ± 28	16000 ± 110
$Z+jets$	70 ± 7	160 ± 16	580 ± 60
Total	37000 ± 780	35000 ± 570	120000 ± 2400
Data	36677	34573	118928
	HP Tagged TCR	LP Tagged TCR	Resolved Tagged TCR
Electron Multi-jet	-	-	-
Muon Multi-jet	-	-	-
Diboson	10 ± 1	9 ± 1	30 ± 5
Single-top	110 ± 21	120 ± 23	660 ± 130
$t\bar{t}$	2000 ± 50	1500 ± 47	18000 ± 190
$W+jets$	30 ± 4	90 ± 7	490 ± 37
$Z+jets$	1 ± 1	2 ± 1	19 ± 2
Total	2100 ± 50	1700 ± 50	19000 ± 230
Data	2047	1708	19143

Table 13.2: Expected and Measured for DY WZ $W+jets$, $t\bar{t}$ tag and untag control regions.

	HP Untagged SR	LP Untagged SR	Resolved Untagged SR
Electron Multi-jet	-	-	7800 ± 1200
Muon Multi-jet	-	-	17004.81 ± 1834.40
Diboson	3000 ± 270	2300 ± 210	15000 ± 1200
Single-top	2100 ± 370	1400 ± 240	18000 ± 3100
$t\bar{t}$	12000 ± 210	8900 ± 140	110000 ± 2100
$W+jets$	23000 ± 190	42000 ± 240	340000 ± 2300
$Z+jets$	400 ± 40	800 ± 90	10000 ± 1000
Total	40000 ± 550	55000 ± 430	520000 ± 5100
Data	40193	54735	521813
	HP Tagged SR	LP Tagged SR	Resolved Tagged SR
Electron Multi-jet	-	-	200 ± 30
Muon Multi-jet	-	-	393.43 ± 124.06
Diboson	100 ± 12	65 ± 8	620 ± 58
Single-top	180 ± 34	160 ± 29	3500 ± 620
$t\bar{t}$	1000 ± 32	710 ± 26	38000 ± 4000
$W+jets$	300 ± 40	580 ± 40	6000 ± 500
$Z+jets$	8 ± 1	12 ± 1	180 ± 19
Total	2000 ± 60	2000 ± 60	50000 ± 900
Data	1699	1559	48919

Table 13.3: Expected and Measured for DY WZ $W+jets$, $t\bar{t}$ tag and untag signal regions.

	HP WCR	LP WCR	Resolved WCR
Electron Multi-jet	-	-	900 ± 140
Muon Multi-jet	-	-	601.46 ± 182.74
Diboson	100 ± 45	170 ± 68	290 ± 240
Single-top	78 ± 18	130 ± 32	880 ± 220
$t\bar{t}$	400 ± 28	570 ± 49	5100 ± 160
$W+jets$	900 ± 60	1900 ± 90	19000 ± 400
$Z+jets$	20 ± 2	47 ± 5	800 ± 80
Total	2000 ± 80	2900 ± 130	27000 ± 60
Data	1495	2898	27120
	HP TCR	LP TCR	Resolved TCR
Electron Multi-jet	-	-	-
Muon Multi-jet	-	-	-
Diboson	10 ± 7	28 ± 14	24 ± 20
Single-top	68 ± 16	59 ± 14	300 ± 70
$t\bar{t}$	500 ± 30	400 ± 32	3800 ± 100
$W+jets$	51 ± 4	140 ± 8	450 ± 12
$Z+jets$	1 ± 1	5 ± 1	30 ± 3
Total	600 ± 40	637.10 ± 40	5000 ± 130
Data	636	634	4615
	HP SR	LP SR	Resolved SR
Electron Multi-jet	-	-	600 ± 90
Muon Multi-jet	-	-	481.01 ± 144.48
Diboson	150 ± 49	180 ± 67	400 ± 320
Single-top	80 ± 20	57 ± 15	780 ± 190
$t\bar{t}$	340 ± 24	240 ± 21	4300 ± 140
$W+jets$	500 ± 40	1300 ± 65	11000 ± 290
$Z+jets$	9 ± 1	29 ± 3	570 ± 58
Total	1000 ± 70	2000 ± 100	20000 ± 500
Data	1096	1846	18530

Table 13.4: Expected and Measured for VBF WW $W+jets$, $t\bar{t}$ control regions and signal regions.

	HP WCR	LP WCR	Resolved WCR
Electron Multi-jet	-	-	870 ± 130
Muon Multi-jet	-	-	620 ± 200
Diboson	93 ± 42	150 ± 64	230 ± 110
Single-top	71 ± 16	120 ± 28	1200 ± 280
$t\bar{t}$	430 ± 30	500 ± 50	6900 ± 250
$W+jets$	870 ± 64	2000 ± 94	19000 ± 440
$Z+jets$	20 ± 2	47 ± 5	800 ± 80
Total	1500 ± 84	2800 ± 130	30000 ± 600
Data	1495	2898	29755

	HP TCR	LP TCR	Resolved TCR
Electron Multi-jet	-	-	-
Muon Multi-jet	-	-	-
Diboson	10 ± 5	13 ± 7	14 ± 7
Single-top	52 ± 12	35 ± 8	170 ± 45
$t\bar{t}$	470 ± 29	300 ± 25	2400 ± 75
$W+jets$	50 ± 4	110 ± 6	380 ± 12
$Z+jets$	1 ± 1	5 ± 1	18 ± 2
Total	580 ± 32	460 ± 28	3000 ± 90
Data	584	459	3001

	HP SR	LP SR	Resolved SR
Electron Multi-jet	-	-	400 ± 70
Muon Multi-jet	-	-	400 ± 130
Diboson	100 ± 40	110 ± 46	270 ± 140
Single-top	63 ± 15	48 ± 12	870 ± 210
$t\bar{t}$	350 ± 24	190 ± 18	5100 ± 190
$W+jets$	500 ± 40	1000 ± 50	10000 ± 250
$Z+jets$	8 ± 1	24 ± 2	560 ± 57
Total	1000 ± 60	1000 ± 70	20000 ± 400
Data	1018	1313	17826

Table 13.5: Expected and Measured for VBF WZ $W+jets$, $t\bar{t}$ control regions and signal regions.

Background	Fitted Normalization
XS_Top_LP_lvqq_Merg_binned	$0.91^{+0.017}_{-0.017}$
XS_Top_Merg	$0.94^{+0.020}_{-0.020}$
XS_Top_Res	$0.96^{+0.013}_{-0.013}$
XS_Wjets_LP_lvqq_Merg_binned	$0.88^{+0.0049}_{-0.0049}$
XS_Wjets_Merg	$0.9^{+0.008}_{-0.008}$
XS_Wjets_Res	$1.0^{+0.006}_{-0.006}$

Table 13.6: Fitted background normalizations for $t\bar{t}$ and $W+jets$ backgrounds for the DY WW analysis region.

Background	Fitted Normalization
XS_Top_LP_Tag_lvqq_Merg_binned	$0.97^{+0.033}_{-0.033}$
XS_Top_LP_lvqq_Merg_binned	$0.89^{+0.014}_{-0.014}$
XS_Top_Merg	$0.89^{+0.016}_{-0.016}$
XS_Top_Res	$0.97^{+0.018}_{-0.018}$
XS_Top_Tag_lvqq_Merg_binned	$0.95^{+0.028}_{-0.028}$
XS_Top_Tag_lvqq_Res_binned	$0.99^{+0.011}_{-0.011}$
XS_Wjets_LP_Tag_lvqq_Merg_binned	$0.91^{+0.070}_{-0.070}$
XS_Wjets_LP_lvqq_Merg_binned	$0.88^{+0.0050}_{-0.0050}$
XS_Wjets_Merg	$0.95^{+0.008}_{-0.008}$
XS_Wjets_Res	$1.0^{+0.007}_{-0.007}$
XS_Wjets_Tag_lvqq_Merg_binned	$0.91^{+0.12}_{-0.12}$
XS_Wjets_Tag_lvqq_Res_binned	$1.2^{+0.090}_{-0.090}$

Table 13.7: Fitted background normalizations for $t\bar{t}$ and $W+jets$ backgrounds for the DY WZ analysis region.

Background	Fitted Normalization
XS_Top_LP_lvqq_Merg_binned	$0.79^{+0.067}_{-0.067}$
XS_Top_Merg	$0.89^{+0.061}_{-0.061}$
XS_Top_Res	$1.0^{+0.031}_{-0.031}$
XS_Wjets_LP_lvqq_Merg_binned	$0.88^{+0.042}_{-0.042}$
XS_Wjets_Merg	$0.881^{+0.068}_{-0.068}$
XS_Wjets_Res	$0.93^{+0.020}_{-0.020}$

Table 13.8: Fitted background normalizations for $t\bar{t}$ and $W+jets$ backgrounds for the VBF WW analysis region.

Background	Fitted Normalization
XS_Top_LP_lvqq_Merg_binned	$0.71^{+0.064}_{-0.064}$
XS_Top_Merg	$0.96^{+0.064}_{-0.064}$
XS_Top_Res	$1.0^{+0.04}_{-0.04}$
XS_Wjets_LP_lvqq_Merg_binned	$0.9^{+0.044}_{-0.044}$
XS_Wjets_Merg	$0.88^{+0.069}_{-0.069}$
XS_Wjets_Res	$0.95^{+0.022}_{-0.022}$

Table 13.9: Fitted background normalizations for $t\bar{t}$ and $W+jets$ backgrounds for the VBF WZ analysis region.

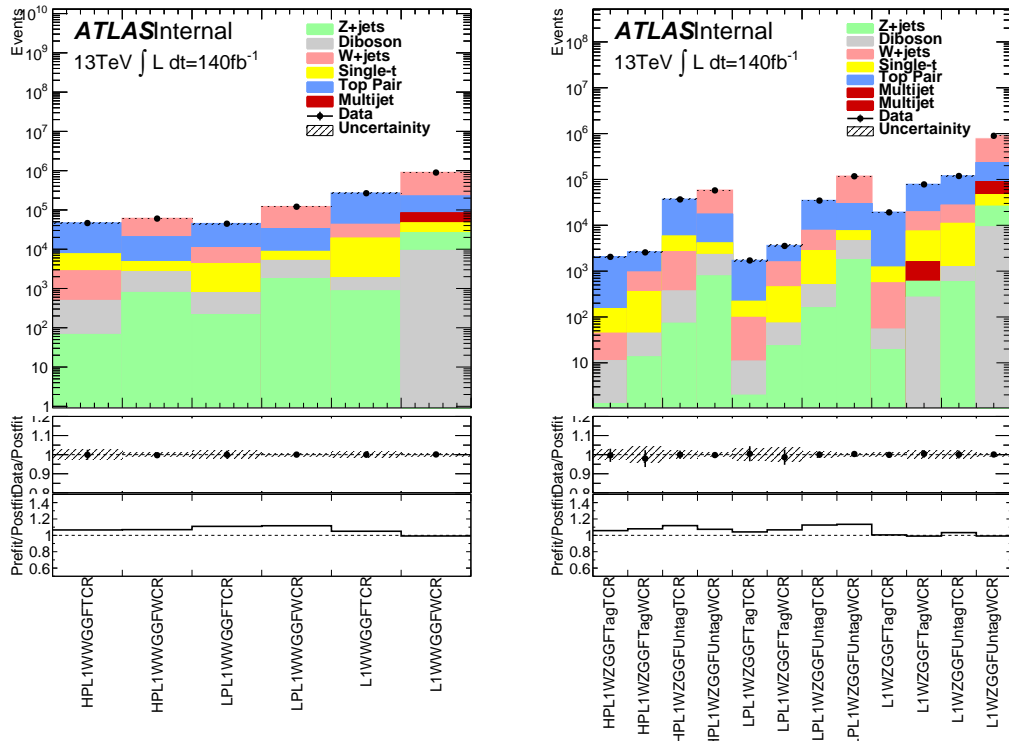


Figure 13.1: The distribution of $m_{l\nu qq}$ in the DY $WW(WZ)$ control regions on the left(right).

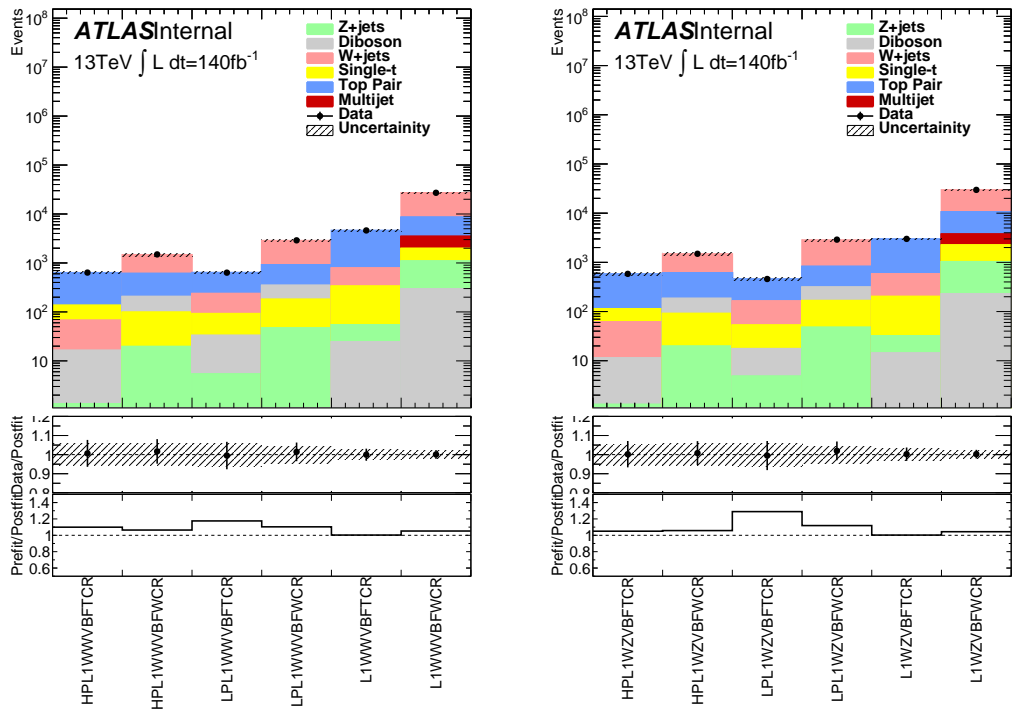


Figure 13.2: The distribution of $m_{\ell\nu qq}$ in the VBF $WW(WZ)$ control regions.

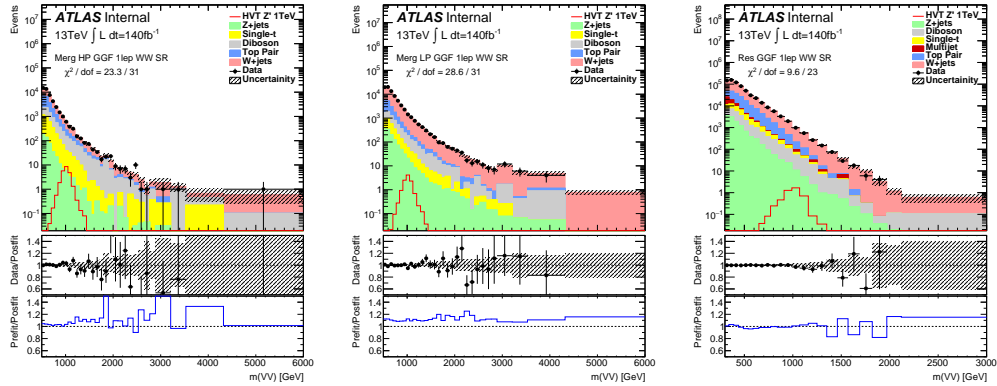


Figure 13.3: The distribution of $m_{\ell\nu qq}$ in the GGF WW signal regions.

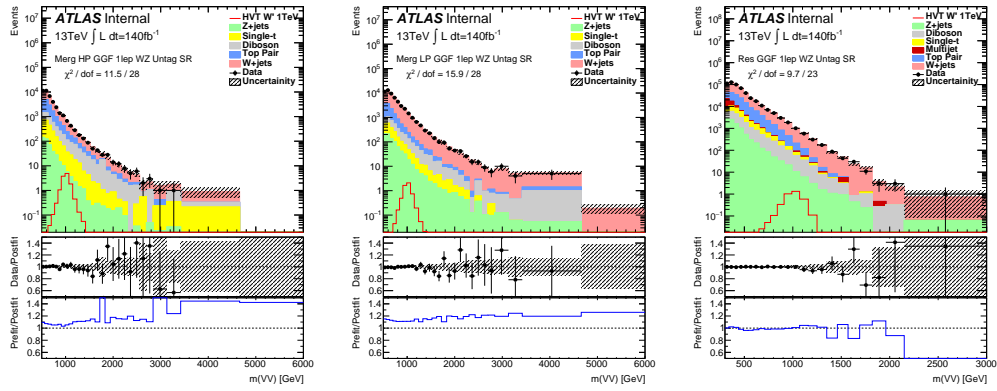


Figure 13.4: The distribution of $m_{\ell\nu qq}$ in the GGF WZ Untag signal regions.

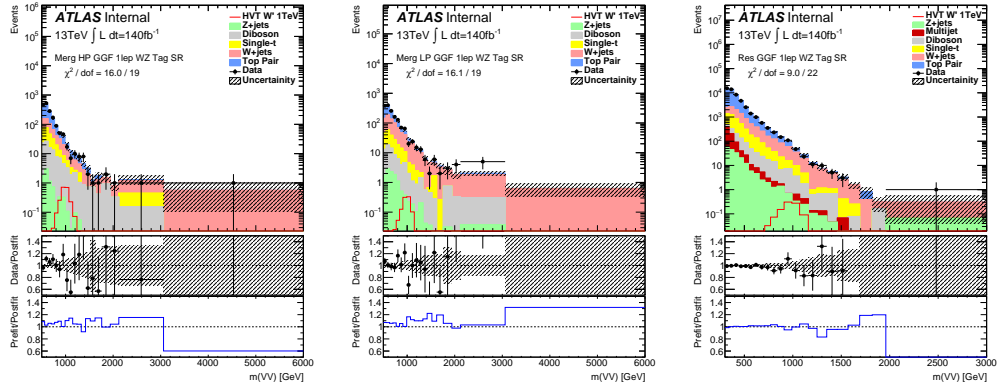


Figure 13.5: The distribution of $m_{\ell\nu qq}$ in the GGF WZ Tag signal regions.

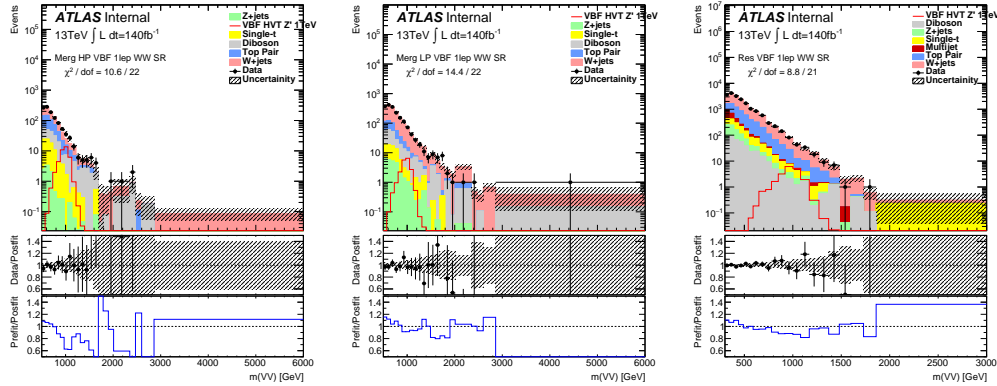


Figure 13.6: The distribution of $m_{\ell\nu qq}$ in the VBF WW Tag signal regions.

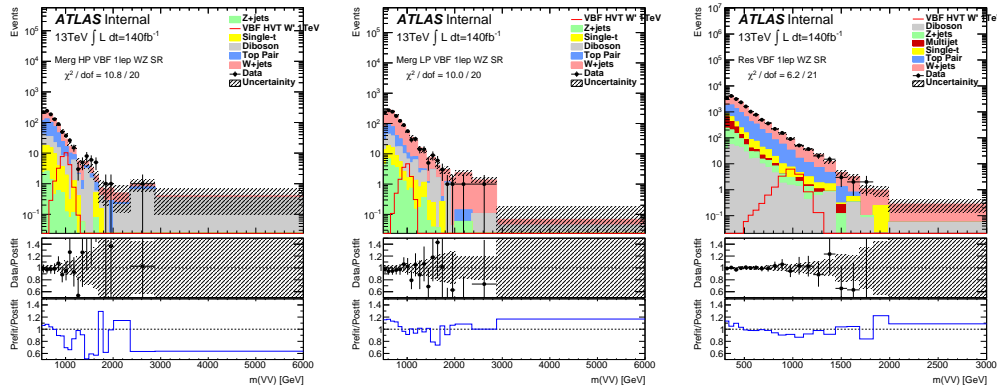


Figure 13.7: The distribution of $m_{\ell\nu qq}$ in the VBF WZ Tag signal regions.

13.2 Systematic Profiling and Correlations

The ranked systematics, in terms of their impact on $\hat{\mu}$, and their fitted values are shown for the different analysis regions in Figure 13.8 and 13.9. Note that background normalizations for $W+jets$ and $t\bar{t}$ are left free to float in the fit. This means the nominal normalization values are one and the uncertainties are not shown in the ranked plots. Overall, systematics are not pulled outside their uncertainties, especially nuisance parameters that affect $\hat{\mu}$ most significantly.

The correlation between systematics are shown in Figure 13.10. Correlations

between background normalization are expected. The remaining systematic correlations are not very strong or unexpected.

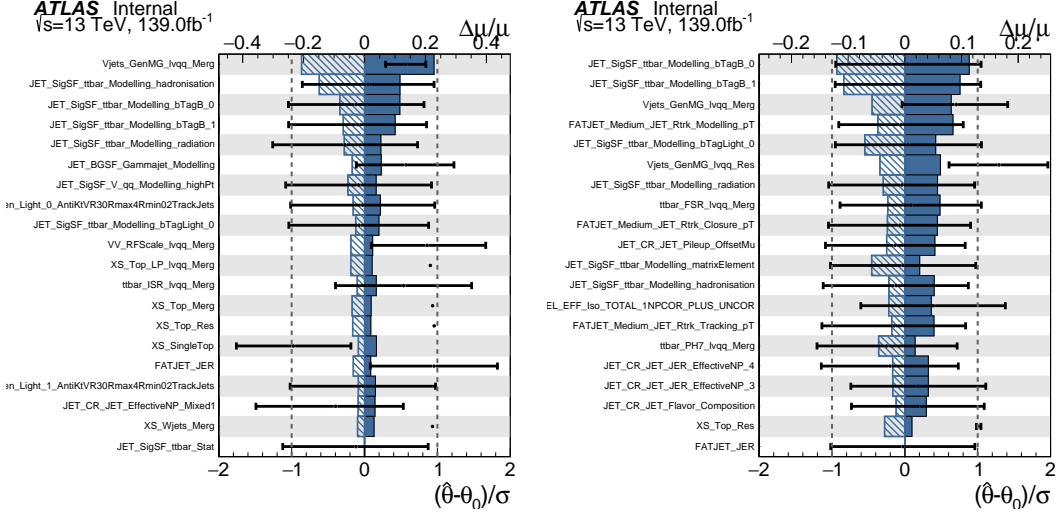


Figure 13.8: Ranked systematics and their fitted values for WW DY (right) and VBF (left) selections.

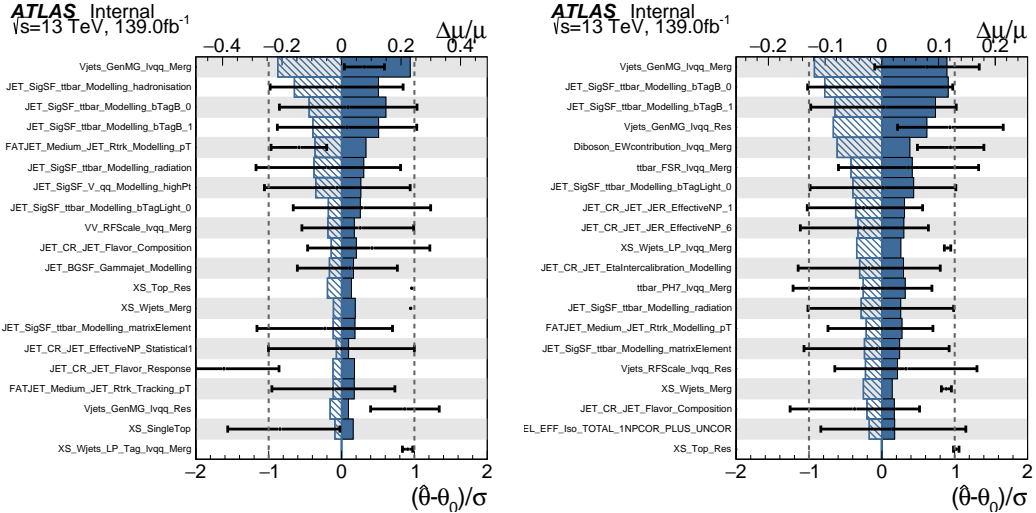


Figure 13.9: Ranked systematics and their fitted values for WZ DY (right) and VBF (left) selections.

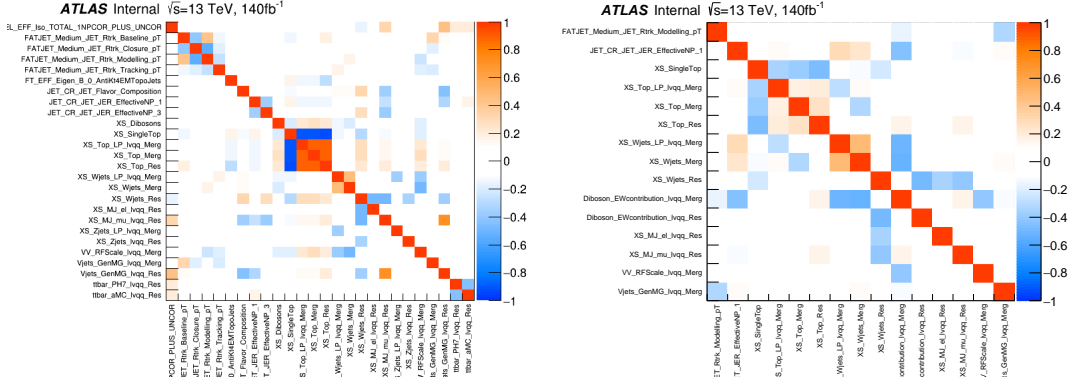


Figure 13.10: Correlations between systematics for WW DY (right) and VBF (left) selections.

13.3 Discovery Tests

To test for the existence of signal in the observed dataset, the discovery tests discussed earlier are used to calculate p -values as a function of resonance mass. The results of these tests are shown in Figures 13.11 - 13.13. The largest non-VBF excesses are 2.2σ at 600 GeV and 1.8σ at 2 TeV for HVT Z' . The largest VBF excess is 2.6σ for HVT Z' 1 TeV resonance.

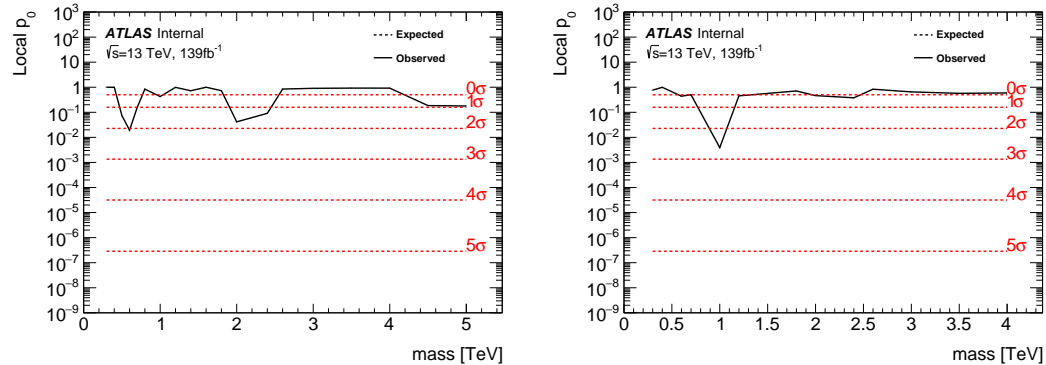


Figure 13.11: These plots show the measured p_0 value as a function of resonance mass for HVT Z' DY(VBF) production, left(right).

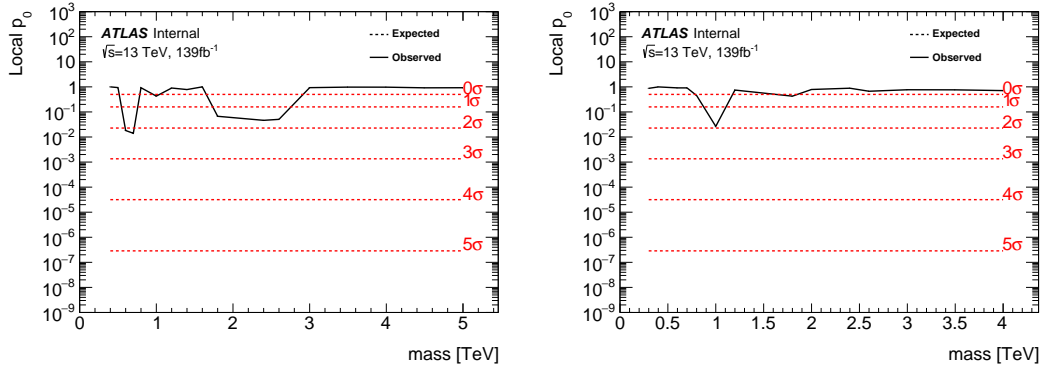


Figure 13.12: These plots show the measured p_0 value as a function of resonance mass for HVT W' DY(VBF) production, left(right).

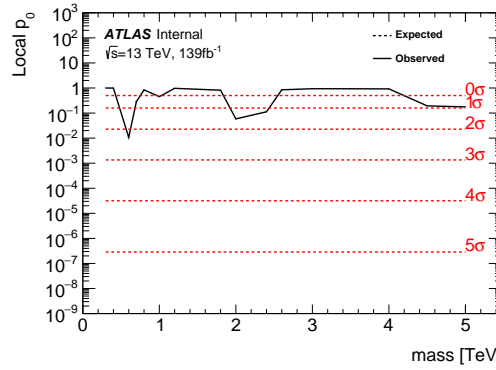


Figure 13.13: These plots show the measured p_0 value as a function of resonance mass for the RS Graviton DY production.

13.4 Limits

As the deviations from the background only hypothesis do not constitute discoveries from 13.3, upper limits on μ are calculated. Using the exclusion limits tests discussed previously, exclusion limits are set on μ and consequently signal cross-sections. Exclusion limits for the models considered are shown in Figure 13.14 - 13.16. These plots show the theory cross section for a given resonance to decay to WW/WZ . An Asimov dataset is used to expected calculate the lim-

its (assuming no new physics contributions) with the associated errors, shown as the black dashed lines with the green and yellow error bands. Finally, the observed limits are shown in black. All signal masses where the theory prediction is less than the observed prediction are excluded. These limits shown exclude HVT Model A $W' < 3.4$ TeV and $Z' < 3.3$ TeV and Model B $W' < 3.7$ TeV and $Z' < 3.7$ TeV. RS Gravitons are excluded for masses below 1.6 TeV .

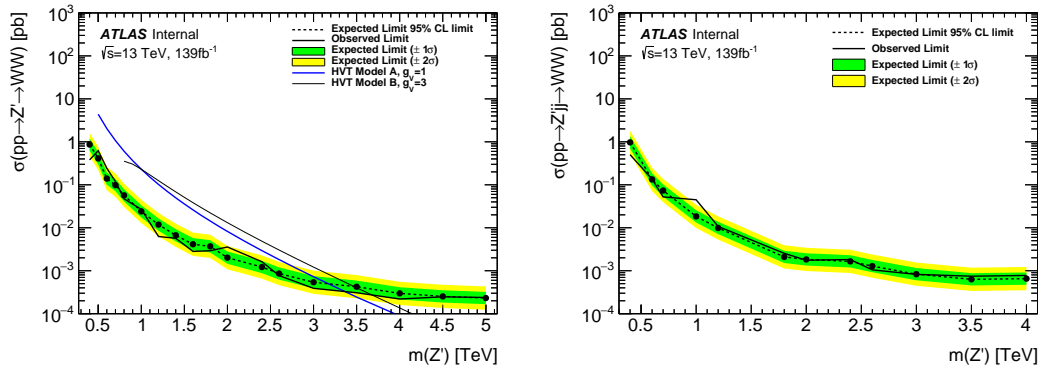


Figure 13.14: Theory, expected and observed limits for HVT W' DY (left) and VBF (right) production.

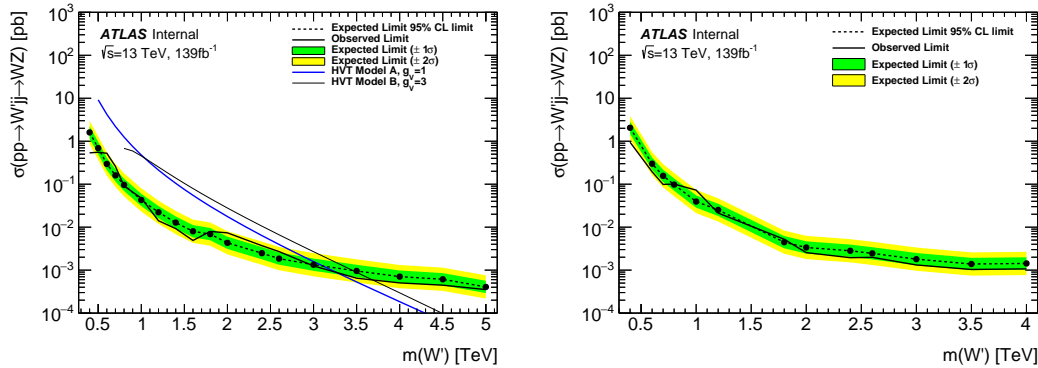


Figure 13.15: Theory, expected and observed limits for HVT Z' DY (left) and VBF (right) production.

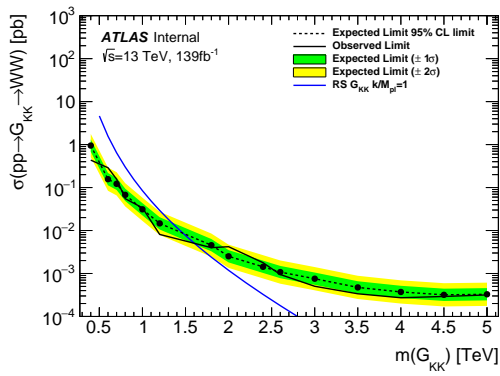


Figure 13.16: Theory, expected and observed limits for RS Gravitons via gluon-gluon fusion production.

Part V

Quark and Gluon Tagging

Chapter 14

Quark Gluon Tagging in $\ell\nu qq$

Diboson Resonance Search

The jets produced in diboson resonances in $\ell\nu qq$ final states below ~ 700 GeV are well separated and may be reconstructed separately. The background jets of this diboson resonance search are gluon dominated, while signal jets are quark enriched. By classifying jets in events as quark or gluon initiated, background contamination in the signal region may be reduced.

Figure 14.1 shows the flavor distributions of the truth parton matched to the jet (meaning the highest energy parton in the jet catchment area) in events passing the resolved signal region selections. From this Figure, it is evident that a notable fraction of the background (all background events that passed the resolved SR are used) that contaminates the signal region contains gluon jets, especially for the sub-leading jet.

As gluons jets have more constituents and therefore more tracks (n_{trk}), background jets generally have more tracks than the signal jets. This is shown in Figure 14.2. Therefore n_{trk} , provides discrimination between quark and gluon jets (i.e. jets with less than a specified n_{trk} value could be classified as a quark-

initiated jet, otherwise the jet would be classified as gluon-initiated.). Moreover, as the momentum of the jet increases the number of tracks also increases logarithmically and improves tagging efficiency by about 10% relative to a constant cut on the number of tracks [39]. Figures 14.3-14.6 show normalized heat maps of $\ln(p_T)$ vs n_{trk} for the background and HVT Z' signals. This information is also shown in table 14.1. In these plots it is evident that n_{trk} in the background jets grows more quickly with $\ln(p_T)$ than for the signal jets. This is expected given that the signal is quark dominated and the background is gluon dominated.

In Figure 14.7 is the ROC Curve for quark gluon tagging with cut on n_{trk} in a jet that depends on $\ln(p_T)$. Here the quark tagging efficiency is the ratio of quarks tagged as quarks to the total number of quarks in the signal region. The gluon rejection is calculated as the reciprocal of the gluon tagging efficiency. For example, choosing a 90% efficient working point with a rejection of 1.4 corresponds to a slope of 4 and intercept of -5. Tagging both jets in this analysis would yield an efficiency of 81%. Focusing on the background in Figure 14.8, this cut helps minimize gluon contamination in the signal region.

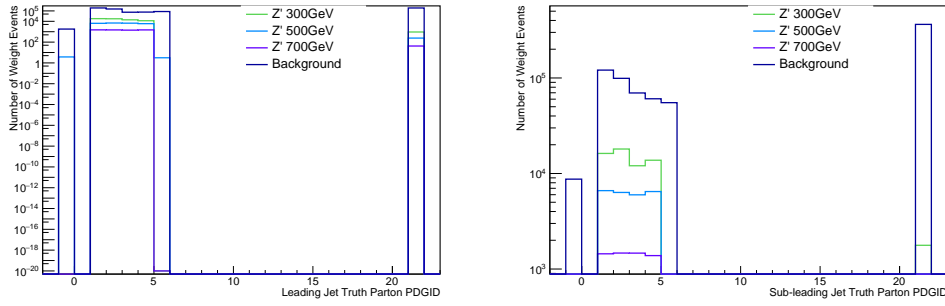


Figure 14.1: PDGID of the truth-level parton matched to the small-R jets passing the Resolved GGF WW Signal Region selections for the (a) Leading (b) Sub-Leading jets . These distributions are shown for 300, 500, and 700GeV Z' signals and the background (all simulated backgrounds that pass SR selections). PDGID = -1 corresponds to pileup jets, $0 < \text{PDGID} < 6$ correspond to quarks and PDGID = 21 corresponds to gluons.

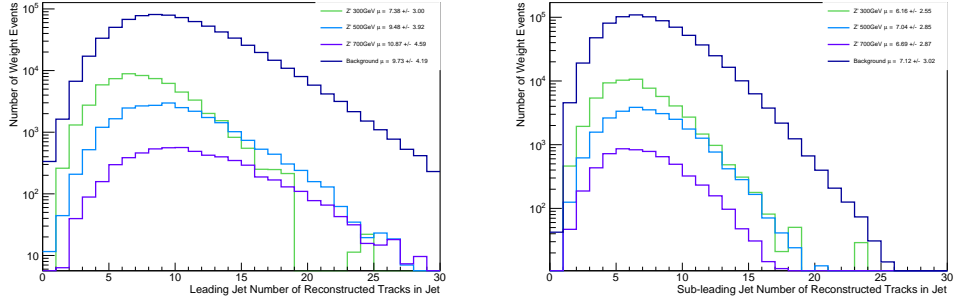


Figure 14.2: The number of tracks in small-R jets in events passing the Resolved GGF WW Signal Region selections for the (a) Leading (b) Sub-Leading jets. These distributions are shown for 300, 500, and 700GeV Z' signals and the background.

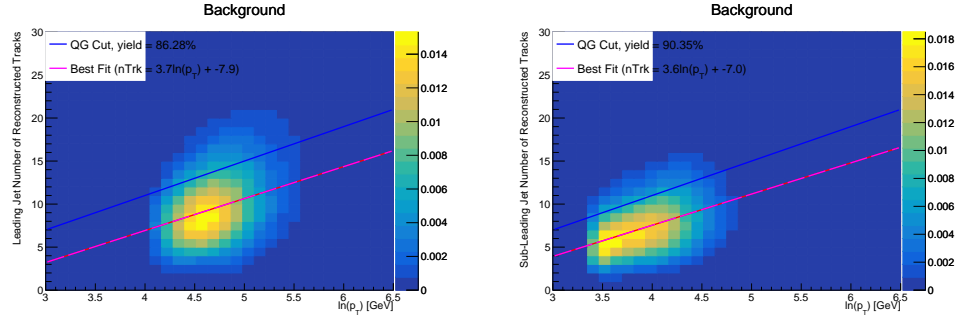


Figure 14.3: The number of tracks in background small-R jets in events passing the Resolved GGF WW Signal region selection vs. $\ln(p_T)$ for (a)Leading (b) Sub-Leading jets. The best fit line for the distribution is also shown, as well as the percentage of jets that pass a cut of number of tracks $< 4 \times \ln(p_T) - 5$. Note the number of total entries in these plots has been normalized to one.

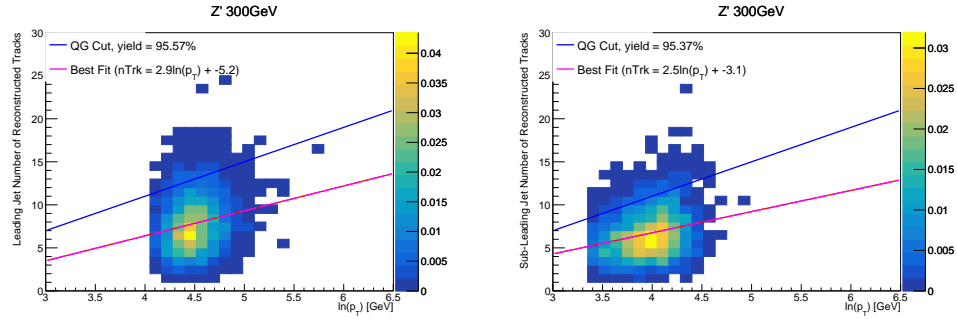


Figure 14.4: The number of tracks in small-R jets in 300GeV Z' events passing the Resolved GGF WW Signal region selection vs. $\ln(p_T)$ for (a)Leading (b) Sub-Leading jets. The best fit line for the distribution is also shown, as well as the percentage of jets that pass a cut of number of tracks $< 4 \times \ln(p_T) - 5$. Note the number of total entries in these plots has been normalized to one.

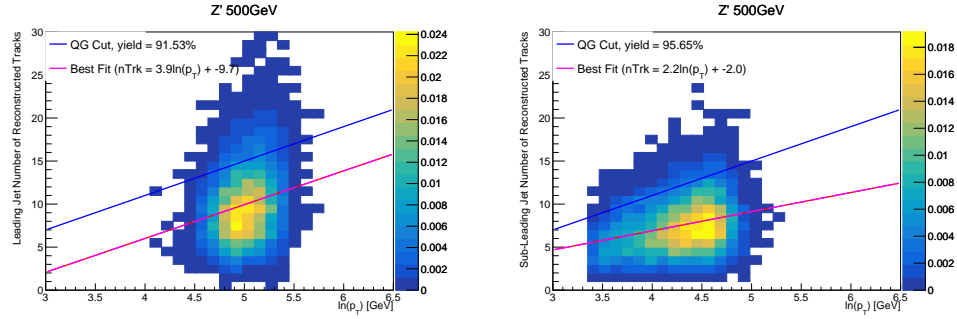


Figure 14.5: The number of tracks in small-R jets in 500GeV Z' events passing the Resolved GGF WW Signal region selection vs. $\ln(p_T)$ for (a)Leading (b) Sub-Leading jets. The best fit line for the distribution is also shown, as well as the percentage of jets that pass a cut of number of tracks $< 4 \times \ln(p_T) - 5$. Note the number of total entries in these plots has been normalized to one.

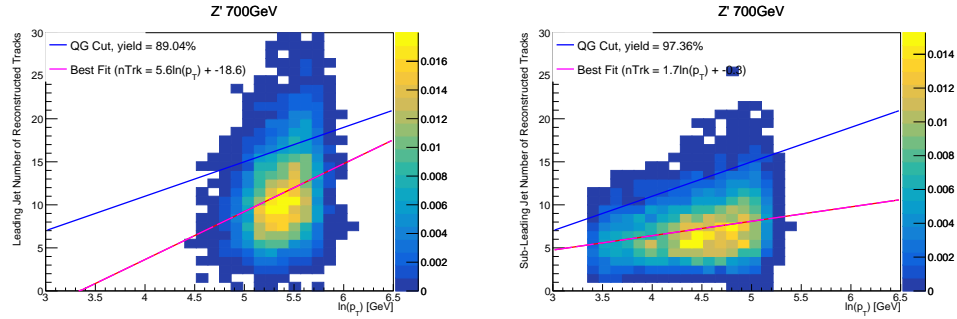


Figure 14.6: The number of tracks in small-R jets in 700GeV Z' events passing the Resolved GGF WW Signal region selection vs. $\ln(p_T)$ for (a)Leading (b) Sub-Leading jets. The best fit line for the distribution is also shown, as well as the percentage of jets that pass a cut of number of tracks $< 4 \times \ln(p_T) - 5$. Note the number of total entries in these plots has been normalized to one.

Sample	Best Fit Slope	Best Fit Intercept	QG Tag Yield
Backgrounds	3.7	-7.9	86%
HVT Z' 300 GeV	2.9	-5.2	95%
HVT Z' 500 GeV	3.9	-9.7	92%

Table 14.1: This table shows the best fit slope and intercept for the 2-d distribution of n_{trk} vs. jet $\ln(p_T)$ for the leading jet in the background and HVT Z' samples. The tagging efficiency is shown for the 90% working point in the last column. The background jets contain more gluons than the signal jets. Consequently, the best fit line for the background predicts larger values of the number of tracks in jets for the background than the considered signals.

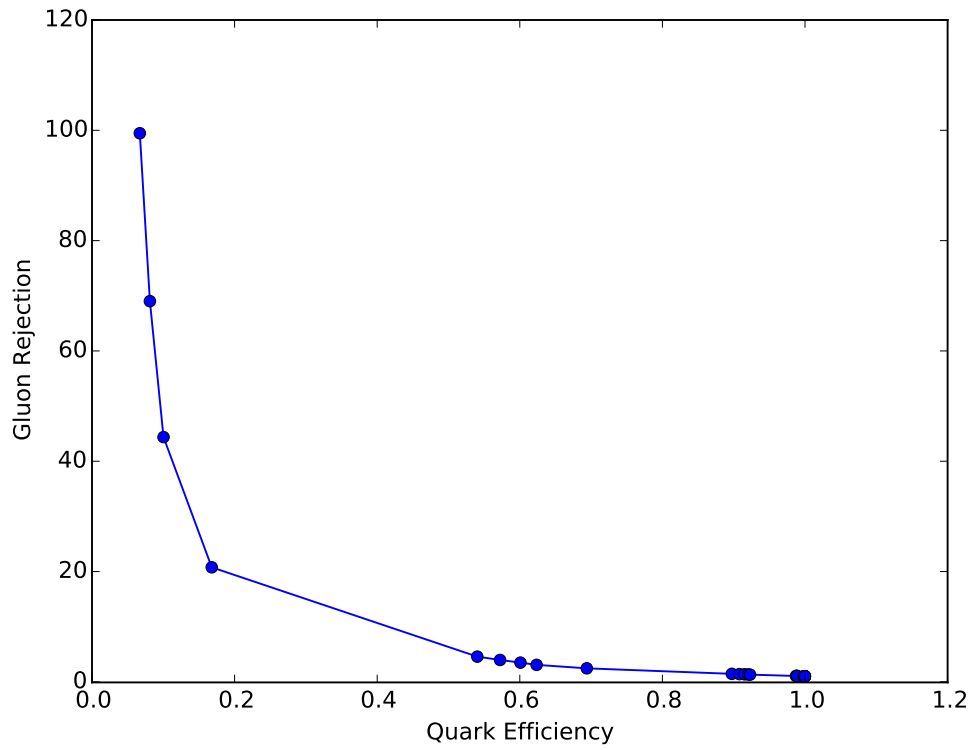


Figure 14.7: ROC Curve for Quark and Gluon Tagging with a cut on the number of tracks that depends on the $\ln(p_T)$.

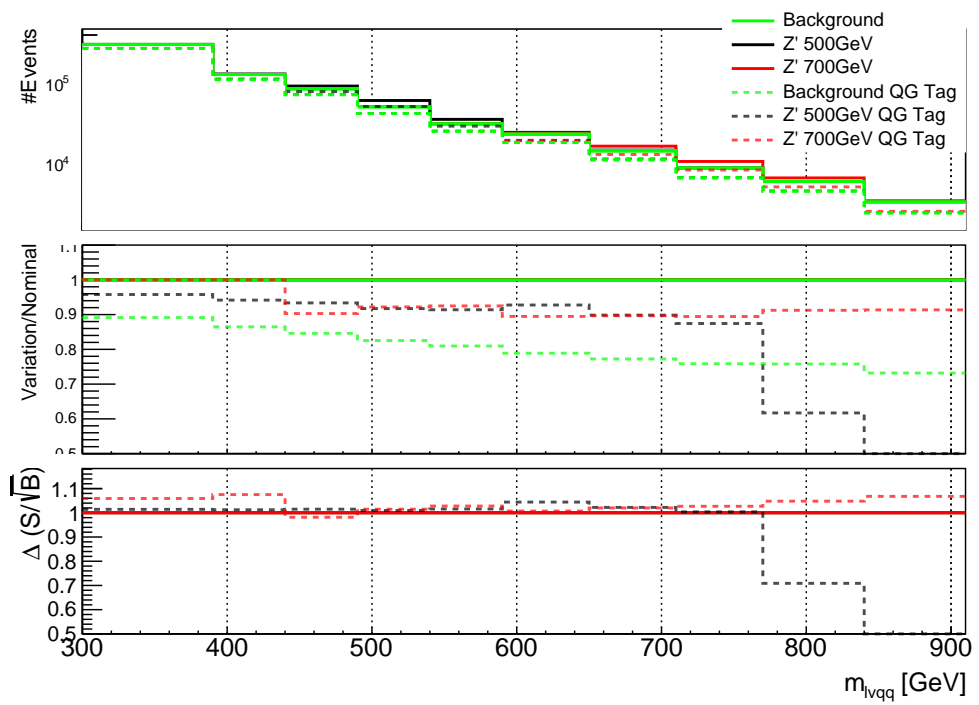


Figure 14.8: The top panel shows the distribution of m_{lvqq} with and without quark gluon tagging. The middle panel shows the ratio of the signals and backgrounds with and without quark gluon tagging. The bottom panel shows the change in S/\sqrt{B} with quark gluon tagging.

Chapter 15

Quark Gluon Tagger Calibration

The number of tracks in jets depends on modeling and experimental systematics. Consequently, the efficiency of a n_{trk} based quark-gluon tagger would have associated uncertainties. In the context of the resonance search discussed, these uncertainties would be treated as systematics that impact the m_{WV} distributions used for discovery tests.

The n_{trk} modeling uncertainties are obtained by assessing PDF and ME variations on the number of charged particles (n_c) in particle-level jets from a dijet sample. The distribution of n_c as a function of jet p_T is calculated using an Iterative Bayesian (IB) technique [26].

This measurement detailed in [22], uses the ATLAS 2012 pp collision dataset, corresponding to 20.3^{-1} fb at center-of-mass energy $\sqrt{s} = 8$ TeV. The number of charged constituents depends on fragmentation modeling and matrix elements, which do not depend on s . For this reason, it is safe to use these uncertainties for $\sqrt{s} = 13$ TeV. Monte Carlo (MC) samples are used to determine the response matrix. The MC sample is a dijet sample generated with Pythia 8.175 using CT10 PDF and AU2 tune. The anti- k_t algorithm is used to cluster jets with a radius parameter $R = 0.4$. Jets are required to have $|\eta| < 2.1$. Tracks in jets are required

to have $p_T > 500$ MeV, $|\eta| < 2.5$, track-fit $\chi^2 < 3.0$ and originate from the primary vertex. Matching tracks to jets is accomplished using ghost-association [11]. In this technique, jets are re-clustered with the track collection augmented with "ghost" versions of tracks. These "ghosts" tracks have the same direction as their parent track, but infinitesimal track p_T . This insures meta-jet properties (e.g. η , p_T , etc) are unchanged. A track is matched to a jet if it's ghost version remains in the jet after re-clustering.

To select dijet topologies events are required to have at least two jets with $p_T > 50 GeV$ that are relatively well-balanced ($p_T^{lead}/p_T^{sub-lead} < 1.5$).

In the IB technique, the prior distribution and number of iterations are the inputs [26]. The IB response matrix connects n_c to n_{trk} using the simulated samples. This response matrix is used to unfold data to extract the n_c . Before applying the response matrix a fake factor is applied. This accounts for jets that pass detector level selections, but not particle level selections. Following this, the IB method iteratively applies the response matrix using the nominal Pythia 8.175 sample as a prior. The number of IB iterations is chosen to minimize unfolding bias and statistical fluctuations. For this measurement four iterations was found to be optimal by minimizing the unfolding bias from pseudodata simulated with Herwig++ with a prior from Pythia 8 AU2. Finally, the inefficiency factor is applied to account for events passing particle level selection but not detector level, yielding the unfolded n_c distribution.

This process is prone to three main sources of bias: response matrix, correction factor, and unfolding procedure uncertainties. The response matrix is sensitive to experimental uncertainties impacting jet track reconstruction and calorimeter jet p_T . Correction factors are also sensitive to experimental uncertainties (e.g. JES) as such uncertainties modify detector level acceptance. Sensitivity to particle

level acceptance is calculated by comparing Pythia and Herwig. Finally, the bias from the IB prior choice is determined by reweighting the particle-level spectrum, so the simulated detector level spectrum more closely matches the uncorrected data. Unfolding this modified detector-level simulation and comparing it to the reweighted particle-level spectrum indicates bias from the prior distribution choice.

A summary of all the systematic uncertainties associated with this unfolding may be found in [22]. Total uncertainties are < 7% for the number of charged particles in jets. The unfolded distribution of the n_c in jets from data are further analyzed to extract the quark and gluon n_c distributions. In dijet events, the jet with a larger η is more energetic and therefore more likely to be a quark. This is due to the quarks in protons generally having a larger fraction of the total momentum of the proton constituents. The more central jet is more likely to be a gluon-initiated jet. This correlation between jet η and flavor may then be used to extract n_c in p_T bins using:

$$\langle n_c^f \rangle = f_q^f \langle n_c^q \rangle + f_g^f \langle n_c^g \rangle \quad (15.1)$$

$$\langle n_c^c \rangle = f_q^c \langle n_c^q \rangle + f_g^c \langle n_c^g \rangle \quad (15.2)$$

In this equation the f and c subscripts denote the more forward and central jets, respectively. The q and g subscripts denote quark and gluon. The fraction of more forward jets that are say, gluons, is denoted by f_g^f . The other relevant jet fractions are denoted with the same naming scheme. Finally, $\langle n_c \rangle$ is the average number of charged particles in a jet in a given p_T bin. To show these equations may be used to extract quark and gluon n_c distributions, the extracted distributions are compared to n_c distributions determined using the jet flavor in simulation. Figure 15.4 shows that the extracted and true distributions differ by < 1% over the p_T range probed for this study. Moreover, this implies that n_c

depends only on the flavor of the initiating parton and jet p_T .

These extracted distributions are prone to PDF and ME biases. The bias from the choice of the CT10 PDF for the Pythia sample is accounted for by comparing quark/gluon fractions for the nominal CT10 sample with its eigenvector variations. Comparing the quark/gluon fractions from Pythia 8 and Herwig++ quantify the uncertainty from the ME calculation. These uncertainties are added in quadrature with the unfolding uncertainty to give the total modeling uncertainty on the extracted n_c distribution. This is shown in Figure 15.1.

To apply these uncertainties in n_c distributions in data, per-jet event weights are associated with each uncertainty according to:

$$w_i(n_c) = \frac{P(n_c | < n_c > \pm \sigma_{n_c}^i)}{P(n_c | < n_c >)} \quad (15.3)$$

In Eq. 15.3, i denotes the uncertainty considered, P is the Poisson probability, and $\sigma_{n_c}^i$ represents the average impact of the uncertainty on n_c .

The previous uncertainties described accounted for modeling uncertainty associated with the number of charged particles in a jet. However, n_c is not a measurable quantity. Instead the number of tracks in a jet is measured, which is a proxy for n_c . Therefore the uncertainties associated with the measurement of n_{trk} must also be considered [24]. These uncertainties were calculated using a Pythia 8 dijet sample with NNPDF 23 and Run 2 data. Track reconstruction efficiency and fake rates are the dominant sources of n_{trk} uncertainties.

The track reconstruction efficiency is affected by the uncertainty of the description of the ID material in simulation and the modeling of charged-particle interactions with this material. These uncertainties are accounted for by varying the ID material by 5-25% (dependent on the region of the detector considered). The difference in the tracking efficiency between the nominal and varied simula-

tion give the uncertainty on the track reconstruction efficiency. Another important source of track reconstruction inefficiency arises in the core of jets. The high density of tracks in the jet cores can cause ID clusters to merge. The fraction of lost tracks due to merging is given by the fraction of tracks that have a charge of two minimum ionizing particles. This quantity is compared between data and simulation resulting in an uncertainty of 0.4% on tracks with $\Delta R < 0.1$. Combining these effects gives a total uncertainty as a function of p_T and η that is generally $< 2\%$ [24].

Fake tracks are the other dominant source of n_{trk} uncertainty. Fake tracks are tracks that cannot be associated to a single particle. Often these tracks are a result of random combinations of hits from charged particles that overlap in space. In dense environments, such as the core of jets or high-pileup environments, fake tracks are more likely. Fake tracks are estimated with a control region method which is briefly summarized here [23]. By applying a series of track selections to enrich the fraction of fake tracks (e.g. $|d_0| > 0.1$, track $\chi^2 > 1.4$, etc) in simulation, templates for fake track parameters are calculated. These templates are then fit to data to determine the fraction of fake tracks. On average the fake rate is found to be 30% (independent of p_T and η).

To assess the impact of these two detector level uncertainties, tracks are randomly dropped according to the rates described above. Reconstruction and fake uncertainties both lower the number of tracks, hence these uncertainties are one-sided. By dropping tracks in this way a varied n_{trk} distribution is calculated for both uncertainties. The associated per-jet event weights are then calculated in the same way as the modeling weights as:

$$w_i(n_c) = \frac{P(n_{trk} | n_{trk} > \pm \sigma_{n_{trk}}^i)}{P(n_{trk} | n_{trk} >)} \quad (15.4)$$

Adding the modeling and detector level uncertainties in quadrature gives the overall n_{trk} uncertainty. The effects of the individual uncertainties on the n_{trk} distributions can be seen in Fig 15.2. Fig 15.3 shows the m_{lvqq} and n_{trk} distributions for the WCR and TCR before the final likelihood fit. In these plots the n_{trk} uncertainties improve agreement between data and MC. The remaining differences are likely covered by the likelihood fit and improving the analysis itself.

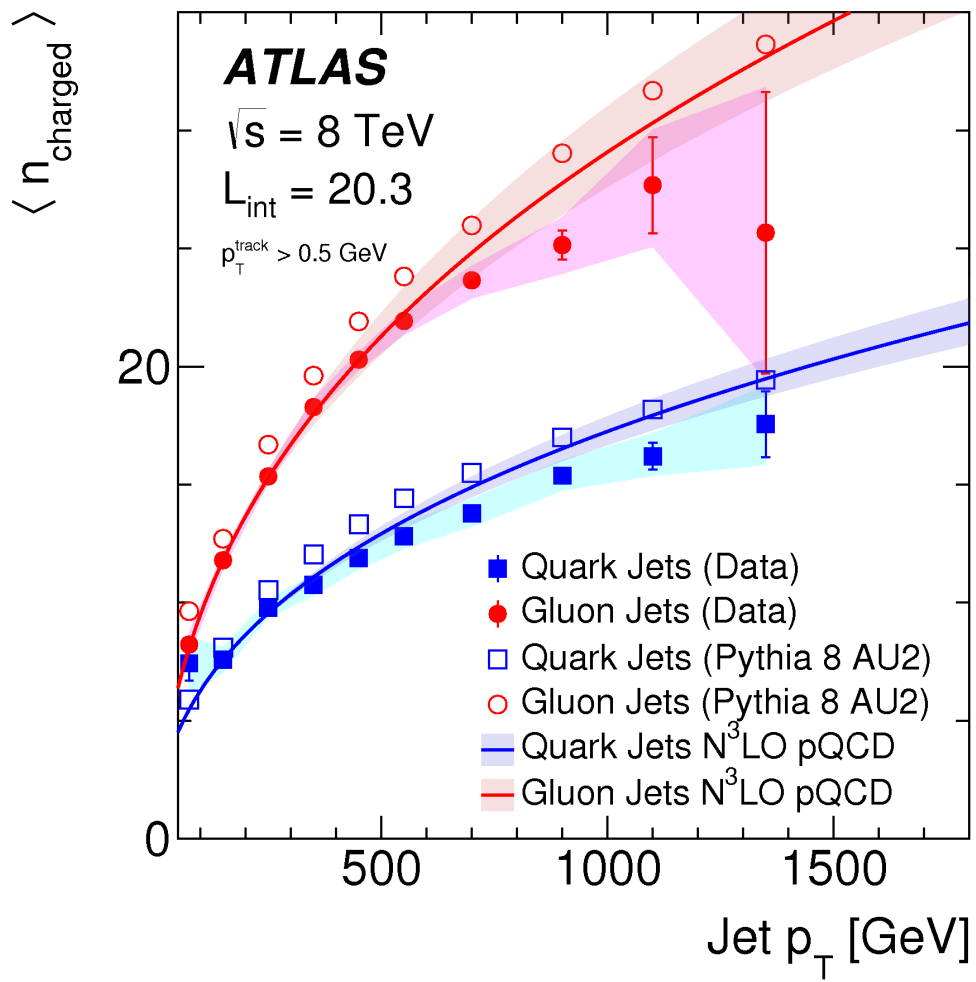


Figure 15.1: Unfolded and extracted n_c quark and gluon distributions.

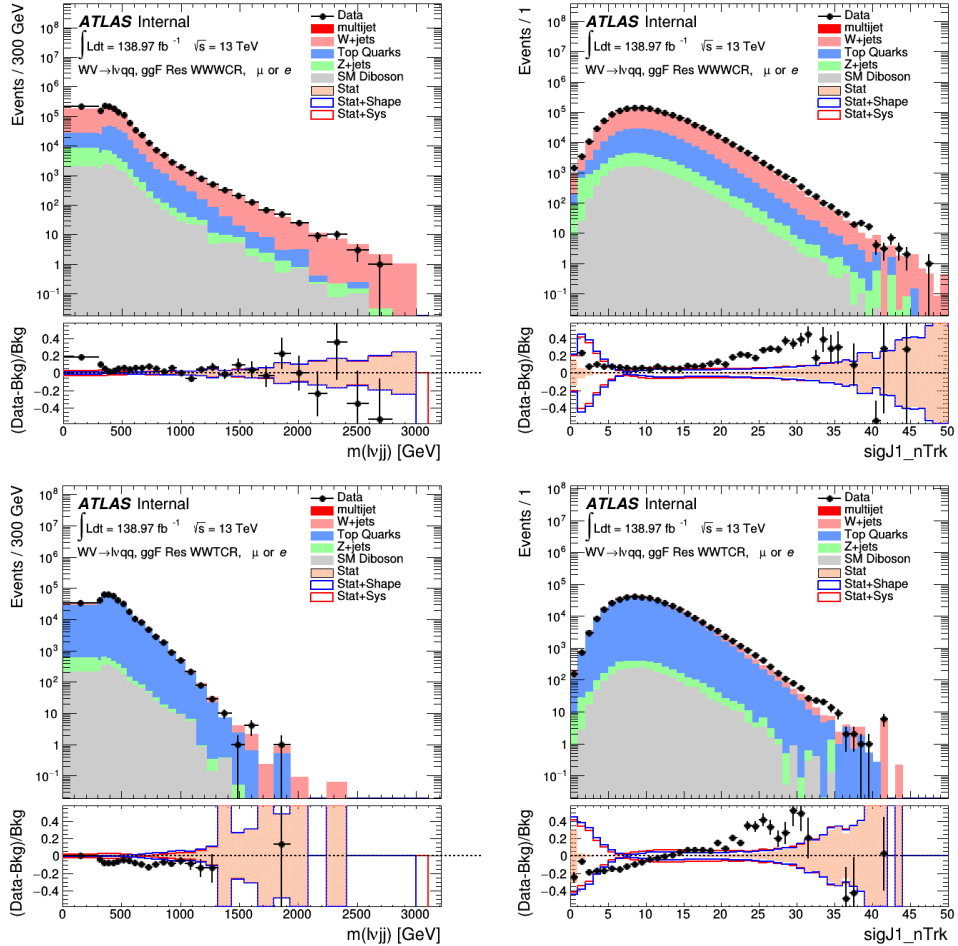


Figure 15.2: The distribution of n_{trk} and m_{WV} for the resolved WCR and TCR including systematics from the quark gluon tagger calibration.

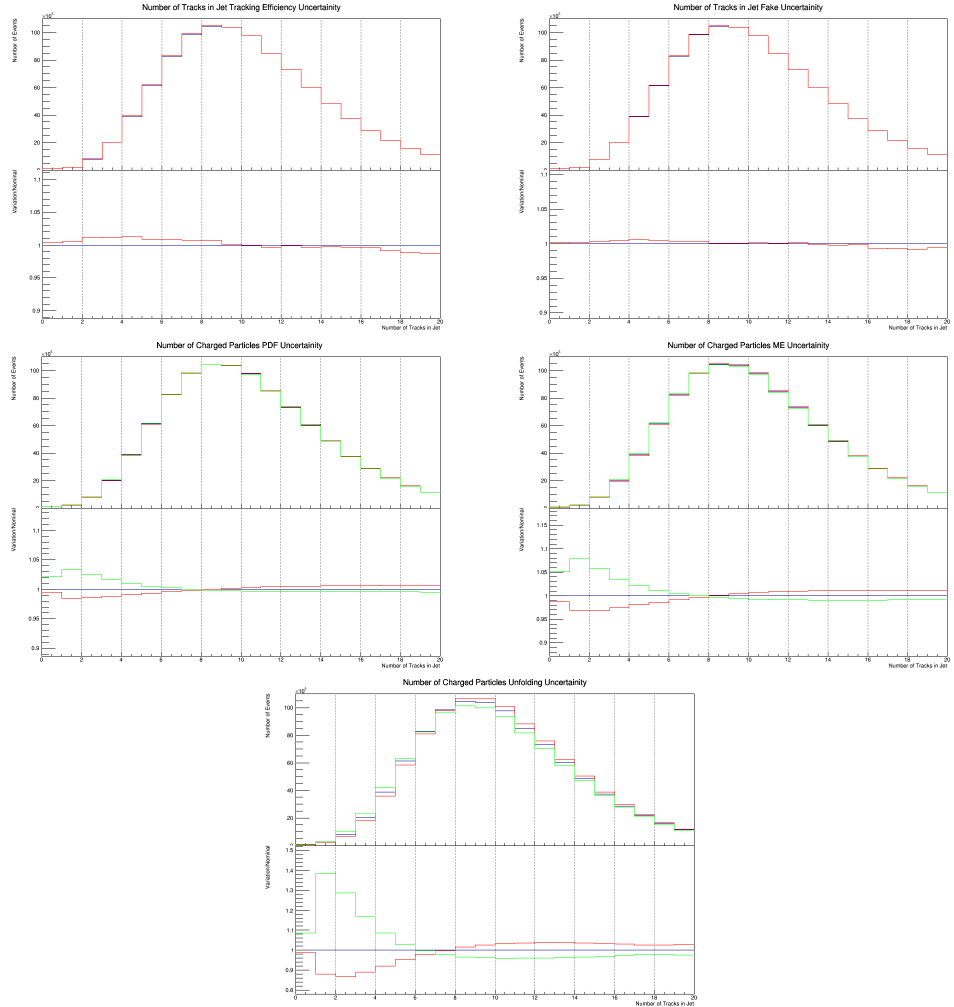


Figure 15.3: These figures show the impact of the uncertainties on the number of tracks in the leading jet in the sum of the background sample in the Resolved ggF WW SR (a) tracking efficiency (b) fake (c) PDF (d) ME (e) unfolding uncertainties.

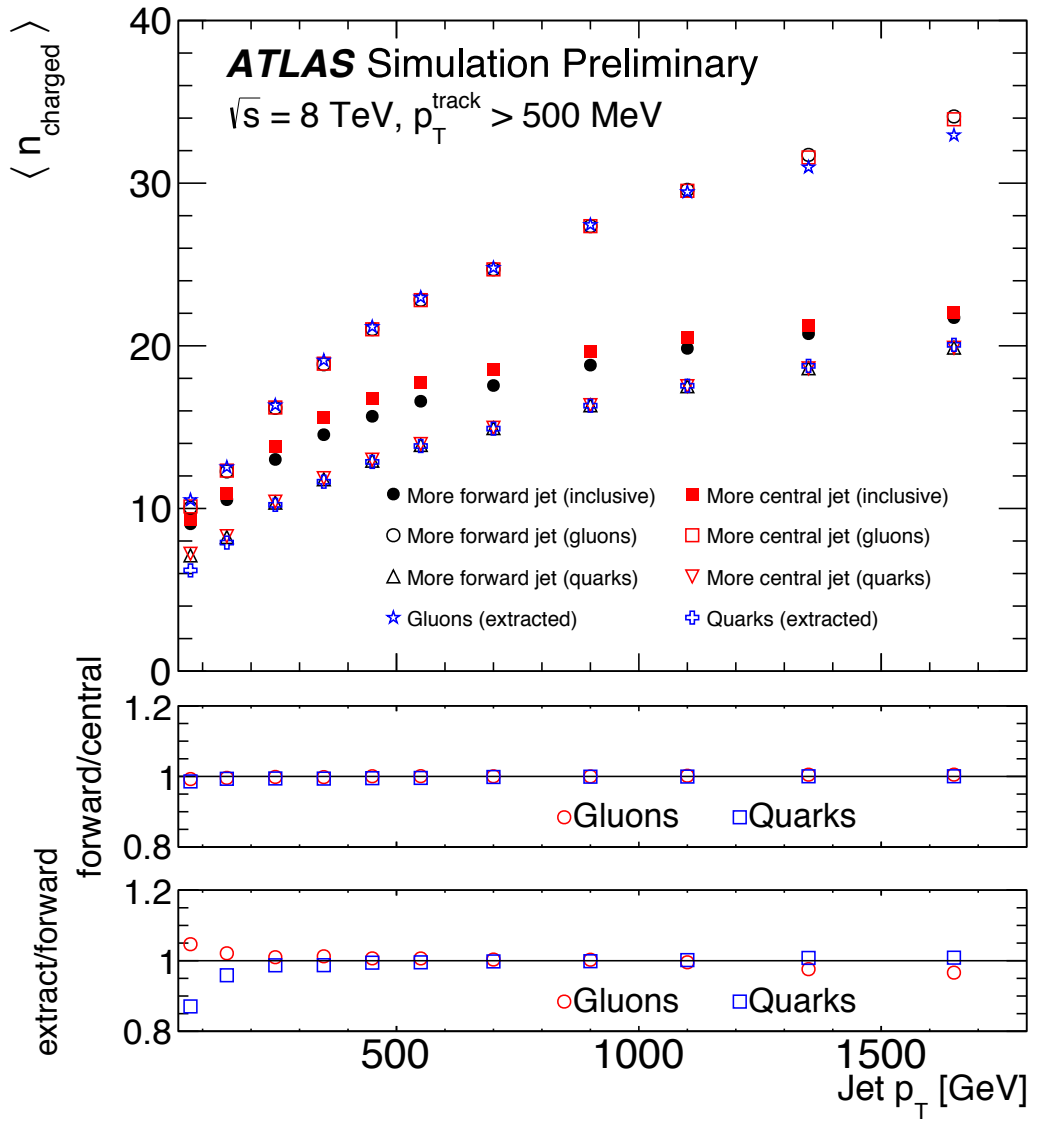


Figure 15.4: An illustration of the closure test from the central-forward method. Filled squares and circles in the upper panel are the value of $\langle n_{\text{charged}}^{c,f} \rangle$. The open blue points show $\langle n_{\text{charged}}^{q,g} \rangle$ extracted. Open red and black points show $\langle n_{\text{charged}}^{q,g} \rangle$ for the more forward and more central jets extracted from labels directly in simulation. The middle panel shows the ratio of $\langle n_{\text{charged}}^{q,g} \rangle$ for the forward versus central jets and the lower panel shows the ratio for the values extracted and the ones taken directly from simulation for the more forward jets. The extraction method used is possible because the filled red squares and circles are slightly displaced from each other. Closure is given by the fact that the open stars, circles, and up triangles overlap and the open crosses, squares, and down triangles also overlap [22].

Chapter 16

Quark Gluon Tagger Impact in Diboson Resonance Search

Using the 90% WP of the n_{trk} tagger improves S/\sqrt{B} is $\sim 3\%$ as shown in Figure 14.8. Although, n_{trk} is the single most powerful discriminating variable for quark and gluon jets, the addition of other jet variables would improve the classification efficiency. Figure 16.1 shows the possible improvement of 10% in jet classification using the truth label of the jets to classify jets. This type of improvement is possible by using variables such as jet width, and energy correlatators. Figure 16.2 shows for a 90% quark tagging efficiency for a 200 GeV jet, using a boosted decision tree improves the gluon rejection by ~ 10 . Once this tagger is calibrated it would improve the analysis sensitivity of this search.

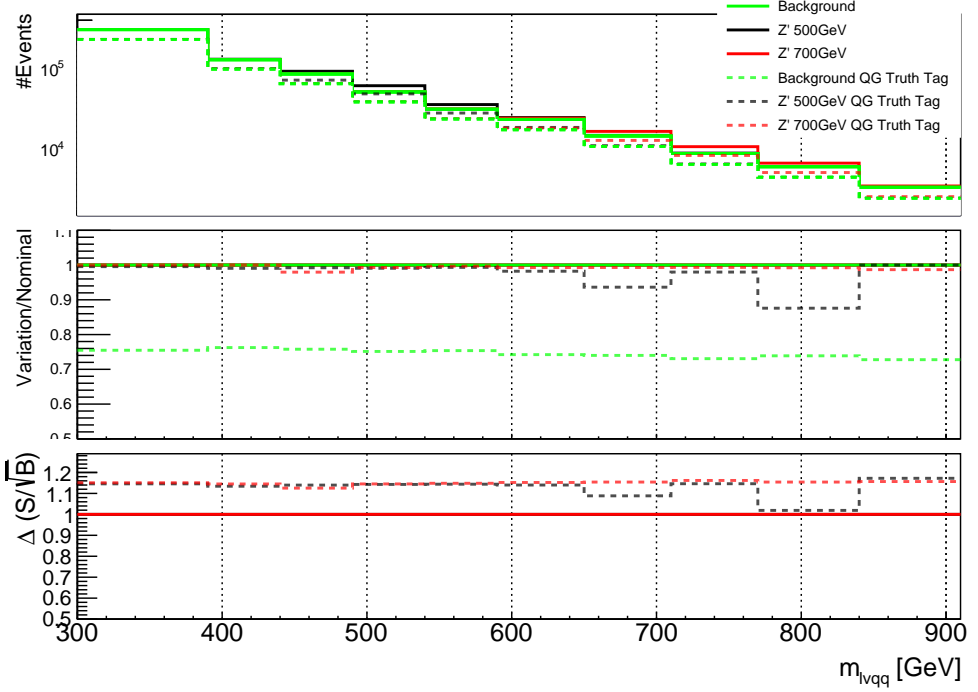


Figure 16.1: The top panel shows the distribution of m_{lvqq} with and without requiring jets to be true quarks. The middle panel shows the ratio of the signals and backgrounds with and without requiring jets to be true quarks. The bottom panel shows the change in S/\sqrt{B} when requiring jets to be true quarks.

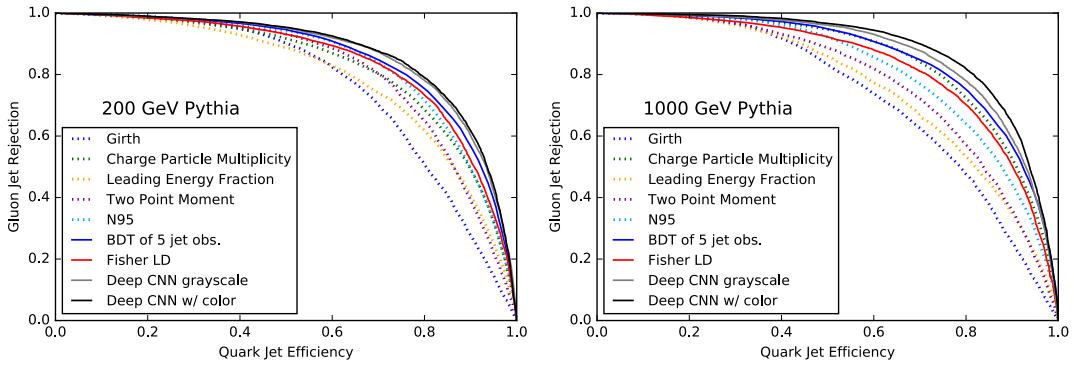


Figure 16.2: ROC curves for quark gluon tagging BDT (trained using jet substructure variables) and convolutional neural networks (trained using jet images) on (left) 200 GeV and (right) 1000 GeV Pythia jets using jet substructure variables [33].

Part VI

Conclusion

Chapter 17

Conclusions

The incompleteness of the SM motivates searching for new physics at the TeV scale. This thesis presented one such search for WW and WZ diboson resonance production in $\ell\nu qq$ final states. This search was performed using 139 fb^{-1} of pp collision data collected at a center-of-mass energy of $\sqrt{s} = 13\text{ TeV}$ by the ATLAS detector at the LHC between 2015 and 2018. No significant excess of events above the background-only expectation was observed. The largest excess is 2.7σ for a 1 TeV HVT Z' produced via VBF. Limits on the production cross sections are obtained for the HVT W' and Z' and RS Gravitons. Signal masses below 3.4 (3.7) TeV are excluded for HVT W' Model A(B). Signal masses below 3.3 (3.7) TeV are excluded for HVT Z' Model A(B). RS Gravitons are excluded for masses below 1.6 TeV. This search and other ATLAS analyses will benefit from improved jet classification. To distinguish quark and gluon jets a tagger based on the number constituent tracks in jets is studied in the $\ell\nu qq$ search and calibrated.

Bibliography

- [1] ATLAS Run 1 Pythia8 tunes. Technical Report ATL-PHYS-PUB-2014-021, CERN, Geneva, Nov 2014.
- [2] Expected performance of missing transverse momentum reconstruction for the ATLAS detector at $\sqrt{s} = 13$ TeV. Technical Report ATL-PHYS-PUB-2015-023, CERN, Geneva, Jul 2015.
- [3] Selection of jets produced in 13TeV proton-proton collisions with the ATLAS detector. Technical Report ATLAS-CONF-2015-029, CERN, Geneva, Jul 2015.
- [4] Performance of b-jet identification in the ATLAS experiment. *Journal of Instrumentation*, 11(04):P04008–P04008, Apr 2016.
- [5] Improving jet substructure performance in ATLAS using Track-Calorimeter Clusters. Technical Report ATL-PHYS-PUB-2017-015, CERN, Geneva, Jul 2017.
- [6] M. Aaboud, G. Aad, B. Abbott, J. Abdallah, O. Abdinov, B. Abelos, O. S. AbouZeid, N. L. Abraham, H. Abramowicz, and et al. Electron efficiency measurements with the ATLAS detector using 2012 LHC proton–proton collision data. *The European Physical Journal C*, 77(3), Mar 2017.
- [7] Kaustubh Agashe, Hooman Davoudiasl, Gilad Perez, and Amarjit Soni. Warped Gravitons at the LHC and Beyond. *Phys. Rev.*, D76:036006, 2007.
- [8] G. Altarelli and G. Parisi. Asymptotic freedom in parton language. *Nuclear Physics B*, 126(2):298 – 318, 1977.
- [9] J. Alwall, R. Frederix, S. Frixione, V. Hirschi, F. Maltoni, O. Mattelaer, H.-S. Shao, T. Stelzer, P. Torrielli, and M. Zaro. The automated computation of tree-level and next-to-leading order differential cross sections, and their matching to parton shower simulations. *Journal of High Energy Physics*, 2014(7), Jul 2014.
- [10] Richard D. Ball, Valerio Bertone, Stefano Carrazza, Christopher S. Deans, Luigi Del Debbio, Stefano Forte, Alberto Guffanti, Nathan P. Hartland,

José I. Latorre, and et al. Parton distributions for the lhc run ii. *Journal of High Energy Physics*, 2015(4), Apr 2015.

- [11] Matteo Cacciari, Gavin P Salam, and Gregory Soyez. The catchment area of jets. *Journal of High Energy Physics*, 2008(04):005–005, Apr 2008.
- [12] Matteo Cacciari, Gavin P. Salam, and Gregory Soyez. FastJet user manual. *The European Physical Journal C*, 72(3), Mar 2012.
- [13] M. N. Chernodub. Background magnetic field stabilizes QCD string against breaking, 2010.
- [14] ATLAS Collaboration. ATLAS Muon Reconstruction Performance in LHC Run 2.
- [15] ATLAS Collaboration. Summary plots from the ATLAS Standard Model physics group.
- [16] ATLAS Collaboration. The ATLAS Experiment at the CERN Large Hadron Collider. *Journal of Instrumentation*, 3(08):S08003–S08003, aug 2008.
- [17] ATLAS Collaboration. Tagging and suppression of pileup jets with the ATLAS detector. *ATLAS-CONF- 2014-018*, 2014.
- [18] ATLAS Collaboration. Luminosity determination in pp collisions at $\sqrt{s} = 8$ TeV using the ATLAS detector at the LHC. Luminosity determination in pp collisions at $\sqrt{s} = 8$ TeV using the ATLAS detector at the LHC. *Eur. Phys. J. C*, 76(CERN-EP-2016-117. CERN-EP-2016-117. 12):653. 71 p, Aug 2016. Comments: 53 pages plus author list + cover pages (71 pages total), 19 figures, 9 tables, submitted to EPJC, All figures including auxiliary figures are available at <http://atlas.web.cern.ch/Atlas/GROUPS/PHYSICS/PAPERS/DAPR-2013-01>.
- [19] ATLAS Collaboration. Jet energy scale measurements and their systematic uncertainties in proton-proton collisions at $\sqrt{s} = 13$ TeV with the ATLAS Detector. *Physical Review D*, 96(7), Oct 2017.
- [20] ATLAS Collaboration. Search for diboson resonances in hadronic final states in 139 fb^{-1} of pp collisions at $\sqrt{s} = 13$ TeV with the ATLAS detector. *JHEP*, 1909(arXiv:1906.08589):091. 41 p, Jun 2019. 41 pages in total, author list starting page 25, 9 figures, 3 tables, published in JHEP. All figures including auxiliary figures are available at <http://atlas.web.cern.ch/Atlas/GROUPS/PHYSICS/PAPERS/HDBS-2018-31>.

- [21] ATLAS Collaboration. Jet energy scale measurements and their systematic uncertainties in proton–proton collisions at $\sqrt{s} = 13$ TeV with the ATLAS detector. arXiv: 1703.09665 [hep-ex].
- [22] ATLAS Collaboration. Measurement of the charged-particle multiplicity inside jets from $s=\sqrt{8}$ TeV pp collisions with the ATLAS detector. arXiv:1602.00988 [hep-ex].
- [23] ATLAS Collaboration. Performance of the ATLAS track reconstruction algorithms in dense environments in LHC Run 2. arXiv:1704.07983 [hep-ex].
- [24] ATLAS Collaboration. Properties of jet fragmentation using charged particles measured with the ATLAS detector in pp collisions at $\sqrt{s} = 13$ TeV. arXiv:1906.09254 [hep-ex].
- [25] CMS Collaboration. Particle-flow reconstruction and global event description with the CMS detector, 2017.
- [26] G. D'Agostini. Improved iterative bayesian unfolding, 2010.
- [27] Alex Dias and V. Pleitez. Grand Unification and Proton Stability Near the Peccei-Quinn Scale. *Physical Review D*, 70, 07 2004.
- [28] E. Diehl. Calibration and Performance of the ATLAS Muon Spectrometer, 2011.
- [29] R. Keith Ellis, W. James Stirling, and B. R. Webber. QCD and collider physics. *Camb. Monogr. Part. Phys. Nucl. Phys. Cosmol.*, 8:1–435, 1996.
- [30] T Gleisberg, S Höche, F Krauss, M Schönherr, S Schumann, F Siegert, and J Winter. Event generation with SHERPA 1.1. *Journal of High Energy Physics*, 2009(02):007–007, Feb 2009.
- [31] Stefan Höche, Frank Krauss, Marek Schönherr, and Frank Siegert. QCD matrix elements + parton showers. The NLO case. *Journal of High Energy Physics*, 2013(4), Apr 2013.
- [32] Diederik P. Kingma and Jimmy Ba. Adam: A Method for Stochastic Optimization, 2014.
- [33] Patrick T. Komiske, Eric M. Metodiev, and Matthew D. Schwartz. Deep learning in color: towards automated quark/gluon jet discrimination. *Journal of High Energy Physics*, 2017(1), Jan 2017.
- [34] David Krohn, Jesse Thaler, and Lian-Tao Wang. Jets with variable R. *Journal of High Energy Physics*, 2009(06):059–059, Jun 2009.

- [35] David Krohn, Jesse Thaler, and Lian-Tao Wang. Jet trimming. *Journal of High Energy Physics*, 2010(2), Feb 2010.
- [36] Andrew J. Larkoski, Ian Moult, and Duff Neill. Power counting to better jet observables. *Journal of High Energy Physics*, 2014(12), Dec 2014.
- [37] Andrew J. Larkoski, Ian Moult, and Duff Neill. Analytic boosted boson discrimination. *Journal of High Energy Physics*, 2016(5), May 2016.
- [38] Gregory Soyez Matteo Cacciari, Gavin P. Salam. The anti- k_T jet clustering algorithm. arXiv:0802.1189 [hep-ph].
- [39] Benjamin Nachman. Investigating the quantum properties of jets and the search for a supersymmetric top quark partner with the atlas detector, 2016.
- [40] Duccio Pappadopulo, Andrea Thamm, Riccardo Torre, and Andrea Wulzer. Heavy vector triplets: bridging theory and data. *Journal of High Energy Physics*, 2014(9), Sep 2014.
- [41] Antonio Pich. The Standard Model of Electroweak Interactions. In *Proceedings, High-energy Physics. Proceedings, 18th European School (ESHEP 2010): Raseborg, Finland, June 20 - July 3, 2010*, pages 1–50, 2012. [,1(2012)].
- [42] Lisa Randall and Raman Sundrum. A Large mass hierarchy from a small extra dimension. *Phys. Rev. Lett.*, 83:3370–3373, 1999.
- [43] Sebastian Raschka. Model Evaluation, Model Selection, and Algorithm Selection in Machine Learning, 2018.
- [44] Alexander L. Read. Presentation of search results: The CL(s) technique. *J. Phys.*, G28:2693–2704, 2002. [,11(2002)].
- [45] Tania Robens and Tim Stefaniak. LHC benchmark scenarios for the real Higgs singlet extension of the standard model. *The European Physical Journal C*, 76(5), May 2016.
- [46] Andreas Salzburger. Optimisation of the ATLAS Track Reconstruction Software for Run-2. Technical Report ATL-SOFT-PROC-2015-056. 7, CERN, Geneva, May 2015.
- [47] Alex Sherstinsky. Fundamentals of Recurrent Neural Network (RNN) and Long Short-Term Memory (LSTM) Network. *CoRR*, abs/1808.03314, 2018.
- [48] Muhammed Ali Sit and Ibrahim Demir. Decentralized Flood Forecasting Using Deep Neural Networks. Jun 2019.
- [49] Wojciech Zaremba, Ilya Sutskever, and Oriol Vinyals. Recurrent Neural Network Regularization, 2014.